

TOOLS FOR ASSESSING  
MITOCHONDRIAL DYNAMICS IN MOUSE  
TISSUES AND NEURODEGENERATIVE  
MODELS

Thesis by

Anh H Pham

In Partial Fulfillment of the Requirements for the

Degree of

Doctor of Philosophy

CALIFORNIA INSTITUTE OF TECHNOLOGY

Pasadena, California

2013

(Defended May 31, 2012)

© 2013

Anh H Pham

All Rights Reserved

## ACKNOWLEDGEMENTS

I am grateful for the support by my advisor, Professor David Chan. The suggestions and wisdom he shared with me over the years were instrumental in my scientific training. I thank Dr. Hsiuchen Chen for training me with animal work. My projects greatly benefited from Hsiuchen's knowledgeable guidance and years of expertise with mouse experiments. I would like to acknowledge my committee members, Professor Scott Fraser, Professor Henry Lester, and Professor Paul Patterson for insightful discussions and recommendations. In particular, I greatly appreciate Professor Lester's continued interest in my project. He has provided me much encouragement and useful suggestions on multiple occasions.

I would like to thank Andrew Steele for insightful discussions about neurobiology and for use of his microscopy equipment. These resources were extremely helpful during our manuscript preparation.

I thank past and present members of the Chan lab, including Dr. Prashant Mishra, Dr. Nickie Chan, Dr. Huu Ngo, Dr. Anna Salazar, Dr. Anne Chomyn, Oliver Loson, Elisabeth Yun Wang, Priscilla Lee Wah Tee, and Rebecca Rojansky for stimulating discussions and creating a supportive working environment.

I am grateful for my parents' unconditional love and support throughout my life. They have sacrificed much for my academic accomplishments. They continue to be my inspiration and the source of my motivation. Lastly, I deeply appreciate my fiancé, Dr. John Burnett, for his enduring love and companionship. He has helped me through many

tough times and always manages to remain patient and understanding. He brings out the best in me, and I am eager to begin the next chapter of our lives in June.

## ABSTRACT

Mitochondria are dynamic organelles that undergo membrane fusion and fission and transport. The dynamic properties of mitochondria are important for regulating mitochondrial function. Defects in mitochondrial dynamics are linked to neurodegenerative diseases and affect the development of many tissues. To investigate the role of mitochondrial dynamics in diseases, versatile tools are needed to explore the physiology of these dynamic organelles in multiple tissues. Current tools for monitoring mitochondrial dynamics have been limited to studies in cell culture, which may be inadequate model systems for exploring the network of tissues. Here, we have generated mouse models for monitoring mitochondrial dynamics in a broad spectrum of tissues and cell types. The photoactivatable mitochondria (*PhAM*<sup>flaxed</sup>) line enables Cre-inducible expression of a mitochondrial targeted photoconvertible protein, Dendra2 (mito-Dendra2). In the *PhAM*<sup>excised</sup> line, mito-Dendra2 is ubiquitously expressed to facilitate broad analysis of mitochondria at various developmental processes.

We have utilized these models to study mitochondrial dynamics in the nigrostriatal circuit of Parkinson's disease (PD) and in the development of skeletal muscles. Increasing evidences implicate aberrant regulation of mitochondrial fusion and fission in models of PD. To assess the function of mitochondrial dynamics in the nigrostriatal circuit, we utilized transgenic techniques to abrogate mitochondrial fusion. We show that deletion of the *Mfn2* leads to the degeneration of dopaminergic neurons and Parkinson's-like features in mice. To elucidate the dynamic properties of mitochondria during muscle development, we established a platform for examining mitochondrial compartmentalization in skeletal

muscles. This model system may yield clues to the role of mitochondrial dynamics in mitochondrial myopathies.

## TABLE OF CONTENTS

List of Figures.....	ix
<b>Chapter 1: Introduction</b>	<b>1</b>
Mitochondria as Dynamic Organelles .....	1
Mitochondrial Dynamics in Diseases .....	8
Physiological Roles of Mitochondrial Fusion and Fission.....	11
Dysfunctional Mitochondria in Parkinson's Disease .....	16
Thesis Overview.....	20
References .....	23
<b>Chapter 2: Mouse Lines with Photoactivatable Mitochondria (PhAM) to Study Mitochondrial Dynamics</b>	<b>32</b>
Abstract.....	33
Introduction .....	34
Results and Discussion.....	36
Materials and Methods.....	42
Figure Legends.....	48
Figures .....	52
References .....	58
<b>Chapter 3: Loss of <i>Mfn2</i> Results in Progressive, Retrograde Degeneration of Dopaminergic Neurons in the Nigrostriatal Circuit</b>	<b>61</b>
Abstract.....	62
Introduction .....	63
Results .....	65
Discussion .....	71
Materials and Methods.....	73
Figure Legends.....	76
Figures .....	80
References .....	87
<b>Chapter 4: Measuring Mitochondrial Dynamics in Muscle Tissue</b>	<b>92</b>
Introduction .....	93
Results .....	96
Discussion .....	100
Materials and Methods.....	102
Figure Legends.....	104
Figures .....	106

References .....	111
<b>Chapter 5: Future Directions</b>	<b>115</b>
References .....	119
Appendix A: Preparing Parasagittal Organotypic Slices.....	121
Appendix B: Broad Activation of the Ubiquitin Proteasome System by Parkin is Critical for Mitophagy .....	126
Appendix C: Postsynaptic Decoding of Neural Activity: eEF2 as a Biochemical Sensor Coupling Miniature Synaptic Transmission to Local Protein Synthesis .....	138

## LIST OF FIGURES

	<i>Page</i>
<i>Chapter 2</i>	
Figure 2.1 Construction of <i>PhAM</i> <sup>flaxed</sup> and <i>PhAM</i> <sup>excised</sup> mouse lines .....	52
Figure 2.2 Tracking of mitochondria in <i>PhAM</i> <sup>flaxed</sup> tail fibroblasts.....	53
Figure 2.3 Expression of mito-Dendra2 in <i>PhAM</i> <sup>excised</sup> tissues .....	54
Figure 2.4 Imaging of mito-Dendra2 in live isolated cells .....	55
Figure 2.5 Purkinje-specific labeling of mitochondria.....	56
Figure 2.6 Visualizing mitochondria in Purkinje cells lacking <i>Mfn2</i> .....	57
<i>Chapter 3</i>	
Figure 3.1 Growth defect in <i>Mfn2</i> mutant mice .....	80
Figure 3.2 Longitudinal analysis of locomotion in <i>Mfn2</i> mutants.....	81
Figure 3.3 Retrograde degeneration of SNc dopaminergic neurons .....	82
Figure 3.4 Mitochondrial fragmentation and depletion in slice cultures of <i>Mfn2</i> mutants .....	83
Figure 3.5 Decreased mitochondrial transport in <i>Mfn2</i> mutant cultures .....	84
Figure 3.6 Analysis of <i>Mfn1</i> -null mice.....	85
Figure 3.7 Comparison of <i>Mfn</i> -double mutants with <i>Mfn2</i> mutants in the open field test .....	86
<i>Chapter 4</i>	
Figure 4.1 Mitochondrial fusion declines with age in EDL.....	106
Figure 4.2 Mitochondrial morphology is dependent on muscle type .....	107
Figure 4.3 Myofibers with tubular mitochondria exhibit higher membrane potential.....	108
Figure 4.4 Discrete mitochondrial domains along the myofiber .....	109

Figure 4.5 Expansive mitochondrial domain in the soleus muscle....110

## *C h a p t e r ~ I*

### INTRODUCTION

#### **Mitochondria as Dynamic Organelles**

Live imaging of mitochondria using fluorescent probes show mitochondria as dynamic and mobile organelles. Mitochondria can be visualized using genetically encoded fluorescent proteins targeted to the mitochondrial compartment or mitochondrial membrane potential sensitive dyes that accumulate in respiratory active mitochondria. Using these methods to monitor mitochondria in mammalian cells, mitochondria are observed to form reticular networks that undergo continuous structural remodeling through cycles of membrane fusion and division. Mitochondrial fusion results in merging of mitochondrial membranes and protein contents, while mitochondrial fission divides mitochondria into two shorter halves. The balance in membrane fusion and fission events dynamically regulates mitochondrial morphology. Under steady state, mitochondria appear as short tubules. However, mitochondrial profiles can range from small punctate structures to elongated tubules depending on the state of the cell. Cells undergoing apoptosis exhibit fragmented morphology while cells in the G1-S phase of the cell cycle show extended mitochondrial networks (Jagasia, Grote et al. 2005; Barsoum, Yuan et al. 2006; Mitra, Wunder et al. 2009).

A family of dynamin-related, large GTPases regulates mitochondrial morphology. Tethering of mitochondrial outer membranes is mediated by homo- and heteroprotein interactions between mitofusins, Mfn1 and Mfn2 (Chen, Detmer et al. 2003; Koshiba, Detmer et al. 2004). Based on fusion assays with isolated mitochondria, heterotypic

interactions between Mfn1 and Mfn2 mediate outer membrane fusion more efficiently compared to homotypic interactions (Hoppins, Edlich et al. 2011). However, the types of interactions found in cells are tissue specific, with heteroallelic interactions being predominant in mouse embryonic fibroblasts (MEFs) whereas giant cells in the placenta and Purkinje neurons of the cerebellum require only Mfn2 for membrane fusion (Chen, Detmer et al. 2003; Chen, McCaffery et al. 2007). More study is necessary to determine whether the strengths of mitofusin interactions, based on *in vitro* data, dictates the efficiency of mitochondrial fusion in different tissue types.

The shaping machineries for mitochondrial outer and inner membrane fusion are distinct. Mitochondrial inner membrane fusion is mediated by optic atrophy protein Opa1 (Olichon, Baricault et al. 2003; Cipolat, Martins de Brito et al. 2004; Griparic, van der Wel et al. 2004). During normal conditions, mitochondrial outer and inner membrane fusion is tightly coupled. Studies in *Saccharomyces cerevisiae* and mammalian systems show that loss of Mgm1 (yeast orthologue of Opa1) or Opa1, respectively, results in fusion intermediates that have multiple matrix compartments bounded by a single outer membrane (Hoppins, Horner et al. 2009; Song, Ghochani et al. 2009). These studies suggest that mitochondrial fusion occurs in a stepwise process with mitofusins necessary for bringing the outer membranes together and Opa1 facilitating inner membrane fusion.

The fusion of mitochondrial inner membranes is intimately linked to the bioenergetics of mitochondria (Detmer and Chan 2007). Uncoupling drugs that dissipate mitochondrial membrane potential, which is essential for the production of ATP, induce proteolytic processing of Opa1 and attenuate mitochondrial fusion (Duvezin-Caubet, Jagasia et al. 2006; Ishihara, Fujita et al. 2006; Griparic, Kanazawa et al. 2007; Song, Chen

et al. 2007). The dependence of inner membrane fusion on mitochondrial membrane potential has also been observed under endogenous conditions in the cell. By monitoring doubly labeled mitochondria with photoactivatable green fluorescent protein (GFP) and a mitochondrial dye that is potential sensitive, Twig and colleagues show that mitochondrial fusion occurs most frequently between mitochondria with intact membrane potential and sufficient Opa1 levels (Twig, Elorza et al. 2008). These findings suggest that mitochondrial fusion is a selective process that enables isolation of respiratory inactive mitochondria from the healthy pool (Twig, Elorza et al. 2008).

Taken together, the profusion machinery is an important regulator of mitochondrial morphology and can be exquisitely responsive to the bioenergetics of the cell. Mitochondrial fusion plays a protective role by enabling the exchange of proteins and metabolites for complementing mitochondrial defects. However, the fusion process is also tightly regulated to ensure quality control of the mitochondrial network.

The opposing process of mitochondrial division is mediated by dynamin-related protein Drp1(Smirnova, Griparic et al. 2001). In mammalian cells, mitochondrial fission occurs through the recruitment of cytosolic Drp1 to the mitochondria by several receptor proteins, including mitochondrial fission 1 (Fis1), mitochondrial fission factor (Mff), and more recently, mitochondrial dynamics protein 49 and Mid 51 (MiD49, MiD51). Overexpression of these receptors increases the recruitment of Drp1 to the mitochondria (James, Parone et al. 2003; Yoon, Krueger et al. 2003; Gandre-Babbe and Van Der Bliek 2008; Otera, Wang et al. 2010; Palmer, Osellame et al. 2011; Zhao, Liu et al. 2011). However, only Fis1 and Mff promote the fission activity of Drp1 whereas MiD49 and MiD51 sequester Drp1 and limit its fission activity (Dikov and Reichert 2011; Palmer,

Osellame et al. 2011; Zhao, Liu et al. 2011). Studies investigating the properties of Drp1 recruitment and regulation by these receptors are ongoing. The fission activity of Drp1 is further modulated by posttranslational modifications, including phosphorylation, sumoylation, and ubiquitination. The copious mechanisms for regulating mitochondrial morphology within a cell are impressive, and further studies will elucidate how these modes of regulation interplay in physiological and pathological states.

In addition to mitochondrial fusion and fission, mitochondria dynamically redistributes throughout the cell along cytoskeletal tracks. Disruption of the cytoskeleton by various drugs dramatically alter the distribution of mitochondria in multiple cell lines (Summerhayes, Wong et al. 1983). In neuronal studies, drugs that depolymerize actin and microtubules cause the mitochondrial network to collapse around the soma (Morris and Hollenbeck 1995; Ligon and Steward 2000). Lastly, mitochondria have also been shown to bind to neurofilaments *in vitro*, in a manner that is sensitive to mitochondrial membrane potential (Wagner, Lifshitz et al. 2003). Taken together, these studies suggest that mitochondrial transport is a regulated process that utilizes multiple cytoskeletal components in the cell.

In fluorescence time-lapse studies, mitochondria reversibly transitions between immobile and mobile states. An elegant *in vivo* study of mitochondrial transport in nerve-muscle explant and living mice observed that 87% of mitochondria are stationary in neuronal axons (Misgeld, Kerschensteiner et al. 2007). These results are consistent with studies in cultured neurons, which report 65% to 85% of the population as stationary (Overly, Rieff et al. 1996; Ligon and Steward 2000; Chang, Honick et al. 2006; Sheng and

Cai 2012). Syntaphilin has been identified as the receptor for docking mitochondria on microtubules in axons. Genetic deletion of syntaphilin in mice results in increased mitochondrial mobility and decreased mitochondrial density in axons (Kang 2008). In the mobile state, mitochondria exhibit bidirectional transport directed toward (retrograde) and away from the cell body (anterograde). The velocities of moving mitochondria vary greatly, ranging from 0.1 to 2  $\mu\text{m/s}$ , and thereby result in mean velocity between 0.3 and 0.9  $\mu\text{m/s}$  for both anterograde and retrograde directions (Ligon and Steward 2000; Misgeld, Kerschensteiner et al. 2007; Sheng and Cai 2012). Often times, mitochondrial movement appears saltatory, alternating between docked and moving states.

The rapid redistribution of mitochondria is particularly important for sustaining the dynamic activity and signaling cascades in neurons. Mitochondria support neuronal function by providing ATP and sequestering calcium to maintain calcium homeostasis. Neurons have specialized dendritic and axonal processes for transmitting and conducting electrochemical activity. Due to the unique functions and metabolic demand at these sites, mitochondrial distribution and properties are not uniform along neuronal processes. Multiple studies have shown that mitochondria are enriched at sites with high ATP demand, including active growth cones, the synaptic terminals, sites of demyelination, and nodes of Ranvier (Fabricius, Berthold et al. 1993; Morris and Hollenbeck 1993; Mutsaers and Carroll 1998; Li, Okamoto et al. 2004; Verstreken, Ly et al. 2005). By using a potentiometric mitochondrial dye to monitor mitochondria, Overly et al. showed that mitochondria in axons are more depolarized, and thus less metabolically active, compared to dendritic mitochondria (Overly, Rieff et al. 1996). There is also an inverse correlation between the size and motility of mitochondria, with smaller mitochondria exhibiting more

mobility (Misgeld, Kerschensteiner et al. 2007). Similarly, axonal mitochondria are smaller in size and move greater distances compared to dendritic mitochondria (Overly, Rieff et al. 1996; Ligon and Steward 2000; Chang, Honick et al. 2006).

In neurons, long-range transport of organelles in axons depends on microtubules whereas actin filaments mediate short-range movement in growth cones and presynaptic terminals. The kinesin superfamily and dynein are motor proteins that mediate microtubule-based transport in the anterograde and retrograde direction, respectively. Genetic screens in *Drosophila melanogaster* identified dMiro and Milton as adaptors required for mitochondrial transport. Loss of either dMiro or Milton impairs anterograde transport of mitochondria and thereby results in depletion of mitochondria at presynaptic terminals (Stowers, Megeath et al. 2002; Guo, Macleod et al. 2005). Miro is a mitochondrial outer membrane protein that has two EF-hand motifs for calcium sensing. In cells, overexpression of Milton is sufficient to recruit endogenous kinesin heavy chain and interact with exogenously expressed Miro (Glater, Megeath et al. 2006). Collectively, these results support the proposed model that the Milton-Miro complex associates with kinesin heavy chain for anterograde transport.

Mitochondrial transport in neurons is dependent on neuronal activity and intracellular calcium. Neuronal activity causes a high influx of calcium into neuronal processes. The rise in intracellular calcium is buffered by the endoplasmic reticulum and the mitochondria to prevent excitotoxicity. Multiple studies have observed changes in mitochondrial motility when neuronal activity is modulated by pharmacological agents. When synaptic activity is inhibited by tetrodotoxin, mitochondria exhibit more motility; in

contrast, stimulation of synaptic activity using glutamate or potassium chloride suppresses mitochondrial transport (Rintoul, Filiano et al. 2003; Li, Okamoto et al. 2004; Chang, Honick et al. 2006). Mitochondrial movement is also arrested in the presence of high cytosolic calcium (Wang and Schwarz 2009; Zhang, Ho et al. 2010).

Two studies have demonstrated that the EF-hand domains of Miro1 are required for the activity-dependent suppression of mitochondrial movement (MacAskill, Rinholm et al. 2009; Wang and Schwarz 2009). In cultured neurons, mutations in the Miro1 EF-hand motifs relieve the inhibition on mitochondrial transport, suggesting that calcium binding to Miro1 uncouples mitochondria from microtubules (MacAskill, Rinholm et al. 2009; Wang and Schwarz 2009). However, the mechanism for mitochondrial release is controversial as immunoprecipitation experiments from these studies lead to two distinct models. In the Wang et al. model, Miro1 was found to associate with the motor head of the kinesin heavy chain at high calcium levels to suggest that Miro1 competes with microtubules for binding with kinesin. In the motor-releasing model by MacAskill et al., Miro1 association with kinesin heavy chain decreases at elevated calcium concentration to support a model where mitochondria are released from kinesin. Collectively, these results demonstrate that the calcium-sensing domain of Miro1 enables regulated transport and release of mitochondria to active synapses with high metabolic demand and calcium signaling. The mitochondrial fusion machinery has also been implicated in regulating mitochondrial transport. Mitofusins 1 and 2 was shown to indirectly interact with the Miro-Milton complex by co-immunoprecipitation (Misko, Jiang et al. 2010).

The identification of molecular adaptors for mitochondrial transport has provided some mechanistic insight into how mitochondria are dynamically distributed in response to neuronal function. However, further studies are needed to address how mitofusins mediate mitochondrial transport. Since mitochondrial fusion and fission dynamics are important for mitochondrial function, it would be of interest to determine whether mitofusins serve a concerted role in quality control and regulated transport of mitochondria.

### **Mitochondrial Dynamics in Diseases**

Mutations of mitochondrial shaping genes identified in human diseases highlight the importance of mitochondrial dynamics for cellular processes. Currently, there are three diseases that are associated with the GTPases regulating mitochondrial morphology. Mitofusin 2 is the primary gene mutated in a common neuromuscular disease known as Charcot Marie Tooth type 2A (CMT2A) (Zuchner, Mersiyanova et al. 2004; Verhoeven, Claeys et al. 2006). CMT2A is an axonopathy that preferentially affects the long nerve processes of the motor and sensory neurons in the peripheral nervous system. Patients with CMT2A have a stepping gait, progressive muscle weakness and atrophy and loss of sensory in distal limbs. A transgenic mouse model carrying the CMT2A mutant allele of *Mfn2* provides direct evidence that implicate *Mfn2* in the disease pathology. Mice with overexpression of the T105M pathogenic allele in motor neurons exhibit a gait defect, muscle atrophy in the hindlimbs, and a decrease number of motor axons (Detmer, Velde et al. 2007). The motor and cellular phenotypes in the mouse model strikingly resemble the classical signs of CMT2A. Additionally, aggregation of mitochondria was detected in

cultured neurons with *Mfn2* disease mutations to suggest that mitochondrial transport may be altered in the disease process (Baloh, Schmidt et al. 2007; Detmer, Velde et al. 2007). Collectively, these findings suggest that *Mfn2* exert different regulatory function on mitochondrial dynamics, and its role in mitochondrial transport may explain the cell-specific susceptibility of peripheral neurons with long axons.

Mutations in *Opa1* cause an autosomal dominant form of optic atrophy (ADOA), which leads to degeneration of the optic nerve and progressive blindness (Alexander, Votruba et al. 2000; Delettre, Lenaers et al. 2000). Monocytes isolated from ADOA patients show a fragmented mitochondrial network, consistent with the role of Opa1 in mediating mitochondrial fusion (Delettre, Lenaers et al. 2000). Recently, extraocular symptoms, including myopathies, deafness, and sensory-motor neuropathy have been described in a class of ADOA plus syndromes (Amati-Bonneau, Valentino et al. 2008; Hudson, Amati-Bonneau et al. 2008). Samples collected from these patients demonstrate multiple mitochondrial DNA deletions to suggest that instability of mitochondrial DNA may contribute to the multisystemic manifestation of the disease. The phenotypic similarities shared between ADOA plus syndromes and CMT2A support the functional overlap of these mechanoenzymes in mediating mitochondrial fusion. Interestingly, deletion of mitofusins in mouse skeletal muscles leads to increased rates of mtDNA mutations and depletion (Chen, Vermulst et al. 2010). Collectively, these results underscore mitochondrial fusion as a key regulator of the integrity of mitochondrial DNA.

Mutations affecting the mitochondrial fission machinery have also been described. A single case study reported a mutation in Drp1 that resulted in neonatal lethality.

Fibroblasts from this patient demonstrated elongated mitochondrial network, consistent with a defect in mitochondrial fission (Waterham, Koster et al. 2007). The neonate also displayed symptoms of hypotonia and optic atrophy that are broadly reminiscent of CMT and ADOA diseases. The overlapping spectrum of neurological symptoms between these pathogenic alleles suggests that these neuronal subtypes may be selectively vulnerable to defects in mitochondrial dynamics. The selective vulnerability may be attributed to the intrinsic stress loads that may decrease the threshold for tolerating mitochondrial impairments and ultimately result in degeneration (Saxena and Caroni 2011).

Mitochondrial dysfunction and dynamics have also been observed in many late-onset neurodegenerative disorders including Alzheimer's (AD), Huntington's (HD), and Parkinson's disease (PD) (Chen and Chan 2009). Abnormal mitochondrial structures have been detected in ultrastructural analysis of AD brains, and the levels of mitochondrial fusion and fission genes are also dysregulated in AD samples (Baloyannis 2006; Wang, Su et al. 2009). The mutant huntingtin protein involved in HD has been shown to aggregate on mitochondria, induce mitochondrial fragmentation, and impair mitochondrial trafficking (Orr, Li et al. 2008; Wang, Lim et al. 2009) in cultured cells and mouse models. The evidence for mitochondrial dysfunction in PD is considerable. Toxins that inhibit mitochondrial respiration have provided valuable neurotoxic mouse models to understand the pathophysiology and susceptibility of dopaminergic neurons, the main target of degeneration in PD (Dauer and Przedborski 2003; Cannon and Greenamyre 2010). Furthermore, exposure to the mitochondrial toxin, 1-methyl-4-phenyl-1,2,3,6-tetrahydropyridine (MPTP), is sufficient to induce permanent Parkinsonism in humans (Langston, Ballard et al. 1983; Ballard, Tetrud et al. 1985). Evidence for the involvement

of mitochondrial dynamics in PD has come from investigations of the genes associated with familial inheritance of PD, which will be elaborated in a later section.

### **Physiological Roles of Mitochondrial Dynamics**

Several mouse models have elucidated a prominent role of mitochondrial dynamics in regulating embryonic, neuronal, skeletal muscle, cardiomyocyte development. Mitochondrial fusion and fission processes are essential for mouse embryonic development as genetic inactivation of *Mfn1*, *Mfn2*, *Opa1*, *Fis1*, and *Drp1* all cause embryonic lethality (Chen, Detmer et al. 2003; Alavi, Bette et al. 2007; Davies, Hollins et al. 2007; Ishihara, Nomura et al. 2009; Wakabayashi, Zhang et al. 2009). Loss of *Mfn2* embryonically causes placental insufficiency due to an inadequate development of trophoblast giant cells (Chen, Detmer et al. 2003). There is a dependence of *Mfn2* and *Drp1* for postnatal growth of the cerebellum since loss of either genes cause atrophy of the cerebellum and diminished dendritic arborization in Purkinje neurons (Chen, Mccaffery et al. 2007; Wakabayashi, Zhang et al. 2009; Kageyama, Zhang et al. 2012). Strikingly, mitochondria are also improperly localized in Purkinje neurons to support an intimate link between mitochondrial shape and transport (Baloh, Schmidt et al. 2007; Chen, Mccaffery et al. 2007). Interestingly, embryonic deletion of fusion and fission genes affects similar populations of cells suggesting that the balance in fusion and fission dynamics is critical for cell survival. Abrogation of both mitofusins in glycolytic muscle caused muscle atrophy and concurrent instability of mitochondrial DNA via increased rates of mutations, deletions, and depletion (Chen, Vermulst et al. 2010). A role for mitofusin in cardiac function was demonstrated

recently. Ablation of *Mfn2* and both mitofusins in adult cardiac myocytes resulted in dilated cardiomyopathy, characterized by cardiac enlargement and defective contractility (Chen, Liu et al. 2011; Papanicolaou, Khairallah et al. 2011).

Studies in cell lines have provided mechanistic understanding about the importance of mitochondrial fusion for mitochondrial metabolism, which may explain the severe *in vivo* defects in genetic mouse models. Previous reports from our lab have shown that loss of mitochondrial fusion in mouse embryonic fibroblasts causes stochastic loss of mitochondrial membrane potential, suggesting that ATP production may be compromised (Chen, Detmer et al. 2003). Indeed, when mitochondrial respiration was measured by oxygen consumption, these fibroblasts demonstrated decreased mitochondrial metabolism and cell growth (Chen, Chomyn et al. 2005). The effects of mitofusin on cell growth may be explained by the role mitochondrial fusion in the G1-S transition of the cell cycle. Lippincott-Schwartz and colleagues have demonstrated that mitochondria form a hyperfused network during the G1-S transition (Mitra, Wunder et al. 2009). This elongated and interconnected mitochondrial network exhibits hyperpolarized membrane potential, indicating a high electrical coupling and efficient ATP production. Depolarization of mitochondrial membrane potential using the FCCP uncoupler causes arrest of the cell cycle at the G1-S checkpoint and blocks the transition into the S-phase of DNA duplication. Collectively, these results suggest that the hyperfused network ensures sufficient energy production for the progression into the energetically costly S-phase (Finkel and Hwang 2009). Hyperfusion of mitochondria have also been observed transiently during a process called stress-induced hyperfusion (SIMH). When cells are exposed to stresses, including UV-irradiation, protein synthesis inhibition by cycloheximide, and repression of DNA

transcription by actinomycin D, mitochondria form a hyperfused network with an associated increase in ATP production (Tonnera, Grandemange et al. 2009). The process of SIMH is dependent on Mfn1, Opa1, and an inner membrane protein SLP2 since cells depleted of these proteins are SIMH incompetent and more sensitive to apoptosis. Collectively mitochondrial fusion seems to exert a protective role for the cell by promoting electrical coupling for efficient ATP production and conferring resistance to stress-induced cell death.

Mitochondrial fission is implicated in apoptosis. Apoptosis is a form of programmed cell death that is essential in development and can be triggered by various stimuli. There are multiple pieces of evidence that highlight the importance of mitochondria in the progression of apoptosis. First, proapoptotic molecules, such as cytochrome c, are stored in the mitochondrial intermembrane space and cristae junction, and the release of these molecules is necessary for downstream activation of the apoptotic caspase cascade. Second, mitochondria switch to a fragmented state during apoptosis and the sites of mitochondrial division coincides with the localization of early activators of apoptosis (Frank, Gaume et al. 2001; Karbowski, Lee et al. 2002). In HeLa cells, overexpression of Drp1 causes mitochondrial fragmentation and sensitizes cells to apoptotic stimulus staurosporine (Szabadkai, Simoni et al. 2004). In *Caenorhabditis elegans*, ectopic expression of Drp1 is sufficient to induce apoptosis in those cells (Jagasia, Grote et al. 2005). However, the direct role of Drp1 and mitochondrial fission in apoptosis has been questioned. By monitoring cytochrome c release using fluorescence time-lapse imaging, several studies have shown that the release of cytochrome c occurs before mitochondria fragment to argue against the model where mitochondrial fission is a

prerequisite of apoptosis (Gao, Ren et al. 2001; Arnoult, Grodet et al. 2005). Furthermore, the depletion of Drp1 in cells and mouse models only causes the delayed release of cytochrome *c* rather than prevention of apoptosis (Parone, James et al. 2006; Ishihara, Nomura et al. 2009; Wakabayashi, Zhang et al. 2009). Currently, cristae remodeling by Opa1 is proposed as another model for enabling the leakage of cytochrome *c* into the cytosol and the activation of apoptosis (Arnoult, Grodet et al. 2005; Frezza, Cipolat et al. 2006; Arnoult 2007). Taken together, these results suggest that the mechanism for Drp1 involvement and the function of mitochondrial fission in apoptosis require further investigation. Nonetheless, these findings show that perturbations to mitochondrial dynamics in favor of mitochondrial division may accelerate and sensitize cells to apoptosis.

Mitochondrial division is another quality control mechanism for mitochondria. Mitochondrial division helps to segregate defective mitochondria for selective removal by autophagy, termed mitophagy. By following mitochondrial dynamics with a potentiometric mitochondrial dye and a mitochondrial targeted photoactivatable GFP, Twig and colleagues observed that mitochondria division often generates daughter mitochondria with heterogeneous membrane potential. One daughter mitochondrion would exhibit hyperpolarized membrane potential and undergo subsequent rounds of fusion with the mitochondrial network. In contrast, the remaining depolarized mitochondrion would be fusion incompetent and be surrounded by fluorescently labeled autophagosomes (Twig, Elorza et al. 2008). Additionally, when cells are treated with the mitochondrial uncoupler CCCP to induce depolarization of the mitochondrial network, Drp1-dependent fission has been shown to be important for mediating clearance of dysfunctional mitochondria

(Tanaka, Cleland et al. 2010). These results suggest that mitochondrial fission facilitates in the separation of damaged mitochondria for mitophagy.

The targeting mechanism for mitophagy has recently been elucidated by the studies of two genes implicated in Parkinson's disease (PD), *Pink1* and *Parkin*. *Pink1* is a mitochondrial kinase that acts upstream of *Parkin*, a cytosolic E3 ubiquitin ligase. By overexpressing fluorescently tagged Parkin in cells, Narendra and colleagues show that Parkin selectively accumulates on depolarized mitochondria and recruits autophagosome formation for mitophagy (Narendra, Tanaka et al. 2008). Furthermore, Parkin localization on mitochondria occurs in a *Pink1*-dependent manner as *Pink1* deficient cells lose Parkin recruitment and Parkin-mediated mitophagy (Narendra, Jin et al. 2010). In healthy mitochondria, *Pink1* is maintained at a low level by constitutive cleavage. However, upon mitochondrial membrane depolarization, *Pink1* cleavage is inhibited, enabling *Pink1* to accumulate on the mitochondrial outer membrane and recruit Parkin (Narendra, Jin et al. 2010). Studies from our lab and others highlight that Parkin-mediated mitophagy also requires the proteasome machinery (Tanaka, Cleland et al. 2010; Chan and Chan 2011; Chan, Salazar et al. 2011; Glauser, Sonnay et al. 2011). Using quantitative mass spectrometry, we found that components of the ubiquitin proteasome (UPS) machinery were highly upregulated during Parkin recruitment. Immunoblots further confirmed that many mitochondrial outer membrane proteins, including mitofusins, were degraded via the UPS prior to mitophagy. Significantly, we showed that inhibition of the UPS is sufficient to block mitophagy, suggesting that the degradation of mitochondrial outer membrane proteins is a distinct and necessary process in mitophagy (Chan, Salazar et al. 2011). The observed degradation of mitofusins also supports the fragmented phenotype observed by

immunofluorescent studies and may reinforce the isolation of dysfunctional mitochondria after mitochondrial fission. Taken together, these results show that the UPS machinery provides an additional mechanism for targeting dysfunctional mitochondria for autophagic clearance and implicate impaired quality control of mitochondria in PD.

### **Mitochondrial Dysfunction in Parkinson's Disease (PD)**

Parkinson's disease affects over 4 million people worldwide, making PD the most common movement disorder (Dorsey, Constantinescu et al. 2007). PD is a progressive neurodegenerative disease characterized by resting tremor, postural instability, bradykinesia, and rigidity. Classically, PD is confirmed by postmortem detection of proteinaceous inclusion bodies known as Lewy bodies and the degeneration of dopaminergic neurons in the substantia nigra (SNc). However, neurodegeneration in many circuits, including cholinergic, serotonin, and norepinephrine neurons, suggests that PD is a multisystemic disorder. The idiopathic form of PD is most common and occurs in patients older than 50 years of age. The remaining 10% of PD cases have genetic origins and affect younger patients. Currently, treatments for PD only provide symptomatic relief rather than reverse the progressive neuronal loss. Cellular studies of the PD-related genes have provided valuable insight into the pathogenic mechanisms contributing to dopaminergic cell loss. Oxidative stress, toxicity of protein aggregates, calcium excitotoxicity, and mitochondrial dysfunction have all been implicated in the disease pathology. The different mechanisms causing PD have led to a proposal that dopaminergic cell loss is attributed to

multiple hits including intrinsic vulnerabilities, genetic risks, and environmental toxins (Sulzer 2007).

Mitochondrial dysfunction has been extensively documented in idiopathic and familial forms of PD. Deficiencies in the mitochondrial complex I activity have been reported in platelets, brain, fibroblasts, and muscle samples from PD patients (Parker, Boyson et al. 1989; Schapira, Cooper et al. 1989; Shoffner, Watts et al. 1991; Mann, Cooper et al. 1992; Benecke, Strumper et al. 1993; Parker and Swerdlow 1998). A recent genome-wide meta-analysis comprising over 400 samples from PD patients also confirmed the metabolic deficiencies suggested by early studies (Zheng, Liao et al. 2010). Environmental toxins and pesticides, including 1-methyl-4-phenylpyridine (MPP), that inhibit mitochondrial complex I activity can also induce chronic parkinsonism in humans (Langston, Ballard et al. 1983; Liou, Tsai et al. 1997; Gash, Rutland et al. 2008; Tanner, Ross et al. 2009). It is apparent from these studies that SN dopaminergic neurons are exquisitely sensitive to defects mitochondrial bioenergetics.

Gene expression analyses comparing the SN neurons to other dopaminergic neurons in the brain have provided some insight into the vulnerabilities of the SN. Dopaminergic neurons are found throughout the brain, with three types of dopamine neurons residing in the midbrain, the retrorubral area (A8), the substantia nigra (A9), and the ventral tegmental area (A10). These neurons are classified based on their anatomical organization and axonal projections (Björklund and Dunnett 2007). Remarkably, early histological examinations of PD brains demonstrate a pattern of loss that is regionally confined to the A9 neurons (Hirsch, Graybiel et al. 1988; Fearnley and Lees 1991). By

combining laser capture microdissection to isolate individual A9 and A10 neurons and microarray analysis of gene expression, several studies have identified distinct expression profiles between these neurons. Genes related to energy metabolism and mitochondrial proteins were consistently elevated in A9 neurons, suggesting that SN neurons have higher metabolic demand to support homeostatic function (Chung, Seo et al. 2005; Greene, Dingledine et al. 2005). Higher transcripts of adenine nucleotide translocase 2 (ANT-2) and caspase 7 were also found in A9 neurons by microarray and quantitative PCR analyses (Chung, Seo et al. 2005). The involvement of ANT-2 in regulating the mitochondrial permeability transition pore, important for cytochrome *c* release and apoptosis induction, and the higher caspase level may sensitize SN neurons to apoptosis. Moreover, the A9 cells exhibit lower levels of protective factors, including neurotrophic factors, neuropeptides, and genes involved in synaptic plasticity, compared to the VTA neurons (Grimm, Mueller et al. 2004; Chung, Seo et al. 2005; Greene, Dingledine et al. 2005). The combination of high metabolic load and low plasticity for adapting to insults may explain the susceptibility of SN neurons toward mitochondrial defects and complex I inhibitors. Collectively, the gene expression studies present mechanisms that may explain the vulnerability of the SNC toward environmental toxins and highlight the importance of mitochondrial function in these neurons.

Studies of PD-related genes and mutations underscore mitochondria as a central player in the disease and provide direct evidence for impaired mitochondrial dynamics. Multiple genes associated with PD have been shown to modulate mitochondrial morphology, including *α-synuclein*, *LRRK-2*, *DJ-1*, *Parkin*, and *Pink1*. Overexpression of *α-synuclein*, the main component in Lewy bodies, inhibits mitochondrial fusion and

induces mitochondrial fragmentation in human cells and the body wall muscles of *C. elegans* (Kamp, Exner et al. 2010). Moreover, wild-type DJ-1, Pink1, and Parkin, and not PD-related mutations, can rescue the mitochondrial fragmentation induced by  $\alpha$ -synuclein (Kamp, Exner et al. 2010). Similar studies using of *LRRK-2* and *DJ-1* also demonstrate increased mitochondrial fragmentation with PD-linked mutations (Irrcher, Aleyasin et al. 2010; Wang, Yan et al. 2012). As stated previously, Pink1 and Parkin regulate mitophagy and are therefore important in the quality control of mitochondria. Null mutations of *Pink1* and *Parkin* in *Drosophila* cause swollen mitochondria and flight defects due to dysfunction of the indirect flight muscles (Clark, Dodson et al. 2006; Yang, Gehrke et al. 2006). Interestingly, the muscle and mitochondrial abnormalities in *Pink1* and *Parkin* mutants are rescued by the overexpression of *Drp1* or the knock-down of fusion components, including *Marf* (the *Drosophila* homolog of mitofusin) and *Opa1* (Deng, Dodson et al. 2008; Poole, Thomas et al. 2008; Yang, Ouyang et al. 2008). These results clearly demonstrate that regulators of mitochondrial dynamics genetically interact with the *Pink1/Parkin* pathway and may modify the disease course. Recent studies also suggest that DJ-1 functions in a parallel pathway with Pink1/Parkin to regulate mitochondrial morphology. In *Drosophila*, expression of DJ-1 rescues the muscle and mitochondrial impairments of Pink1 mutants (Hao, Giasson et al. 2010). In *DJ-1*-null cells, overexpression of Pink1 or Parkin reverses the fragmentation of mitochondria, implying that these genes promote mitochondrial fusion (Irrcher, Aleyasin et al. 2010; Thomas, McCoy et al. 2011). Although these results demonstrate that mitochondrial dynamics may be abnormally regulated in PD, the importance of mitochondrial dynamics in dopaminergic neurons has not been directly examined.

## **Thesis Overview**

It is clear that mitochondrial function is essential for the development and survival of many tissues, and that impairments in mitochondria will impact cells with the lowest threshold to metabolic defects. Terminally differentiated cells such as neurons and muscles critically rely on mitochondrial integrity for survival. More studies are needed to identify the intrinsic processes that enhance cellular susceptibility to dysfunction in mitochondrial dynamics. To investigate the role of mitochondrial dynamics in diseases, versatile tools are needed to explore the physiology of these dynamic organelles in multiple tissues. Toward this goal, we have generated a mitochondrial reporter that facilitates broad analysis of mitochondria in different tissues and developmental stages. In the subsequent chapters, we demonstrate the versatility of these models for examining mitochondrial function in neuronal circuits and muscle compartments.

## **Chapter 2**

Mitochondrial dynamics are important in the development and survival of many tissues. Current tools for monitoring mitochondrial fusion have been limited to cell cultures. Here, we characterize the development of mouse models with photoactivatable mitochondria for visualizing mitochondria in a wide spectrum of tissue types. We constructed a mitochondrial-localized version of the photoconvertible protein, Dendra2 (mito-Dendra2), and targeted the mitochondrial reporter to the *Rosa26* locus for ubiquitous expression. The *PhAM*<sup>lox</sup> line provides Cre-inducible expression using a floxed termination signal upstream of mito-Dendra2. GermLine excision of the floxed termination cassette produced the *PhAM*<sup>excised</sup> line, which exhibits broad tissue expression

of mito-Dendra2. In these lines, Dendra2 fluorescence is restricted to the mitochondria and the photoswitchable properties of Dendra2 enable high resolution analysis of mitochondrial dynamics in dense tissues and mitochondrial network.

### **Chapter 3**

Although mitochondrial dysfunction has been extensively documented in PD, studies of PD-related genes implicate dysfunctional mitochondrial dynamics in the pathology. To determine the role of mitochondrial dynamics in dopaminergic neurons, we performed targeted deletion of *mitofusin2* (*Mfn2*) to abrogate mitochondrial fusion in the nigrostriatal circuit. We show that loss of *Mfn2* causes age-dependent deficits in locomotion that precedes the degeneration of dopaminergic neurons in the substantia nigra. Slice cultures of mutant animals also exhibit severe mitochondrial fragmentation as well as diminishment of mitochondrial mass and transport in neuronal processes. These results suggest that defects in mitochondrial dynamics may be a risk for the progression of neurodegeneration.

### **Chapter 4**

Mitochondrial fusion is important for maintaining the integrity of mitochondrial DNA in skeletal muscles. How this is achieved is unclear since the dynamics of mitochondria in skeletal muscles have not been extensively characterized. Using the *PhAM<sup>excised</sup>* model, we show that mitochondrial fusion decreases during postnatal development. We also observe a correlation between mitochondrial fusion and muscle types, with oxidative fibers exhibiting more elongated mitochondria. To explore the

compartmentalization of mitochondria along the length of a multinucleated muscle fiber, we took advantage of the leaky expression of a tamoxifen inducible Cre system to achieve sparse labeling of mitochondria along the myofiber. With this platform, we examined the dynamics of mitochondrial compartments in the myofiber during different development stages. Collectively, these results have implications for examining mitochondrial dynamics in models of mitochondrial myopathies.

## REFERENCES

- Alavi, M. V., S. Bette, et al. (2007). A splice site mutation in the murine Opa1 gene features pathology of autosomal dominant optic atrophy. *Brain*. **130**: 1029-1042.
- Alexander, C., M. Votruba, et al. (2000). OPA1, encoding a dynamin-related GTPase, is mutated in autosomal dominant optic atrophy linked to chromosome 3q28. *Nat Genet*. **26**: 211-215.
- Amati-Bonneau, P., M. L. Valentino, et al. (2008). OPA1 mutations induce mitochondrial DNA instability and optic atrophy 'plus' phenotypes. *Brain*. **131**: 338-351.
- Arnoult, D. (2007). Mitochondrial fragmentation in apoptosis. *Trends Cell Biol* **17**(1): 6-12.
- Arnoult, D., A. Grodet, et al. (2005). Release of OPA1 during apoptosis participates in the rapid and complete release of cytochrome c and subsequent mitochondrial fragmentation. *J Biol Chem* **280**(42): 35742-35750.
- Ballard, P. A., J. W. Tetrud, et al. (1985). Permanent human parkinsonism due to 1-methyl-4-phenyl-1,2,3,6-tetrahydropyridine (MPTP): seven cases. *Neurology* **35**(7): 949-956.
- Baloh, R. H., R. E. Schmidt, et al. (2007). Altered axonal mitochondrial transport in the pathogenesis of Charcot-Marie-Tooth disease from Mitofusin 2 mutations. *J Neurosci*. **27**: 422-430.
- Baloyannis, S. J. (2006). Mitochondrial alterations in Alzheimer's disease. *J Alzheimers Dis* **9**(2): 119-126.
- Barsoum, M. J., H. Yuan, et al. (2006). Nitric oxide-induced mitochondrial fission is regulated by dynamin-related GTPases in neurons. *EMBO J* **25**(16): 3900-3911.
- Benecke, R., P. Strumper, et al. (1993). Electron transfer complexes I and IV of platelets are abnormal in Parkinson's disease but normal in Parkinson-plus syndromes. *Brain* **116** ( Pt 6): 1451-1463.
- Björklund, A. and S. B. Dunnett (2007). Dopamine neuron systems in the brain: An update. *Trends Neurosci*. **30**: 194-202.
- Cannon, J. R. and J. T. Greenamyre (2010). Neurotoxic in vivo models of Parkinson's disease recent advances. *Prog Brain Res* **184**: 17-33.
- Chan, N. C. and D. C. Chan (2011). Parkin uses the UPS to ship off dysfunctional mitochondria. *Autophagy* **7**(7): 771-772.
- Chan, N. C., A. M. Salazar, et al. (2011). Broad activation of the ubiquitin-proteasome system by Parkin is critical for mitophagy. *Hum Mol Genet* **20**(9): 1726-1737.

- Chang, D. T. W., A. S. Honick, et al. (2006). Mitochondrial trafficking to synapses in cultured primary cortical neurons. *J Neurosci.* **26:** 7035-7045.
- Chen, H. and D. C. Chan (2009). Mitochondrial dynamics-fusion, fission, movement, and mitophagy in neurodegenerative diseases. *Human Molecular Genetics.* **18:** R169-176.
- Chen, H., A. Chomyn, et al. (2005). Disruption of fusion results in mitochondrial heterogeneity and dysfunction. *J Biol Chem.* **280:** 26185-26192.
- Chen, H., S. A. Detmer, et al. (2003). Mitofusins Mfn1 and Mfn2 coordinately regulate mitochondrial fusion and are essential for embryonic development. *J Cell Biol* **160**(2): 189-200.
- Chen, H., J. McCaffery, et al. (2007). Mitochondrial Fusion Protects against Neurodegeneration in the Cerebellum. *Cell.* **130:** 548-562.
- Chen, H., M. Vermulst, et al. (2010). Mitochondrial fusion is required for mtDNA stability in skeletal muscle and tolerance of mtDNA mutations. *Cell.* **141:** 280-289.
- Chen, Y., Y. Liu, et al. (2011). Mitochondrial fusion is essential for organelle function and cardiac homeostasis. *Circ Res* **109**(12): 1327-1331.
- Chung, C. Y., H. Seo, et al. (2005). Cell type-specific gene expression of midbrain dopaminergic neurons reveals molecules involved in their vulnerability and protection. *Hum Mol Genet* **14**(13): 1709-1725.
- Cipolat, S., O. Martins de Brito, et al. (2004). OPA1 requires mitofusin 1 to promote mitochondrial fusion. *Proc Natl Acad Sci USA.* **101:** 15927-15932.
- Clark, I. E., M. W. Dodson, et al. (2006). Drosophila pink1 is required for mitochondrial function and interacts genetically with parkin. *Nature.* **441:** 1162-1166.
- Dauer, W. and S. Przedborski (2003). Parkinson's Disease Mechanisms and Models. *Neuron.* **39:** 889-909.
- Davies, V. J., A. J. Hollins, et al. (2007). Opa1 deficiency in a mouse model of autosomal dominant optic atrophy impairs mitochondrial morphology, optic nerve structure and visual function. *Hum Mol Genet.* **16:** 1307-1318.
- Delettre, C., G. Lenaers, et al. (2000). Nuclear gene OPA1, encoding a mitochondrial dynamin-related protein, is mutated in dominant optic atrophy. *Nat Genet.* **26:** 207-210.
- Deng, H., M. W. Dodson, et al. (2008). The Parkinson's disease genes pink1 and parkin promote mitochondrial fission and/or inhibit fusion in *Drosophila*. *Proc Natl Acad Sci USA.* **105:** 14503-14508.

- Detmer, S. A. and D. C. Chan (2007). Functions and dysfunctions of mitochondrial dynamics. Nat Rev Mol Cell Biol. **8**: 870-879.
- Detmer, S. A., C. V. Velde, et al. (2007). Hindlimb gait defects due to motor axon loss and reduced distal muscles in a transgenic mouse model of Charcot-Marie-Tooth type 2A. Hum Mol Genet. **17**: 367-375.
- Dikov, D. and A. S. Reichert (2011). How to split up: lessons from mitochondria. EMBO J. **30**: 2751.
- Dorsey, E. R., R. Constantinescu, et al. (2007). Projected number of people with Parkinson disease in the most populous nations, 2005 through 2030. Neurology **68**(5): 384-386.
- Duvezin-Caubet, S., R. Jagasia, et al. (2006). Proteolytic processing of OPA1 links mitochondrial dysfunction to alterations in mitochondrial morphology. J Biol Chem. **281**: 37972-37979.
- Fabricius, C., C. H. Berthold, et al. (1993). Axoplasmic organelles at nodes of Ranvier. II. Occurrence and distribution in large myelinated spinal cord axons of the adult cat. J Neurocytol **22**(11): 941-954.
- Fearnley, J. M. and A. J. Lees (1991). Ageing and Parkinson's disease: substantia nigra regional selectivity. Brain **114** (Pt 5): 2283-2301.
- Finkel, T. and P. M. Hwang (2009). The Krebs cycle meets the cell cycle: mitochondria and the G1-S transition. Proc Natl Acad Sci USA **106**(29): 11825-11826.
- Frank, S., B. Gaume, et al. (2001). The role of dynamin-related protein 1, a mediator of mitochondrial fission, in apoptosis. Dev Cell **1**(4): 515-525.
- Frezza, C., S. Cipolat, et al. (2006). OPA1 controls apoptotic cristae remodeling independently from mitochondrial fusion. Cell. **126**: 177-189.
- Gandre-Babbe, S. and A. Van Der Bliek (2008). The Novel Tail-anchored Membrane Protein Mff Controls Mitochondrial and Peroxisomal Fission in Mammalian Cells. Mol Bio Cell. **19**: 2402.
- Gao, C. F., S. Ren, et al. (2001). Caspase-dependent cytosolic release of cytochrome c and membrane translocation of Bax in p53-induced apoptosis. Exp Cell Res **265**(1): 145-151.
- Gash, D. M., K. Rutland, et al. (2008). Trichloroethylene: Parkinsonism and complex 1 mitochondrial neurotoxicity. Ann Neurol **63**(2): 184-192.
- Glater, E. E., L. J. Megeath, et al. (2006). Axonal transport of mitochondria requires milton to recruit kinesin heavy chain and is light chain independent. J Cell Bio. **173**: 545-557.

- Glauser, L., S. Sonnay, et al. (2011). Parkin promotes the ubiquitination and degradation of the mitochondrial fusion factor mitofusin 1. *J Neurochem* **118**(4): 636-645.
- Greene, J. G., R. Dingledine, et al. (2005). Gene expression profiling of rat midbrain dopamine neurons: implications for selective vulnerability in parkinsonism. *Neurobiol Dis* **18**(1): 19-31.
- Grimm, J., A. Mueller, et al. (2004). Molecular basis for catecholaminergic neuron diversity. *Proc Natl Acad Sci USA* **101**(38): 13891-13896.
- Gripasic, L., T. Kanazawa, et al. (2007). Regulation of the mitochondrial dynamin-like protein Opa1 by proteolytic cleavage. *J Cell Bio*. **178**: 757-764.
- Gripasic, L., N. N. van der Wel, et al. (2004). Loss of the intermembrane space protein Mgm1/OPA1 induces swelling and localized constrictions along the lengths of mitochondria. *J Biol Chem*. **279**: 18792-18798.
- Guo, X., G. T. Macleod, et al. (2005). The GTPase dMiro is required for axonal transport of mitochondria to Drosophila synapses. *Neuron*. **47**: 379-393.
- Hao, L. Y., B. I. Giasson, et al. (2010). DJ-1 is critical for mitochondrial function and rescues PINK1 loss of function. *Proc Natl Acad Sci USA* **107**(21): 9747-9752.
- Hirsch, E., A. M. Graybiel, et al. (1988). Melanized dopaminergic neurons are differentially susceptible to degeneration in Parkinson's disease. *Nature*. **334**: 345-348.
- Hoppins, S., F. Edlich, et al. (2011). The soluble form of Bax regulates mitochondrial fusion via MFN2 homotypic complexes. *Mol Cell* **41**(2): 150-160.
- Hoppins, S., J. Horner, et al. (2009). Mitochondrial outer and inner membrane fusion requires a modified carrier protein. *J Cell Biol* **184**(4): 569-581.
- Hudson, G., P. Amati-Bonneau, et al. (2008). Mutation of OPA1 causes dominant optic atrophy with external ophthalmoplegia, ataxia, deafness and multiple mitochondrial DNA deletions: a novel disorder of mtDNA maintenance. *Brain*. **131**: 329-337.
- Irreher, I., H. Aleyasin, et al. (2010). Loss of the Parkinson's disease-linked gene DJ-1 perturbs mitochondrial dynamics. *Hum Mol Genet* **19**(19): 3734-3746.
- Ishihara, N., Y. Fujita, et al. (2006). Regulation of mitochondrial morphology through proteolytic cleavage of OPA1. *EMBO J*. **25**: 2966-2977.
- Ishihara, N., M. Nomura, et al. (2009). Mitochondrial fission factor Drp1 is essential for embryonic development and synapse formation in mice. *Nat Cell Biol* **11**(8): 958-966.

- Jagasia, R., P. Grote, et al. (2005). DRP-1-mediated mitochondrial fragmentation during EGL-1-induced cell death in *C. elegans*. *Nature* **433**(7027): 754-760.
- James, D. I., P. A. Parone, et al. (2003). hFis1, a novel component of the mammalian mitochondrial fission machinery. *J Biol Chem* **278**(38): 36373-36379.
- Kageyama, Y., Z. Zhang, et al. (2012). Mitochondrial division ensures the survival of postmitotic neurons by suppressing oxidative damage. *J Cell Biol*.
- Kamp, F., N. Exner, et al. (2010). Inhibition of mitochondrial fusion by alpha-synuclein is rescued by PINK1, Parkin and DJ-1. *EMBO J* **29**(20): 3571-3589.
- Kang, J. (2008). Docking of Axonal Mitochondria by Syntaphilin Controls Their Mobility and Affects Short-Term Facilitation. *Cell* **132**: 137-148.
- Karbowski, M., Y. J. Lee, et al. (2002). Spatial and temporal association of Bax with mitochondrial fission sites, Drp1, and Mfn2 during apoptosis. *J Cell Biol* **159**(6): 931-938.
- Koshiba, T., S. A. Detmer, et al. (2004). Structural basis of mitochondrial tethering by mitofusin complexes. *Science* **305**: 858-862.
- Langston, J. W., P. Ballard, et al. (1983). Chronic Parkinsonism in humans due to a product of meperidine-analog synthesis. *Science* **219**(4587): 979-980.
- Li, Z., K. Okamoto, et al. (2004). The Importance of Dendritic Mitochondria in the Morphogenesis and Plasticity of Spines and Synapses. *Cell* **119**: 873-887.
- Ligon, L. A. and O. Steward (2000a). Movement of mitochondria in the axons and dendrites of cultured hippocampal neurons. *J Comp Neurol* **427**: 340-350.
- Ligon, L. A. and O. Steward (2000b). Role of microtubules and actin filaments in the movement of mitochondria in the axons and dendrites of cultured hippocampal neurons. *J Comp Neurol* **427**(3): 351-361.
- Liou, H. H., M. C. Tsai, et al. (1997). Environmental risk factors and Parkinson's disease: a case-control study in Taiwan. *Neurology* **48**(6): 1583-1588.
- MacAskill, A. F., J. E. Rinholm, et al. (2009). Miro1 is a calcium sensor for glutamate receptor-dependent localization of mitochondria at synapses. *Neuron* **61**: 541-555.
- Mann, V. M., J. M. Cooper, et al. (1992). Brain, skeletal muscle and platelet homogenate mitochondrial function in Parkinson's disease. *Brain* **115** ( Pt 2): 333-342.
- Misgeld, T., M. Kerschensteiner, et al. (2007). Imaging axonal transport of mitochondria in vivo. *Nat Meth* **4**: 559-561.

Misko, A., S. Jiang, et al. (2010). Mitofusin 2 is necessary for transport of axonal mitochondria and interacts with the Miro/Milton complex. *J Neurosci*. **30**: 4232-4240.

Mitra, K., C. Wunder, et al. (2009). A hyperfused mitochondrial state achieved at G1-S regulates cyclin E buildup and entry into S phase. *Proceedings of the National Academy of Sciences of the United States of America*. **106**: 11960-11965.

Morris, R. L. and P. J. Hollenbeck (1993). The regulation of bidirectional mitochondrial transport is coordinated with axonal outgrowth. *J Cell Sci* **104** (Pt 3): 917-927.

Morris, R. L. and P. J. Hollenbeck (1995). Axonal transport of mitochondria along microtubules and F-actin in living vertebrate neurons. *J Cell Biol* **131**(5): 1315-1326.

Mutsaers, S. E. and W. M. Carroll (1998). Focal accumulation of intra-axonal mitochondria in demyelination of the cat optic nerve. *Acta Neuropathol* **96**(2): 139-143.

Narendra, D. P., A. Tanaka, et al. (2008). Parkin is recruited selectively to impaired mitochondria and promotes their autophagy. *J Cell Biol*: jcb.200809125.

Narendra, D. P., S. M. Jin, et al. (2010). PINK1 Is Selectively Stabilized on Impaired Mitochondria to Activate Parkin. *PLoS Biol*. **8**.

Olichon, A., L. Baricault, et al. (2003). Loss of OPA1 perturbs the mitochondrial inner membrane structure and integrity, leading to cytochrome c release and apoptosis. *J Biol Chem*. **278**: 7743-7746.

Orr, A. L., S. Li, et al. (2008). N-terminal mutant huntingtin associates with mitochondria and impairs mitochondrial trafficking. *J Neurosci* **28**(11): 2783-2792.

Otera, H., C. Wang, et al. (2010). Mff is an essential factor for mitochondrial recruitment of Drp1 during mitochondrial fission in mammalian cells. *J Cell Biol*. **191**: 1141-1158.

Overly, C. C., H. I. Rieff, et al. (1996). Organelle motility and metabolism in axons vs dendrites of cultured hippocampal neurons. *J Cell Sci* **109** (Pt 5): 971-980.

Palmer, C. S., L. D. Osellame, et al. (2011). MiD49 and MiD51, new components of the mitochondrial fission machinery. *EMBO reports*.

Papanicolaou, K. N., R. J. Khairallah, et al. (2011). Mitofusin-2 maintains mitochondrial structure and contributes to stress-induced permeability transition in cardiac myocytes. *Mol Cell Biol* **31**(6): 1309-1328.

Parker, W. D., Jr., S. J. Boyson, et al. (1989). Abnormalities of the electron transport chain in idiopathic Parkinson's disease. *Ann Neurol* **26**(6): 719-723.

Parker, W. D., Jr. and R. H. Swerdlow (1998). Mitochondrial dysfunction in idiopathic Parkinson disease. *Am J Hum Genet* **62**(4): 758-762.

- Parone, P. A., D. I. James, et al. (2006). Inhibiting the mitochondrial fission machinery does not prevent Bax/Bak-dependent apoptosis. *Mol Cell Biol* **26**(20): 7397-7408.
- Poole, A. C., R. E. Thomas, et al. (2008). The PINK1/Parkin pathway regulates mitochondrial morphology. *Proc Natl Acad Sci USA* **105**: 1638-1643.
- Rintoul, G. L., A. J. Filiano, et al. (2003). Glutamate decreases mitochondrial size and movement in primary forebrain neurons. *J Neurosci* **23**(21): 7881-7888.
- Saxena, S. and P. Caroni (2011). Selective neuronal vulnerability in neurodegenerative diseases: from stressor thresholds to degeneration. *Neuron* **71**: 35-48.
- Schapira, A. H., J. M. Cooper, et al. (1989). Mitochondrial complex I deficiency in Parkinson's disease. *Lancet* **1**(8649): 1269.
- Sheng, Z. H. and Q. Cai (2012). Mitochondrial transport in neurons: impact on synaptic homeostasis and neurodegeneration. *Nat Rev Neurosci* **13**(2): 77-93.
- Shoffner, J. M., R. L. Watts, et al. (1991). Mitochondrial oxidative phosphorylation defects in Parkinson's disease. *Ann Neurol* **30**(3): 332-339.
- Smirnova, E., L. Gripasic, et al. (2001). Dynamin-related protein Drp1 is required for mitochondrial division in mammalian cells. *Mol Biol Cell* **12**(8): 2245-2256.
- Song, Z., H. Chen, et al. (2007). OPA1 processing controls mitochondrial fusion and is regulated by mRNA splicing, membrane potential, and Yme1L. *J Cell Biol* **178**: 749-755.
- Song, Z., M. Ghochani, et al. (2009). Mitofusins and OPA1 mediate sequential steps in mitochondrial membrane fusion. *Mol Biol Cell* **20**: 3525-3532.
- Stowers, R. S., L. J. Megeath, et al. (2002). Axonal transport of mitochondria to synapses depends on milton, a novel *Drosophila* protein. *Neuron* **36**: 1063-1077.
- Sulzer, D. (2007). Multiple hit hypotheses for dopamine neuron loss in Parkinson's disease. *Trends Neurosci* **30**: 244-250.
- Summerhayes, I. C., D. Wong, et al. (1983). Effect of microtubules and intermediate filaments on mitochondrial distribution. *J Cell Sci* **61**: 87-105.
- Szabadkai, G., A. M. Simoni, et al. (2004). Drp-1-dependent division of the mitochondrial network blocks intraorganellar Ca<sup>2+</sup> waves and protects against Ca<sup>2+</sup>-mediated apoptosis. *Mol Cell* **16**(1): 59-68.
- Tanaka, A., M. M. Cleland, et al. (2010). Proteasome and p97 mediate mitophagy and degradation of mitofusins induced by Parkin. *J Cell Biol* **191**(7): 1367-1380.

- Tanner, C. M., G. W. Ross, et al. (2009). Occupation and risk of parkinsonism: a multicenter case-control study. *Arch Neurol* **66**(9): 1106-1113.
- Thomas, K. J., M. K. McCoy, et al. (2011). DJ-1 acts in parallel to the PINK1/parkin pathway to control mitochondrial function and autophagy. *Hum Mol Genet* **20**(1): 40-50.
- Tondera, D., S. Grandemange, et al. (2009). SLP-2 is required for stress-induced mitochondrial hyperfusion. *EMBO J.*
- Twig, G., A. Elorza, et al. (2008). Fission and selective fusion govern mitochondrial segregation and elimination by autophagy. *EMBO J.* **27**: 433-446.
- Verhoeven, K., K. Claeys, et al. (2006). MFN2 mutation distribution and genotype/phenotype correlation in Charcot-Marie-Tooth type 2. *Brain*. **129**: 2093.
- Verstreken, P., C. V. Ly, et al. (2005). Synaptic mitochondria are critical for mobilization of reserve pool vesicles at Drosophila neuromuscular junctions. *Neuron*. **47**: 365-378.
- Wagner, O. I., J. Lifshitz, et al. (2003). Mechanisms of mitochondria-neurofilament interactions. *J Neurosci* **23**(27): 9046-9058.
- Wakabayashi, J., Z. Zhang, et al. (2009). The dynamin-related GTPase Drp1 is required for embryonic and brain development in mice. *J Cell Biol*: jcb.200903065v200903061.
- Wang, H., P. J. Lim, et al. (2009). Effects of overexpression of huntingtin proteins on mitochondrial integrity. *Hum Mol Genet*. **18**: 737-752.
- Wang, X. and T. L. Schwarz (2009). The mechanism of Ca<sup>2+</sup>-dependent regulation of kinesin-mediated mitochondrial motility. *Cell*. **136**: 163-174.
- Wang, X., B. Su, et al. (2009). Impaired balance of mitochondrial fission and fusion in Alzheimer's disease. *J Neurosci*. **29**: 9090-9103.
- Wang, X., M. H. Yan, et al. (2012). LRRK2 regulates mitochondrial dynamics and function through direct interaction with DLP1. *Hum Mol Genet* **21**(9): 1931-1944.
- Waterham, H. R., J. Koster, et al. (2007). A lethal defect of mitochondrial and peroxisomal fission. *N Engl J Med*. **356**: 1736-1741.
- Yang, Y., S. Gehrke, et al. (2006). Mitochondrial pathology and muscle and dopaminergic neuron degeneration caused by inactivation of Drosophila Pink1 is rescued by Parkin. *Proc Natl Acad Sci USA*. **103**: 10793-10798.
- Yang, Y., Y. Ouyang, et al. (2008). Pink1 regulates mitochondrial dynamics through interaction with the fission/fusion machinery. *Proc Natl Acad Sci USA*. **105**: 7070-7075.

Yoon, Y., E. W. Krueger, et al. (2003). The mitochondrial protein hFis1 regulates mitochondrial fission in mammalian cells through an interaction with the dynamin-like protein DLP1. Mol Cell Biol **23**(15): 5409-5420.

Zhang, C. L., P. L. Ho, et al. (2010). Activity-dependent regulation of mitochondrial motility by calcium and Na/K-ATPase at nodes of Ranvier of myelinated nerves. J Neurosci **30**(10): 3555-3566.

Zhao, J., T. Liu, et al. (2011). Human MIEF1 recruits Drp1 to mitochondrial outer membranes and promotes mitochondrial fusion rather than fission. EMBO J. **30**: 2762.

Zheng, B., Z. Liao, et al. (2010). PGC-1alpha, a potential therapeutic target for early intervention in Parkinson's disease. Sci Transl Med **2**(52): 52ra73.

Zuchner, S., I. V. Mersiyanova, et al. (2004). Mutations in the mitochondrial GTPase mitofusin 2 cause Charcot-Marie-Tooth neuropathy type 2A. Nat Genet **36**(5): 449-451.

*Chapter 2***MOUSE LINES WITH PHOTO-ACTIVATABLE MITOCHONDRIA (PHAM) TO  
STUDY MITOCHONDRIAL DYNAMICS**

Anh H. Pham<sup>1</sup>, J. Michael McCaffery<sup>2</sup>, and David C. Chan<sup>1,3</sup>

<sup>1</sup>From the Division of Biology  
<sup>3</sup>Howard Hughes Medical Institute  
California Institute of Technology  
Pasadena, CA 91125

<sup>2</sup>Johns Hopkins University  
Integrated Imaging Center  
Department of Biology  
Baltimore, MD 21218

This chapter has been accepted in *Genesis*.

## ABSTRACT

Many pathological states involve dysregulation of mitochondrial fusion, fission, or transport. These dynamic events are usually studied in cells lines because of the challenges in tracking mitochondria in tissues. To investigate mitochondrial dynamics in tissues and disease models, we generated two mouse lines with photoactivatable mitochondria (*PhAM*). In the *PhAM*<sup>flaxed</sup> line, a mitochondrially localized version of the photoconvertible fluorescent protein Dendra2 (mito-Dendra2) is targeted to the ubiquitously expressed *Rosa26* locus, along with an upstream *loxP*-flanked termination signal. Expression of Cre in *PhAM*<sup>flaxed</sup> cells results in bright mito-Dendra2 fluorescence without adverse effects on mitochondrial morphology. When crossed with Cre drivers, the *PhAM*<sup>flaxed</sup> line expresses mito-Dendra2 in specific cell types, allowing mitochondria to be tracked even in tissues that have high cell density. In a second line (*PhAM*<sup>excised</sup>), the expression of mito-Dendra2 is ubiquitous, allowing mitochondria to be analyzed in a wide range of live and fixed tissues. By using photoconversion techniques, we directly measured mitochondrial fusion events in cultured cells as well as tissues such as skeletal muscle. These mouse lines facilitate analysis of mitochondrial dynamics in a wide spectrum of primary cells and tissues, and can be used to examine mitochondria in developmental transitions and disease states.

KEY WORDS: mitochondrial fusion, organelle trafficking, neurodegeneration, mouse model, Cre reporter.

## INTRODUCTION

In recent years, the dynamic properties of mitochondria have become increasingly appreciated. Mitochondria are dynamic and mobile organelles that continually undergo fusion and fission (division). These opposing processes control the morphology of mitochondria, and more importantly, also regulate their physiological functions Detmer and Chan (2007). As a result, mitochondrial fusion and fission impact cellular respiration, apoptosis, necrosis, and maintenance of mitochondrial DNA. Multiple neurodegenerative diseases have also been associated with defects in mitochondrial dynamics (Chen and Chan 2009).

Most studies of mitochondrial dynamics rely on cultured cells, where mitochondria can be imaged at high resolution. In cell lines, the fusion of mitochondria can be directly measured using photoactivatable fluorescent proteins targeted to the mitochondria (Karbowski, Arnoult et al. 2004). There is a pressing need to extend such studies to tissues, particularly where cell-based models are inadequate in recapitulating complex cellular interactions. It is important to be able to study a broad range of tissues, given that mitochondrial dynamics has been shown to affect the physiology of multiple systems, including the placenta, central nervous system, peripheral nervous system, skeletal muscle, and cardiac muscle (Alexander, Votruba et al. 2000; Delettre, Lenaers et al. 2000; Chen, Detmer et al. 2003; Zuchner, Mersiyanova et al. 2004; Chen, McCaffery et al. 2007; Waterham, Koster et al. 2007; Ishihara, Nomura et al. 2009; Wakabayashi, Zhang et al. 2009; Chen, Vermulst et al. 2010). Moreover, the metabolism of tissues can change during developmental transitions, and methods are needed to track mitochondria during such processes. To address this need, we have developed mouse models in which the

photoconvertible fluorescent protein Dendra2 can be used to track mitochondria. These mouse models allow mitochondria to be readily studied in fixed and live tissues. Furthermore, the photoswitchable properties of Dendra2 allow subsets of mitochondria to be precisely monitored within a dense mitochondrial network.

## RESULTS AND DISCUSSION

### Generation of mice with photoactivatable mitochondria

We used homologous recombination in mouse embryonic stem (ES) cells to insert an expression cassette containing mito-Dendra2 (a version of Dendra2 targeted to the mitochondrial matrix) into the ubiquitously expressed *Rosa26* locus. In the expression cassette, the CAG (cytomegalovirus/β-actin) enhancer-promoter drives strong expression, and a *loxP*-flanked (floxed) termination sequence upstream of mito-Dendra2 provides Cre-regulated expression (figure 2-1 A). Once mice were generated from correctly targeted embryonic stem cells (figure 2-1 B), the neomycin selection cassette was removed to generate the *PhAM*<sup>flaxed</sup> line (figure 2-1 A, C). In this mouse line, mito-Dendra2 expression relies on Cre-mediated excision of the termination sequence. These mice can be maintained as heterozygotes or homozygotes without apparent defects in viability or fertility.

To determine the potential of the *PhAM*<sup>flaxed</sup> line in tracking mitochondrial dynamics, tail fibroblasts were isolated for image analysis. No Dendra2 fluorescence was detected in these cells (figure 2-2 A left panel). Upon expression of Cre recombinase, the cells show bright green fluorescence that co-localizes precisely with HSP-60, a marker of the mitochondrial matrix (figure 2-2 A, right panel). The expression of mito-Dendra2 does not alter the morphology of the mitochondrial network (figure 2-2 B).

Taking advantage of the photoswitchable properties of Dendra2, we used a 405 nm laser to photoconvert a sub-population of mitochondria in live fibroblasts. After photoconversion, the mitochondria switch to red fluorescence (figure 2-2 C). In fluorescence time-lapse movies, we observed both transport and fusion of these labeled

mitochondria. Fusion events between the red and green mitochondria result in the transfer of fluorescence signal, an indication of matrix mixing (figure 2-2 C, D).

### **Widespread expression of mito-Dendra2**

We generated mice with ubiquitous expression of mito-Dendra2 by crossing the *PhAM*<sup>flaxed</sup> mice to *Meox2-Cre* mice. The resulting mouse line, referred to as *PhAM*<sup>excised</sup>, lacks the floxed termination cassette (figure 2-1 A, D). In tissue sections, all organs isolated from these animals exhibit bright mito-Dendra2 fluorescence localized specifically to the mitochondrial compartment. Widespread expression is found in the central nervous system, heart, testis, lung, liver, kidney, and thymus (figure 2-3). Therefore, the *PhAM*<sup>excised</sup> line can be used to survey mitochondrial morphology in a wide range of tissues. For example, cardiomyocytes contain linearly aligned mitochondria in contrast to the punctate structures found in hepatocytes (compare figure 2-3 D to 2-3 G). Homozygous *PhAM*<sup>excised</sup> mice are viable and fertile.

### **Tracking of mitochondria in live cells and tissues**

Live cells can be isolated from *PhAM*<sup>excised</sup> mice to facilitate imaging of the mitochondrial network (figure 2-4). In live mouse sperm (figure 2-4 A), we observed a region of intense mito-Dendra2 fluorescence in the midpiece. This fluorescence pattern is consistent with ultrastructural data showing cylindrical packing of mitochondria around the midpiece of the spermatozoa (Cardullo and Baltz 1991). We were unable to resolve individual mitochondria, suggesting that these mitochondria are packed tightly. When a small portion of the midpiece was illuminated with the 405 nm laser, we found that the

photoconverted region was stable, indicating that the packed mitochondria are discrete and do not share matrix contents.

We also examined mitochondria in dissociated tissues and intact skeletal muscles. In collagenase-digested myofibers, mito-Dendra2 fluorescence is arranged in a repeating pattern of doublets (figure 2-4 B). In fixed myofibers, mito-Dendra2 signal localizes adjacent to the Z-disk marker,  $\alpha$ -actinin (figure 2-4 D). This pattern is consistent with ultrastructural studies showing the stereotyped architecture of mitochondria in skeletal muscle (Ogata and Yamasaki 1997). In dissociated cardiomyocytes, mitochondria are arranged in linear arrays (figure 2-4 C). In each case, a subpopulation of mitochondria can be labeled by photoconversion.

To test whether mitochondria can be tracked in live tissues, we monitored mitochondrial dynamics in whole extensor digitorum longus (EDL) muscles. By following a subset of photoconverted mitochondria over time, we observed mitochondrial fusion between intramyofibrillar mitochondria. The fusion events occurred along both the longitudinal and transverse axes of the myofiber (figure 2-4 E). Therefore, although mitochondria in skeletal muscle appear static and rigidly organized, they are dynamic and fusion competent. We previously observed that postnatal development of fast-twitch muscle is accompanied by a dramatic increase in mitochondrial DNA copy number (Chen, Vermulst et al. 2010). This observation suggests that mitochondria may play an important role in the development of skeletal muscle. To explore this idea, we analyzed mitochondrial morphology during the postnatal development of EDL muscle. In fixed whole mounts of EDL, we noted a dramatic remodeling of mitochondrial structure between postnatal day 11 and 30 (figure 2-4 F-H). In EDL muscle at postnatal day 11, the mitochondria appear as

elongated tubules oriented along the long axis of the muscle fiber (figure 2-4 F). By postnatal day 30, the mitochondria are punctate and organized into doublets (figure 2-4 H). These morphological observations in the *PhAM*<sup>excised</sup> muscles were confirmed by electron microscopy analysis of wild-type mice (figure 2-4 G, I). Taken together, these results suggest that extensive mitochondrial remodeling accompanies skeletal muscle development, and indicates that the *PhAM* mouse lines can be used to examine mitochondria in developmental processes.

### Cell-specific labeling of mitochondria

The experiments above indicate that the *PhAM*<sup>excised</sup> line can be used to monitor mitochondria in a wide range of cell types. In some tissues with high cell density and diversity, however, the near ubiquitous expression of mito-Dendra2 results in overlapping mitochondrial signals from multiple cells. In such cases, it would be advantageous to restrict labeling to a particular cell type. To test this idea, we crossed *PhAM*<sup>flaxed</sup> mice with the *Pcp2-Cre* line, which drives Cre expression in Purkinje neurons of the cerebellum. To facilitate high resolution imaging in brain tissue, we used organotypic culturing methods to maintain parasagittal cerebellar slices. Purkinje neurons in the cerebellum were identified by calbindin immunofluorescence. As expected, mito-Dendra2 expression is restricted to Purkinje neurons (figure 2-5 A-C). In these neurons, we noted several morphologically distinct populations of mitochondria (figure 2-5 D). Tubular mitochondria occupy the soma and primary dendrites, whereas focal clusters of smaller mitochondria appear in the secondary and tertiary dendrites. In these clusters, the mitochondria are densely packed, and individual organelles often cannot be distinguished without photoconversion.

Interestingly, when mito-Dendra2 expression is restricted by the *Pcp2-Cre* driver, the mitochondria in individual Purkinje cells are better resolved. In the *PhAM*<sup>excised</sup> line, the expression of mito-Dendra2 in granular cells and supporting cells obscures the tracking of mitochondria in Purkinje neurons beyond the soma and primary dendrites (compare figure 2-3 C to 2-5 C).

### Detection of mitochondrial defects in mutant mice

One of our motivations for constructing the *PhAM* mice was to facilitate the systematic evaluation of mitochondrial dynamics in mutant mouse models. To assess this possibility, we used the *PhAM*<sup>flaxed</sup> line to examine mitochondrial morphology in Purkinje neurons with a targeted deletion of *Mfn2*, which is important for mitochondrial fusion. We have previously shown that the loss of *Mfn2* results in mitochondrial abnormalities as well as degeneration of Purkinje neurons (Chen, McCaffery et al. 2007). Consistent with our previous study, cerebellar sections of *Mfn2* mutant mice show severe mitochondrial fragmentation and sparseness in the dendritic processes (figure 2-6).

The *PhAM*<sup>excised</sup> and *PhAM*<sup>flaxed</sup> mouse models provide new opportunities for assessing mitochondrial dynamics in mouse tissues and cells. Other mouse models with fluorescently labeled mitochondria exist (Misgeld, Kerschensteiner et al. 2007; Sterky, Lee et al. 2011; Magrane, Sahawneh et al. 2012), but our models are the first to combine both photoconversion and conditional expression in a wide spectrum of cell types. With ubiquitous expression of mito-Dendra2, the *PhAM*<sup>excised</sup> line should be useful to investigators surveying mitochondrial dynamics in diverse tissues. Mitochondrial defects in mutant mouse models can be readily screened by histological analysis. Moreover,

photoswitching of mito-Dendra2 enables high-resolution analysis and direct measurement of mitochondrial fusion in live cells. The *PhAM*<sup>flaxed</sup> line can be combined with Cre drivers to restrict mito-Dendra2 expression to specific cells, facilitating the analysis of mitochondria in tissues with high cell diversity. Finally, our analysis in skeletal muscle indicates that these mouse lines can be used to study structural changes in mitochondria that may accompany developmental transitions. Such remodeling events may be particularly important in tissues that undergo developmentally programmed changes in metabolism, activity, or oxygenation.

## MATERIALS AND METHODS

### Construction of the *PhAM*<sup>flaxed</sup> mouse line

The mito-Dendra2 expression cassette was assembled in a modified pBluescript shuttle plasmid (kindly provided by Dr. John Burnett). First, the CAG enhancer-promoter was transferred from Rosa26 mT/mG (Muzumdar, Tasic et al. 2007) with PmeI-SpeI restriction sites. Second, the floxed termination signal was excised as an EcoRI-SpeI fragment from pBS302 (Sauer 1993) and subcloned downstream of the CAG promoter. This floxed termination signal is composed of two *loxP* sites flanking the SV40 polyadenylation signal sequence. Third, the mitochondrial targeting sequence of subunit VIII of cytochrome *c* oxidase was fused to the N-terminus of Dendra2 (Evrogen) (Chudakov, Lukyanov et al. 2007) and cloned into the pcDNA3.1(+) vector (Invitrogen) containing the bovine growth hormone (bGH) polyadenylation signal. Fourth, the mito-Dendra2/bGH segment was cloned into the shuttle vector downstream of the floxed termination signal. Finally, the pCA mT/mG sequence from Rosa26 mT/mG was replaced with the expression construct. All plasmids were verified by DNA sequence analysis.

The targeting construct was linearized with PvuI and electroporated into low passage 129/SvEV ES cells as previously described (Chen, Detmer et al. 2003). Of 94 neomycin-resistant clones, four were correctly targeted, as determined by PCR and Southern blot analysis. One ES clone was injected into C57BL/6 blastocysts to generate chimeric mice. Founder chimeric mice were bred to C57BL/6 to confirm germLine transmission. The mice were then crossed with FLPeR mice (Farley, Soriano et al. 2000) to remove the neomycin-resistance cassette, thereby generating the *PhAM*<sup>flaxed</sup> line. The

*PhAM*<sup>floxed</sup> mice were crossed with the *Meox2-Cre* mice (Tallquist and Soriano 2000) to generate the *PhAM*<sup>excised</sup> line.

### Confirmation of the *PhAM*<sup>floxed</sup> and *PhAM*<sup>excised</sup> alleles

For Southern analysis, genomic DNAs were digested with HindIII and hybridized with the published probe from the pROSA26-5' plasmid (Soriano 1999). To genotype the *PhAM*<sup>floxed</sup> allele by PCR, the set of three primers were used: Rosa4 5'-TCAATGGGCAGGGGTCGTT (Zong, Espinosa et al. 2005), R26-F 5'-TCCTGGCTTCTGAGGACCGC, and R26-R 5'- TTCCCCTGCAGGACAACGCC. The wild-type allele yields a 150 bp band while the mito-Dendra2 insertion results in a 252 bp band. GermLine excision of the termination sequence was verified using the following set of primers: CAG 5'-TACAGCTCCTGGCAACGTGCT, Stop 5'-TGGCAGCAGATCTAACGGCCG, Dendra2 5' – GTTCACGTTGCCCTCCATGT. The lower 265 bp band is derived from the termination cassette whereas the upper 345 bp band represents Cre-mediated excision of the floxed region.

### Antibodies and cell stains

The following dyes were used: wheat germ agglutinin A594 (1:250, Molecular Probes), NeuroTrace fluorescent Nissl stain A640 (1:200, Molecular Probes), DAPI (300 nM, Molecular Probes), and Alexa Fluor 546 streptavidin (1:500, Molecular Probes). Primary antibodies included mouse anti-Map2 (1:1000, Sigma), mouse anti-calbindin (1:1500, Sigma), goat anti-HSP60 (1:200, Santa Cruz), rabbit anti-Dendra2 (1:500, Evrogen), and mouse anti- $\alpha$ -actinin (1:100, Sigma). Secondary antibodies included

biotinylated goat anti-mouse (Vector labs), Alexa Fluor 546 donkey anti-goat, Alexa Fluor 546 donkey anti-mouse, and Alexa Fluor 488 goat-anti-rabbit (1:500, Molecular probes).

### Histological analysis

For all histological sections, mice were perfused transcardially with phosphate buffered saline (PBS) followed by 10% formalin (Sigma). Tissues were embedded overnight at 4°C in 30% sucrose solution and frozen in OCT for sectioning by a cryostat. For fluorescence staining, slides were either incubated with primary antibodies overnight or overlaid with WGA or Nissl stain for 1 to 2 hrs at room temperature.

For organotypic slices, membranes surrounding the cerebellum were trimmed and fixed overnight with 4% paraformaldehyde-lysine-periodate fixative at 4°C. Slices were permeabilized with 1% Triton-X for 15 min and incubated with blocking buffer (2% goat serum, 1% BSA, and 0.1% Triton-X) for 4-6 hrs. Samples were incubated with primary antibodies overnight followed by secondary antibodies for 2 hrs.

To stain muscles, EDL samples were fixed for 1 hour at room temperature with 10% formalin. Myofibers were mechanically teased apart and immunostained with the Vector M.O.M. kit (Vector labs, Burlingame, CA) according to the manufacturer's protocol.

### Fibroblast cells

Tail fibroblasts were isolated from the wild-type or *PhAM*<sup>flaxed</sup> line by trypsin-EDTA digestion of skin fragments from the tail. After several days in culture with media containing DMEM, 10% fetal bovine serum, 1 mM L-glutamine, and 1x

penicillin/streptomycin (Life Technologies/GIBCO, Carlsbad, CA), fibroblasts from hair follicles migrated onto the plate. To facilitate immortalization, these fibroblasts were transduced with retrovirus harboring SV40 large T antigen. For assessment of mitochondrial morphology, fibroblasts were plated in 8-well chamber slides. In each well, 200 cells were classified into one of three mitochondrial profiles: 100% tubular, 50% mixture of fragmented and short tubules, or completely fragmented.

### **Isolated cells and tissues**

To isolate primary cardiomyocytes for live imaging of mitochondrial dynamics, the ventricles were rinsed with cold PBS supplemented with 10 mg/mL of glucose and mechanically minced in 0.5% collagenase PBS buffer. The tissue was digested in 20 min intervals at 37°C in a rotary shaker, and myocyte supernatants were collected and pooled between digestion intervals until minimal ventricular tissues remained. Only rod shaped ventricular myocytes were selected for imaging.

For primary myofibers, the EDL muscle was digested with 0.2% collagenase in DMEM media for 2 hrs at 37°C in a rotary shaker. Digested EDL muscles were triturated several times using decreasing bore sizes of flame-heated pasteur pipettes to obtain individual myofibers for live imaging. For whole muscle imaging, the EDL was removed, placed in a coverglass bottom petri dish, and held in place using a slice anchor (Warner instruments, Hamden, CT). Whole muscles were imaged in media containing DMEM (no phenol red), 10% fetal bovine serum, 1 mM pyruvate, and 25 mM HEPES.

Mouse sperm were isolated from the cauda epididymus of 2-3 months old males. Longitudinal cuts were made along the epididymus to enable motile, mature sperm to swim

out into the PBS solution. All live samples were imaged on a stage-top heated platform maintained at 37°C.

### **Organotypic slice cultures**

Pups from postnatal days 10-12 were used for organotypic cultures. Tail samples from each animal were retained for genotyping. The cerebellum was removed and incubated in ice-cold preparation media containing 1X GBSS (Sigma) supplemented with 6.5 mg/mL of glucose. Each hemisphere was glued onto a rotating magnetic stage for sectioning by a Leica VT1200S vibratome. For each animal, approximately 4-6 sections (2-3 per hemisphere) of 330 µm thickness were collected and transferred to a petri dish with cold preparation media using a wide bore pipette. Evenly sliced sections were selected under the dissecting scope and transferred to Millicell membrane inserts (Millipore, PICM3050) in a 6 well plate. Typically, 2-4 sections were plated onto one insert for culturing by the interface method at 35°C with 5% CO<sub>2</sub> (Stoppini, Buchs et al. 1991). The culture medium is a mixture of MEM (Life Technologies, 51200), 2 mM L-glutamine, 1 mM GlutaMAX (Life Technologies, 35050), 0.5 mg/mL penicillin-streptomycin, 50% heat-inactivated horse serum, 25% Hank's salt solution, 10 mM HEPES, and 6.5mg/mL of glucose. The media was buffered to a pH of 7.2. Slices were fed with new media on alternating days 3 times a week and equilibrated in culture for at least 10 days prior to experimentation.

### Image analysis

Fluorescence images were acquired with a Zeiss LSM 710 confocal microscope with EC-Plan-Neofluar 40X/1.3 oil and Plan-APOCHROMAT 63X/1.4 oil objectives. Z-stack acquisitions oversampled each optical slice twice, and the Zen 2009 image analysis software was used for maximum z-projections. The 488 nm laser line and the 561 nm laser excited Dendra2 in the unconverted state and photoconverted state, respectively. To photoswitch Dendra2, a region was illuminated with the 405 nm line (4% laser power) for 30-60 bleaching iterations at a scan speed of 6.3–12.61  $\mu$ s/pixel. Alexa 594 and Alexa 640 conjugated dyes were excited by the 561 nm laser and the 633 nm laser, respectively. For live imaging of primary cardiomyocytes, sperm, and myofibers, the C-APOCHROMAT 63X/1.2W objective was used.

For EM, the EDL muscle was immobilized in an outstretched position by tying onto a toothpick splint prior to excision. Muscles were fixed in 3% paraformaldehyde, 1.5% glutaraldehyde, 100 mM cacodylate (pH 7.4), and 2.5% sucrose for 1 hour and stored in PBS. Samples were processed and imaged as described previously (Chen, McCaffery et al. 2007).

## FIGURE LEGENDS

**Figure 2.1. Construction of *PhAM*<sup>flaxed</sup> and *PhAM*<sup>excised</sup> mouse lines.** (A) Targeting of mito-Dendra2 into the *Rosa26* locus. Schematic 1 represents the wild-type *Rosa26* locus. The targeting construct (schematic 2) contains a floxed termination signal upstream of mito-Dendra2 and flanking sequences from the *Rosa26* genomic DNA, followed by a diphtheria toxin expression cassette. Homologous recombination in embryonic stem cells results in insertion of the construct into the *Rosa26* locus (schematic 3). In mice, removal of the neomycin selection marker by flippase (Flp) recombinase results in the *PhAM*<sup>flaxed</sup> line (schematic 4), which can be mated to a Cre driver line to obtain cell-specific labeling of mitochondria. GermLine excision of the termination signal produced the *PhAM*<sup>excised</sup> line (schematic 5). PGK-DTA, phosphoglycerate kinase promoter driving diphtheria toxin; CAG, cytomegalovirus/β-actin enhancer-promoter; black arrowheads, *loxP* sites; stop symbol, termination cassette; PGK-Neo, phosphoglycerate kinase promoter driving the neomycin-resistance gene; gray diamonds, flippase recognition target (*frt*) sites; half arrows, PCR primers for genotyping; short horizontal line, probe for Southern blot. (B) Representative Southern blot analysis of ES cell clones. Genomic DNA was digested with HindIII and hybridized with the *Rosa26* probe indicated in schematic 1 of (A). (C) PCR genotyping of the *PhAM*<sup>flaxed</sup> strain for the wild-type or knock-in allele using the set of three primers in schematic 3 of (A). (D) PCR genotyping of the *PhAM*<sup>excised</sup> strain using the three primers in schematic 4 of (A).

**Figure 2.2. Tracking of mitochondria in *PhAM*<sup>flaxed</sup> tail fibroblasts.** (A) Representative images of mitochondria in tail fibroblasts cultured from the *PhAM*<sup>flaxed</sup> mice. Tail

fibroblasts were cultured in the absence (left) or presence of Cre-expressing retrovirus (right). Mitochondria are identified by immunostaining for HSP60 (red), a mitochondrial marker. The mito-Dendra2 fluorescence (green) was found only after expression of Cre (yellow color indicates co-localized signals of Dendra2 and HSP60). Mitochondrial morphology remains tubular (inset). Scale bar is 10 mm. (B) Quantification of mitochondrial morphology in wild-type and *PhAM*<sup>flaxed</sup> fibroblasts. The table shows the percentage of cells with the indicated morphology  $\pm$  SEM ( $n=4$ ). (C) Monitoring mitochondrial fusion in *PhAM*<sup>flaxed</sup> fibroblasts. A subset of mitochondria was photoconverted (red) and tracked by time-lapse imaging. Three still images from the resulting movie highlight a mitochondrial fusion event (arrowhead) and exchange of matrix contents. Scale bar is 5 mm. (D) Fluorescence line analysis of the two mitochondria undergoing fusion in the frames from (C). Each plot measures the red and green signals along the drawn line. The line analysis demonstrates that mitochondrial fusion results in the transfer of red fluorescence to the adjoining mitochondrion.

**Figure 2.3. Ubiquitous expression of mito-Dendra2 in *PhAM*<sup>excised</sup> tissues.** Frozen tissue sections from the *PhAM*<sup>excised</sup> mice. (A) pyramidal neurons in the cortex; (B) pyramidal neurons in the hippocampus; (C) Purkinje neurons of the cerebellum; (D) myocardium; (E) testis; (F) lung; (G) liver cannula, inset shows magnified image of the boxed region; (H) kidney cortex; (I) thymus. Cell counter stains are shown in red or purple. In (A-B), anti-Map2 (red) stains the dendritic processes of neurons; in (A-B), a fluorescent Nissl stain (purple) marks neurons; in (C), anti-calbindin (red) highlights Purkinje neurons; in (D-I), wheat germ agglutinin (WGA) labels cell borders. Scale bars, 10 mm.

**Figure 2.4. Imaging of mito-Dendra2 in live isolated cells.** The fluorescence of mito-Dendra2 (green) was imaged in a (A) spermatocyte, (B) myofiber, and (C) cardiomyocyte. In each case, a subset of mitochondria was irradiated with a 405 nm laser to photoswitch mito-Dendra2 (red). (D) Comparison of mito-Dendra2 (green) in a fixed myofiber with the Z-disc marker  $\alpha$ -actinin (red). Since the myofiber in (D) was processed for immunostaining, the resolution of mitochondrial doublets is lower than (B). (E) Detection of mitochondrial fusion in isolated EDL muscle from a 2-month-old animal. A subset of mitochondria was photoconverted and tracked. Intensity maps of the photoconverted signal show two mitochondrial fusion events (marked by arrowheads) over a 12-minute period. In the top fusion event, the transfer of red signal into an unconverted mitochondrion was detected. In the bottom event, fusion occurs between two photoconverted mitochondria and results in equalization of the intensity. Intensity values of the heat maps are indicated in the legend. Scale bars: 10 mm for sperm and 5 mm for myofibers and cardiomyocyte. (F, H) Changes in mitochondrial structure during postnatal muscle development. Whole EDL muscles were isolated and imaged by mito-Dendra2 fluorescence at indicated ages. Scale bars: 5 mm. (G, I) Ultrastructural analysis of fixed EDL sections. Mitochondria are indicated by arrowheads. Scale bars: 10 mm.

**Figure 2.5. Purkinje-specific labeling of mitochondria.** *PhAM*<sup>flaxed</sup> mice were crossed with a Purkinje-specific driver, *Pcp2 Cre*, and organotypic slice cultures were prepared from the offspring. (A) Merged image of mito-Dendra2 (green) and anti-calbindin (red). Two Purkinje cells express mito-Dendra2. (B) Single-channel image of anti-calbindin

highlighting the borders of Purkinje neurons. (C) Single-channel image of mito-Dendra2 signal. (D) Zoomed image of the boxed region in (C). Note the tight clusters of mitochondria in the distal dendritic branches. Scale bars: 10 mm.

**Figure 2.6. Visualization of mitochondrial defects in Purkinje neurons lacking *Mfn2*.**

Frozen sections of cerebellum with stained for calbindin (red) and Dendra2 (green). The top panel is from a control animal with normal Purkinje neurons. The bottom panel is from a littermate lacking *Mfn2* in Purkinje neurons due to the *Pcp2 Cre* driver. The last column shows zoomed images of the boxed regions. Scale bar: 10 mm in the merged image and 5 mm in the zoomed image.

Figure 2.1

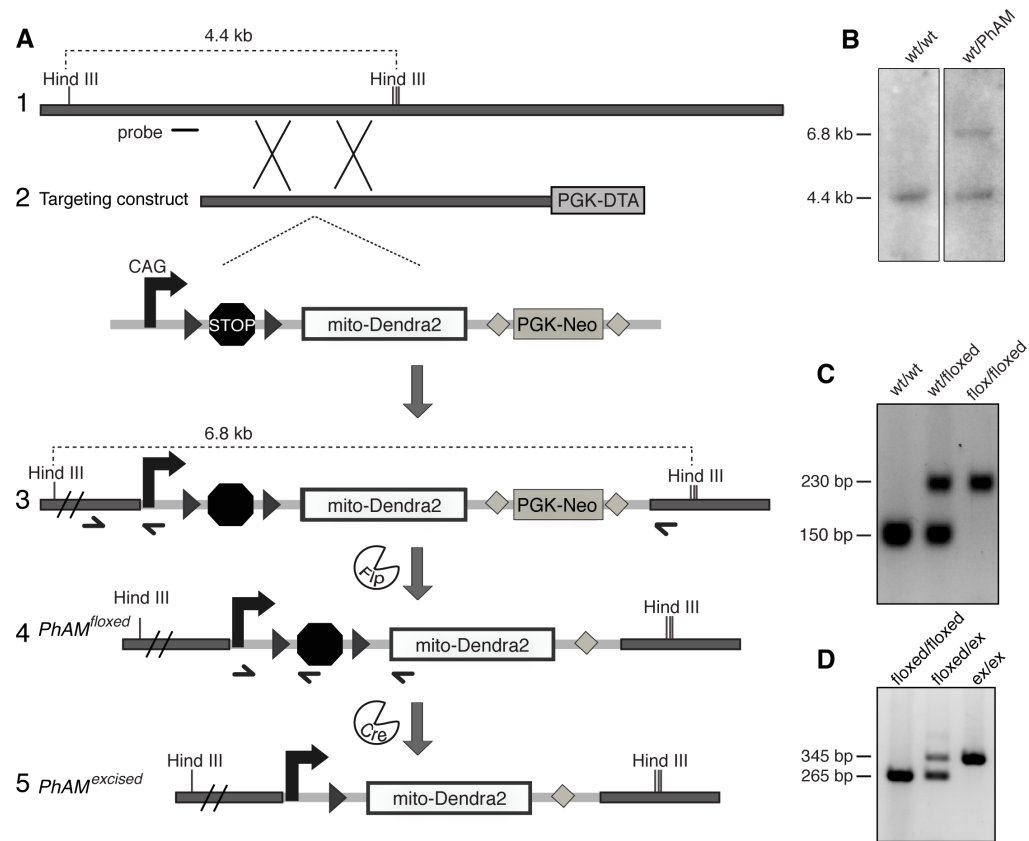


Figure 2.2

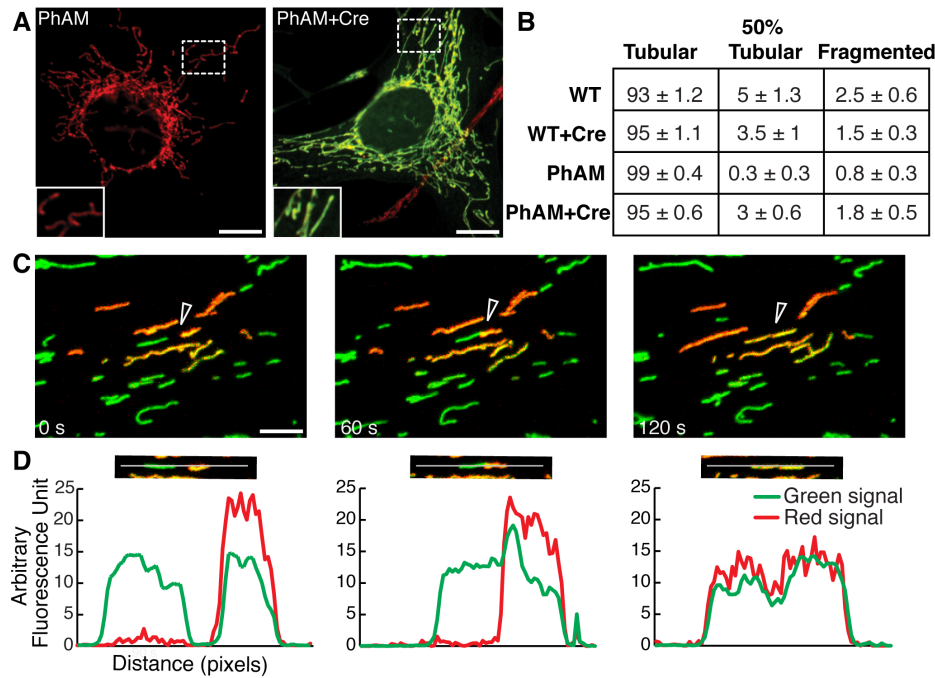


Figure 2.3

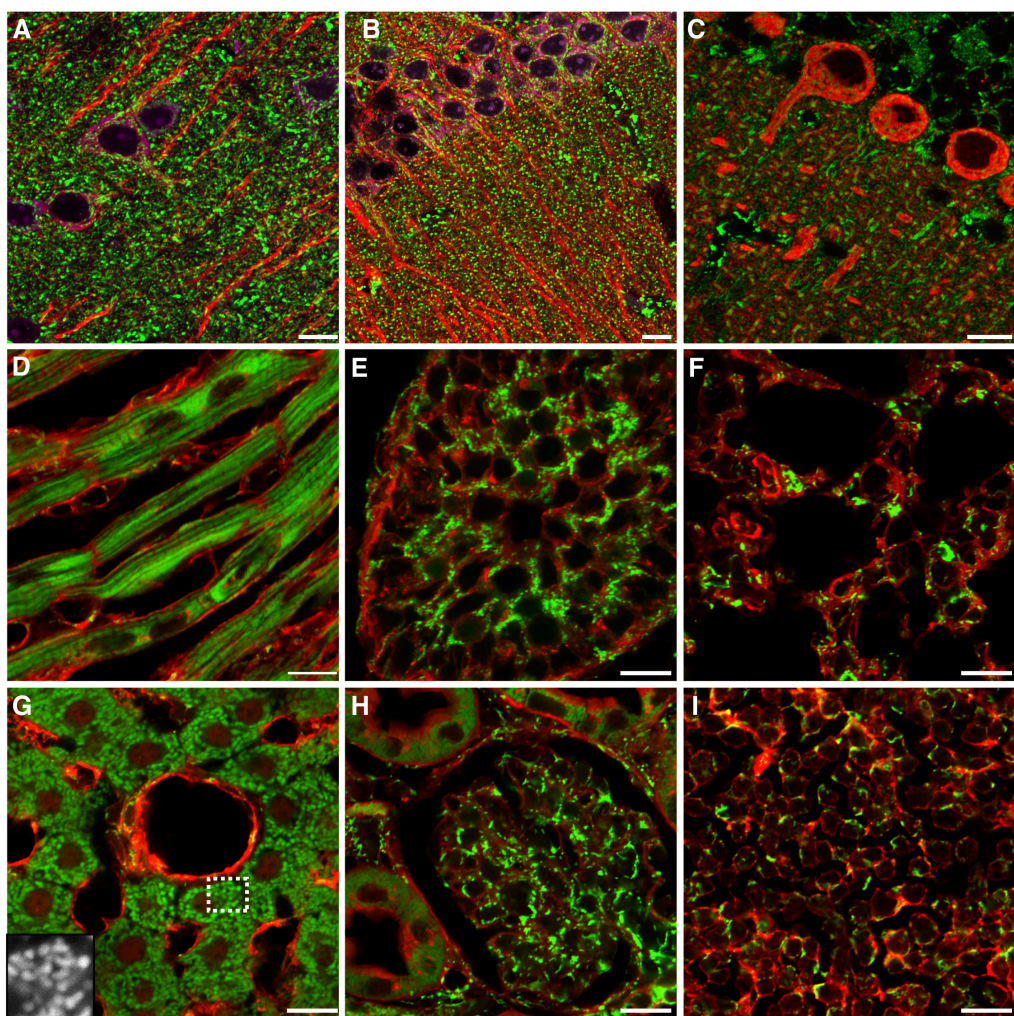


Figure 2.4

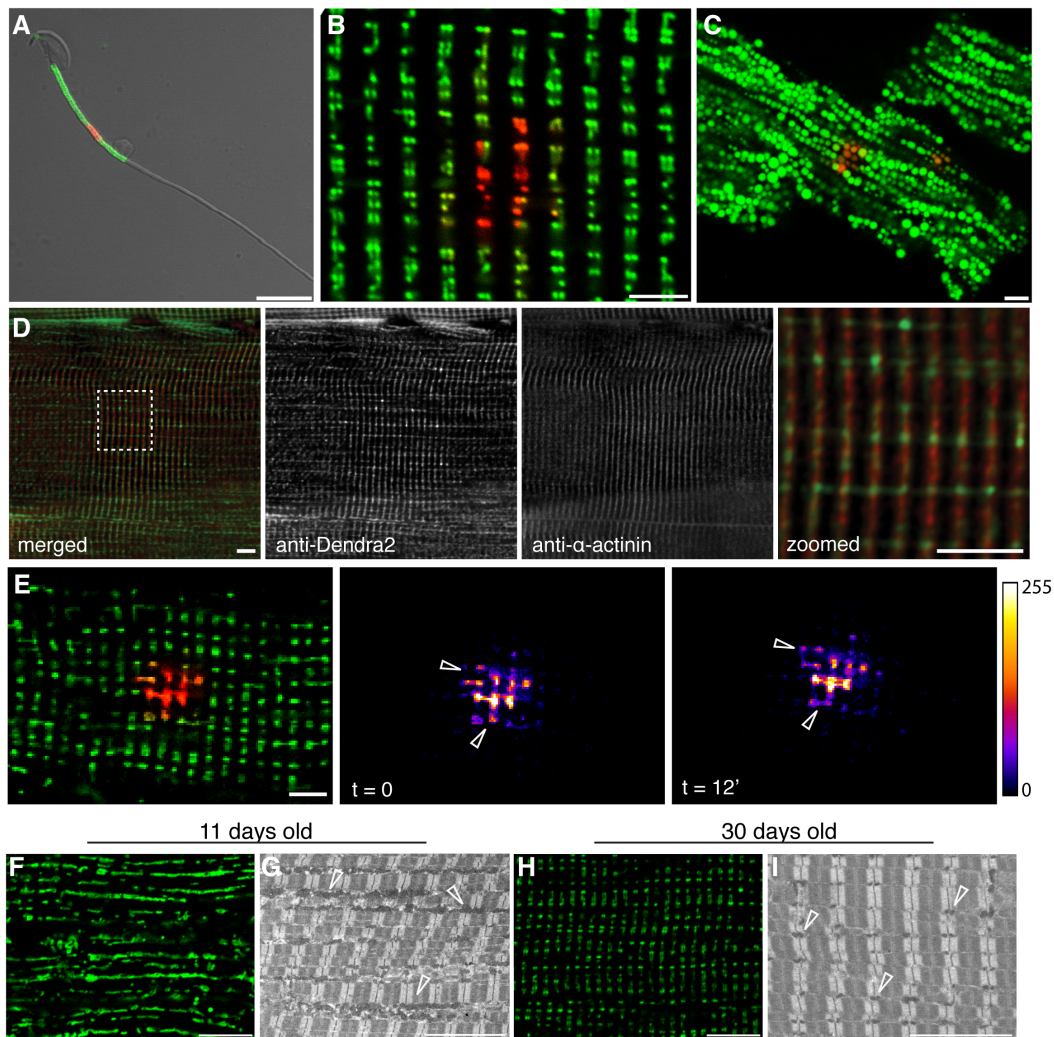


Figure 2.5

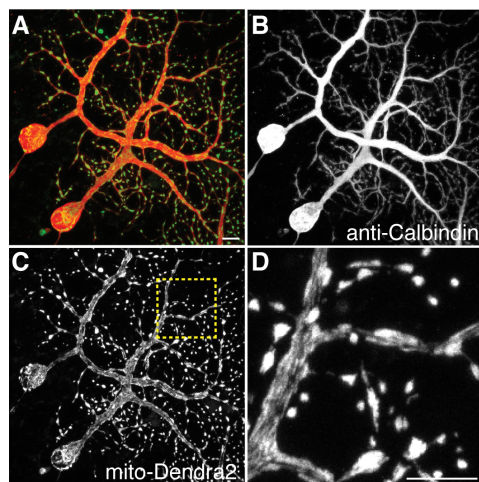
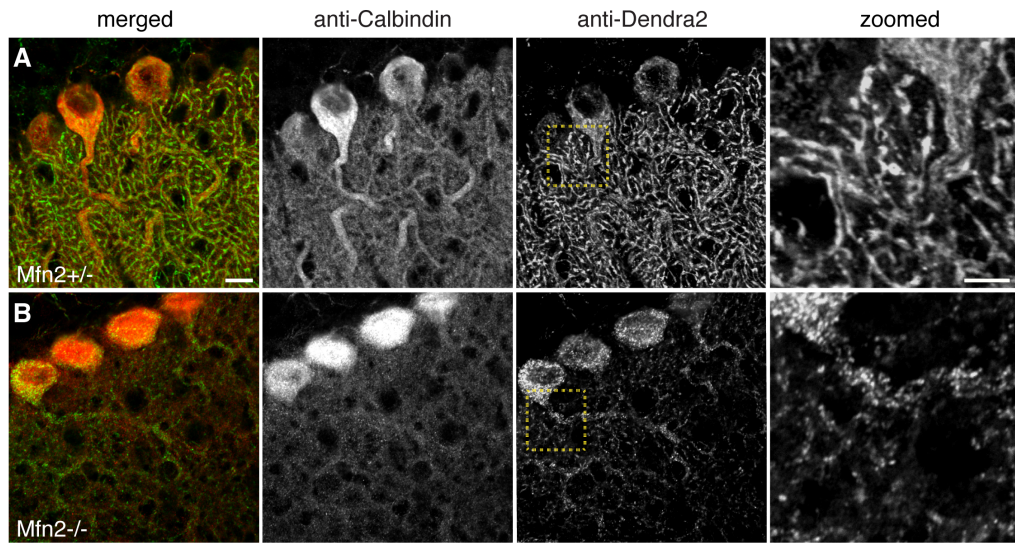


Figure 2.6



## REFERENCES

- Alexander, C., M. Votruba, et al. (2000). OPA1, encoding a dynamin-related GTPase, is mutated in autosomal dominant optic atrophy linked to chromosome 3q28. Nat Genet **26**(2): 211-215.
- Cardullo, R. A. and J. M. Baltz (1991). Metabolic regulation in mammalian sperm: mitochondrial volume determines sperm length and flagellar beat frequency. Cell Motil Cytoskeleton **19**(3): 180-188.
- Chen, H. and D. C. Chan (2009). Mitochondrial dynamics--fusion, fission, movement, and mitophagy--in neurodegenerative diseases. Hum Mol Genet **18**(R2): R169-176.
- Chen, H., S. A. Detmer, et al. (2003). Mitofusins Mfn1 and Mfn2 coordinately regulate mitochondrial fusion and are essential for embryonic development. J Cell Biol **160**(2): 189-200.
- Chen, H., J. M. McCaffery, et al. (2007). Mitochondrial fusion protects against neurodegeneration in the cerebellum. Cell **130**(3): 548-562.
- Chen, H., M. Vermulst, et al. (2010). Mitochondrial fusion is required for mtDNA stability in skeletal muscle and tolerance of mtDNA mutations. Cell **141**(2): 280-289.
- Chudakov, D. M., S. Lukyanov, et al. (2007). Tracking intracellular protein movements using photoswitchable fluorescent proteins PS-CFP2 and Dendra2. Nat Protoc **2**(8): 2024-2032.
- Delettre, C., G. Lenaers, et al. (2000). Nuclear gene OPA1, encoding a mitochondrial dynamin-related protein, is mutated in dominant optic atrophy. Nat Genet **26**(2): 207-210.

- Detmer, S. A. and D. C. Chan (2007). Functions and dysfunctions of mitochondrial dynamics. Nat Rev Mol Cell Biol **8**(11): 870-879.
- Farley, F. W., P. Soriano, et al. (2000). Widespread recombinase expression using FLPeR (flipper) mice. Genesis **28**(3-4): 106-110.
- Ishihara, N., M. Nomura, et al. (2009). Mitochondrial fission factor Drp1 is essential for embryonic development and synapse formation in mice. Nat Cell Biol **11**(8): 958-966.
- Karbowski, M., D. Arnoult, et al. (2004). Quantitation of mitochondrial dynamics by photolabeling of individual organelles shows that mitochondrial fusion is blocked during the Bax activation phase of apoptosis. J Cell Biol **164**(4): 493-499.
- Magrane, J., M. A. Sahawneh, et al. (2012). Mitochondrial dynamics and bioenergetic dysfunction is associated with synaptic alterations in mutant SOD1 motor neurons. J Neurosci **32**(1): 229-242.
- Misgeld, T., M. Kerschensteiner, et al. (2007). Imaging axonal transport of mitochondria in vivo. Nat Methods **4**(7): 559-561.
- Muzumdar, M. D., B. Tasic, et al. (2007). A global double-fluorescent Cre reporter mouse. Genesis **45**(9): 593-605.
- Ogata, T. and Y. Yamasaki (1997). Ultra-high-resolution scanning electron microscopy of mitochondria and sarcoplasmic reticulum arrangement in human red, white, and intermediate muscle fibers. Anat Rec **248**(2): 214-223.
- Sauer, B. (1993). Manipulation of transgenes by site-specific recombination: use of Cre recombinase. Methods Enzymol **225**: 890-900.

- Soriano, P. (1999). Generalized lacZ expression with the ROSA26 Cre reporter strain. Nat Genet **21**(1): 70-71.
- Sterky, F. H., S. Lee, et al. (2011). Impaired mitochondrial transport and Parkin-independent degeneration of respiratory chain-deficient dopamine neurons in vivo. Proc Natl Acad Sci U S A **108**(31): 12937-12942.
- Stoppini, L., P. A. Buchs, et al. (1991). A simple method for organotypic cultures of nervous tissue. J Neurosci Methods **37**(2): 173-182.
- Tallquist, M. D. and P. Soriano (2000). Epiblast-restricted Cre expression in MORE mice: a tool to distinguish embryonic vs. extra-embryonic gene function. Genesis **26**(2): 113-115.
- Wakabayashi, J., Z. Zhang, et al. (2009). The dynamin-related GTPase Drp1 is required for embryonic and brain development in mice. J Cell Biol **186**(6): 805-816.
- Waterham, H. R., J. Koster, et al. (2007). A lethal defect of mitochondrial and peroxisomal fission. N Engl J Med **356**(17): 1736-1741.
- Zong, H., J. Espinosa, et al. (2005). Mosaic Analysis with Double Markers in Mice. Cell **121**(3): 479-492.
- Zuchner, S., I. V. Mersiyanova, et al. (2004). Mutations in the mitochondrial GTPase mitofusin 2 cause Charcot-Marie-Tooth neuropathy type 2A. Nat Genet **36**(5): 449-451.

*Chapter 3***LOSS OF *MFN2* RESULTS IN PROGRESSIVE, RETROGRADE DEGENERATION  
OF DOPAMINERGIC NEURONS IN THE NIGROSTRIATAL CIRCUIT**

Anh H. Pham<sup>1</sup>, Shuxia Meng<sup>1</sup>, Quynh N. Chu<sup>1</sup>, and David C. Chan<sup>1,2</sup>

<sup>1</sup>From the Division of Biology  
<sup>2</sup>Howard Hughes Medical Institute  
California Institute of Technology  
Pasadena, CA 91125

This chapter has been accepted in *Human Molecular Genetics*.

## ABSTRACT

Mitochondria continually undergo fusion and fission, and these dynamic processes play a major role in regulating mitochondrial function. Studies of several genes associated with familial Parkinson's disease (PD) have implicated aberrant mitochondrial dynamics in the disease pathology, but the importance of these processes in dopaminergic neurons remains poorly understood. Because the mitofusins Mfn1 and Mfn2 are essential for mitochondrial fusion, we deleted these genes from a subset of dopaminergic neurons in mice. Loss of *Mfn2* results in a movement defect characterized by hypoactivity, tremors, and a rearing defect. In open field tests, *Mfn2* mutants show severe, age-dependent motor deficits. These motor deficits are preceded by loss of dopaminergic terminals in the striatum. However, loss of dopaminergic neurons in the midbrain occurs weeks after the onset of these motor and striatal deficits, suggesting a retrograde mode of neurodegeneration. In our conditional knockout strategy, we incorporated a mitochondrially targeted fluorescent reporter to facilitate tracking of mitochondria in the affected neurons. Using an organotypic slice culture system, we detected fragmented mitochondria in the soma and proximal processes of these neurons. In addition, we found markedly reduced mitochondrial mass and transport, which may contribute to the neuronal loss. These effects are specific for *Mfn2*, as loss of *Mfn1* yielded no corresponding defects in the nigrostriatal circuit. Our findings indicate that perturbations of mitochondrial dynamics can cause nigrostriatal defects and may be a risk factor for the neurodegeneration in PD.

## INTRODUCTION

Parkinson's disease (PD) is a neurodegenerative movement disorder characterized by resting tremor, rigidity, bradykinesia, and postural instability. PD symptoms are classically attributed to dopamine depletion and the degeneration of dopaminergic neurons in the substantia nigra pars compacta (SNc). However, other neuronal circuits are affected, and non-motor symptoms suggest a systemic pathology. There is compelling evidence that mitochondrial dysfunction is a primary event in the disease process. Decreased mitochondrial electron-transport chain activity has been detected in tissues from PD patients (Schapira, Cooper et al. (1989); (Parker and Swerdlow 1998), and toxins that inhibit mitochondrial respiration can give rise to parkinsonism in humans and animal models (Langston, Ballard et al. 1983; Cannon and Greenamyre 2010). The most direct evidence, however, has come from the study of genes associated with familial forms of PD. Disruption of the PD-associated genes PINK1, Parkin, DJ-1, or LRRK2 results in mitochondrial defects and aberrant mitochondrial morphology (Greene, Whitworth et al. 2003; Clark, Dodson et al. 2006; Park, Lee et al. 2006; Irrcher, Aleyasin et al. 2010; Krebiehl, Ruckerbauer et al. 2010; Wang, Yan et al. 2012).

Fusion and fission are fundamental processes that control the function of mitochondria (Detmer and Chan 2007). Mitofusins Mfn1 and Mfn2 are outer membrane GTPases that mediate fusion of mitochondrial outer membranes by homotypic and heterotypic interactions. The optic atrophy protein OPA1 is necessary for the fusion of the mitochondrial inner membranes. The dynamin-related protein Drp1 mediates the opposing process of mitochondrial fission. Several neurodegenerative diseases, including PD, have been linked to perturbations in mitochondrial dynamics (Chen and Chan 2009).

Recently, this link has been strengthened by the analysis of genes that cause familial forms of PD. The PINK1/Parkin pathway is profoundly affected by mitochondrial fusion and fission. In *Drosophila*, PINK1 and Parkin loss-of-function mutants have severe mitochondrial defects, characterized by swollen mitochondria with abnormal cristae (Greene, Whitworth et al. 2003; Clark, Dodson et al. 2006; Park, Lee et al. 2006; Yang, Gehrke et al. 2006). These mitochondrial perturbations lead to dysfunction of the indirect flight muscles. The defects in mitochondria and muscles are efficiently rescued by the overexpression of Drp1 or knockdown of Marf (a fly ortholog of mitofusin) or OPA1 (Deng, Dodson et al. 2008; Poole, Thomas et al. 2008; Yang, Ouyang et al. 2008). In cultured mammalian cells, the PINK1/Parkin pathway has been shown to promote the elimination of dysfunctional mitochondria by the autophagy machinery. This degradative process, termed mitophagy, is dependent on mitochondrial fission (Twig, Elorza et al. 2008; Tanaka, Cleland et al. 2010). Disruption of DJ-1 function causes mitochondrial fragmentation and enhanced sensitivity to oxidative stress (Irrcher, Aleyasin et al. 2010; Krebiehl, Ruckerbauer et al. 2010; Thomas, McCoy et al. 2011; Wang, Petrie et al. 2012). Overexpression of PINK1 and Parkin in DJ-1 deficient cells rescues the fragmented mitochondrial morphology, suggesting regulation of mitochondrial dynamics by each pathway (Irrcher, Aleyasin et al. 2010; Thomas, McCoy et al. 2011). Finally, PD-associated mutations of LRRK2 in cells induce mitochondrial fragmentation and increased localization of Drp1 to the mitochondria (Wang, Yan et al. 2012).

These observations indicate that PD-related mutations and mitochondrial dynamics have a reciprocal relationship. PD-related mutations can perturb mitochondrial dynamics, and the consequences of these mutations can be modulated by mitochondrial dynamics.

These results highlight the need to understand the function of mitochondrial dynamics in dopaminergic neurons. To address this issue, we have analyzed the consequences of removing the mitofusins from dopaminergic neurons. We find that loss of *Mfn2* results in a severe movement disorder attributed to progressive degeneration of the nigrostriatal circuit.

## RESULTS

### **Deletion of *Mfn2* from dopaminergic neurons**

We utilized a genetic approach to assess the role of mitochondrial fusion in dopaminergic neurons. *Mfn1* and *Mfn2* conditional knockout mice were crossed to the *Slc6a3-Cre* driver (Bäckman, Malik et al. 2006), in which the endogenous dopamine transporter locus expresses Cre recombinase in the A8-A10 subset of dopaminergic neurons, including those of the SNc (figure 3.1 A). Our mating scheme also incorporated a Photoactivatable Mitochondria (PhAM) Cre reporter (Pham, McCaffery et al. 2012) for the dual purpose of labeling mitochondria and monitoring Cre-dependent excision. Mice with disruption of *Mfn1* show no phenotype up to 1 year of age (figure 3.6). In contrast, mice with disruption of *Mfn2* are hunched and hypoactive by 5 weeks of age when compared to wild-type or heterozygous *Mfn2* littermates. These mice also exhibit kyphosis, reduced activity, and tremor (figure 3.1 B). Weight gain is stagnant after 4 weeks of age, resulting in an increasingly larger weight difference between mutant and control littermates (figure 3.1 C).

In our initial cohort of *Mfn2* mutants, many animals died at approximately 6-7 weeks of age due to apparent malnutrition. Mutant animals ( $n = 15$ ) died or were culled due to significant weight loss between 36 and 48 days of age. These phenotypes resemble the

aphagia and adipsia found in models of dopamine depletion (Zhou and Palmiter 1995; Palmiter 2008). However, when supplied with hydrated gel packs and crushed pieces of regular chow on the cage floor, all mutant *Mfn2* mice survive beyond 6 months, with a majority surviving past 1 year of age. To minimize possible secondary effects due to malnutrition, the phenotypic analyses reported below were performed using mutant and control mice provided with this dietary supplementation.

### **Movement disorder in *Mfn2* mutants**

Because initial observations suggested that *Mfn2* mutant mice had reduced activity, we monitored their spontaneous movements in a longitudinal open field study. *Mfn2* mutant mice show an age-dependent decline in locomotive activity (figure 3.2 A). At 4-5 weeks, mutant animals travel only 68% of the distance traversed by wild-type control animals. This defect progresses over the next several weeks. By 8-11 weeks of age, the distance traveled by mutants reduces to 34% of wild-type controls (figure 3.2 B). In contrast, *Mfn2* heterozygous animals show normal locomotion. We compared the *Mfn2* homozygotes to both wild-type controls and heterozygous controls carrying *Slc6a3-Cre*, because the knock-in *Cre* allele causes a slight, insignificant, decrease in dopamine transporter levels in the heterozygous state (Bäckman, Malik et al. 2006). We found that *Mfn2* heterozygotes carrying *Slc6a3-Cre* are indistinguishable from wild-type controls in all the assays used in this study.

Similar to travel distance, the speed of movement exhibited by *Mfn2* mutant animals declines with age (figure 3.2 C). We also observed a strong rearing defect in mutant *Mfn2* mice that is present as early as 4 weeks of age (figure 3.2 D and). This

postural defect likely contributes to the starvation and dehydration observed at 6 weeks when cages are not supplemented with food and gel packs on the floor. Consistent with the decreased locomotion, *Mfn2* mutants spend twice as much time inactive at 6-7 weeks of age. By 8-11 weeks, this discrepancy increases to 6-fold (figure 3.2 E). Of note, the locomotive defect is specific for *Mfn2* mutants; *Mfn1* mutants show no motor deficiency in the open field test (figure 3.6). Moreover, the double *Mfn1/Mfn2* mutants do not have an exacerbated phenotype compared to *Mfn2* mutants (figure 3.7). Overall, measurements from the open field test suggest that, beginning at 4-5 weeks, *Mfn2* mutants exhibit progressive bradykinesia and a postural defect, both cardinal signs of PD.

### Retrograde degeneration of SNC dopaminergic neurons

To determine whether the motor deficits in mutant animals are accompanied by a loss of dopaminergic innervation, we used tyrosine hydroxylase (TH)-immunoreactivity to assess the nigrostriatal circuit. We first analyzed the striatum, the endpoint of the nigrostriatal pathway. Here, TH-staining marks the axon terminals derived from the SNC. In *Mfn2* mutants, the striatum shows a 25% reduction in dopaminergic terminals at 3 weeks of age (figure 3.3 A, C). Loss of TH-immunoreactivity is detected first in the dorsolateral striatum (figure 3.3 A, outlined region in 3 week sample) and gradually encompasses the entire striatum by 11 weeks. Interestingly, the regional severity of striatal loss in *Mfn2* mutants resembles the pattern described in PD patients (Kish, Shannak et al. 1988; Stoessl 2011). By 8-10 weeks, the depletion of dopaminergic terminals increases to 76% in *Mfn2* mutant animals (figure 3.3 C). In contrast, the projections to the nucleus accumbens (NAc) and olfactory tubercle (OT), which come from dopaminergic neurons in the ventral

tegmental area (VTA), appear to be more protected. These dopaminergic terminals, which are part of the mesolimbic pathway, are moderately preserved at 11-14 weeks (figure 3.3 A, outlined regions).

Moving upstream in the nigrostriatal circuit, we counted the number of TH-immunoreactive neurons in the SNC. In contrast to the striatum, there is no notable loss of neurons in the SNC at either 3 weeks or 8-9 weeks (figure 3.3 B, D). The earliest time point with neuronal loss occurs at 10-12 weeks, with a 52% decrease in TH-immunopositive neurons. Further degeneration followed at subsequent ages (figure 3.3 D). Additionally, the neurons remaining in *Mfn2* mutants appear to have smaller cell bodies as well as diminished neuronal processes (figure 3.3 E). Partial loss of neurons was also observed at the VTA but not to the extent of the SNC. Taken together, these results indicate two pertinent features of neurodegeneration in this mouse model. First, multiple types of dopaminergic neurons have a requirement for *Mfn2*, but the nigrostriatal circuit exhibits enhanced vulnerability compared to the mesolimbic pathway. Likewise, SNC neurons in PD patients are more severely affected than the VTA population (Hirsch, Graybiel et al. 1988; Damier, Hirsch et al. 1999). Second, the degeneration of *Mfn2*-deficient dopaminergic neurons occurs in a stepwise manner. The initial defects appear at the axon terminals, followed one to two months later by degeneration of the cell bodies.

### **Mitochondrial fragmentation and depletion in dopaminergic neurons**

We have previously generated a Cre reporter of mitochondrial dynamics that targets the photoconvertible fluorescent protein Dendra2 to the mitochondrial matrix (Pham, McCaffery et al. 2012). The expression of mito-Dendra2 relies on Cre-mediated excision

of an upstream *loxP*-flanked termination signal. In our mating scheme (Figure 3.1 A), mito-Dendra2 expression depends on the *Slc6a3-Cre* driver, thereby allowing us to visualize mitochondria within the affected neurons, a key benefit in the densely populated midbrain. We have also established a slice culture system to assess mitochondrial dynamics in *Mfn2*-null dopaminergic neurons. The organotypic culture system has been extensively used for long-term assessment of neuronal function and development *in vitro*, because it preserves the cytoarchitecture and circuitry between multiple brain regions (Gahwiler, Capogna et al. 1997; Cho, Wood et al. 2007). To best preserve the nigrostriatal connections, we sectioned the brains at an angle previously characterized to retain these projections (Beurrier, Ben-Ari et al. 2006; Ammari, Lopez et al. 2009).

In slice cultures from wild-type and heterozygous brains, we found that *Slc6a3-Cre*/mito-Dendra2 expression is specific for dopaminergic neurons, as evidenced by its restriction to cells with TH immunoreactivity (figure 3.4 A). The morphology of mitochondria in heterozygous slices has a mixed profile, consisting of both tubular structures in proximal processes and short puncta in distal projections. In *Mfn2*-null slices, we found swollen and fragmented mitochondria in the soma and proximal processes. Consistent with our histological analysis (figure 3.3 E), the *Mfn2* mutant neurons have fewer and thinner processes extending from the cell body (figure 3.4 A). In addition, the *Mfn2* mutant cultures contain many neurons that express mito-Dendra2 but lack or have reduced TH signal. The failure to maintain TH expression suggests that these neurons are in the early stages of degeneration (figure 3.4 A, starred neurons). We also noted a severe depletion of mitochondria in neuronal processes both proximal and distal to dopaminergic

cell bodies (figure 3.4 B). Mutant slices show a 70% reduction in mitochondrial mass after normalizing to mito-Dendra2-positive cell bodies (figure 3.4 C).

### **Decreased mitochondrial transport along nerve processes in *Mfn2* mutants**

To monitor mitochondrial transport along dopaminergic axons and dendrites, we performed live imaging of mito-Dendra2 in the slice cultures. For accurate monitoring of mitochondrial dynamics in the dense milieu of dopaminergic projections, we photoconverted mitochondria in a nerve process and tracked the movement of this labeled subpopulation (figure 3.5 A, top). From the time-lapse movies, we generated kymograph representations that resolved the complex trajectories of the photoconverted mitochondria (figure 3.5 A, bottom). With a vertical time axis, mobile mitochondria create diagonal tracks, whereas stationary mitochondria project as vertical streaks. Consistent with previous studies describing the mobility of mitochondria in neuronal processes (Misgeld, Kerschensteiner et al. 2007; Kang, Tian et al. 2008; Sheng and Cai 2012), we found that a subpopulation of mitochondria is highly mobile in heterozygous control dopaminergic neurons (figure 3.5 A). In contrast, mitochondrial transport is minimal in *Mfn2*-null neurons (figure 3.5 B). In heterozygous controls, 50% of photoconversion experiments resulted in at least one transport event, defined as directed movement for 5 mm. In *Mfn2* mutants, only 14% of photoconversion experiments showed a transport event (Figure 3.5 C). Additionally, mobile mitochondria in mutant dopaminergic neurons exhibit more intermittent movements and longer immobile periods. As a result, the average velocity for mitochondria in *Mfn2*-null slices is also slower relative to controls, 0.05  $\mu\text{m/s}$  versus 0.15  $\mu\text{m/s}$  (figure 3.5 D).

## DISCUSSION

Several genes associated with familial PD—including PINK1, Parkin, DJ-1, and LRRK2—have been associated with mitochondrial dynamics. As a result, we sought to understand the role of mitochondrial dynamics in the nigrostriatal pathway. We deleted the mitofusins *Mfn1* and *Mfn2* from a subset of dopaminergic neurons, including those of the SNc. *Mfn2* homozygous mutants exhibit severe locomotive defects, which are preceded by the loss of dopaminergic efferents to the striatum. Importantly, these mice show dopaminergic depletion in the striatum and motor deficits weeks earlier than the loss of nigral neurons. This sequence of pathological findings is consistent with retrograde degeneration, in which neuronal deficits initiate distally in the axon terminals and progress backwards to the cell bodies. Interestingly, pathological studies of PD brains have suggested a similar dying back mode of neurodegeneration based on the disproportionate loss of striatal dopamine relative to the neuronal loss in the SNc (Hornykiewicz 1998; Cheng, Ulane et al. 2010). Administration of MPTP to rhesus monkeys also produces this differential pattern of neuronal damage (Pifl, Schingnitz et al. 1991).

We found that dopaminergic neurons lacking *Mfn2* have a prominent defect in mitochondrial content and transport in neuronal processes. This latter observation supports growing evidence that the mitofusins are important for mitochondrial movement (Chen, Detmer et al. 2003; Misko, Jiang et al. 2010). Mechanistically, this link may be related to the observation that Mfn2 can co-immunoprecipitate with exogenously expressed Miro and Milton, which are important components for kinesin-mediated transport of mitochondria along microtubules (Misko, Jiang et al. 2010).

The identification of PD-related genes, such as  $\alpha$ -synuclein, PINK1, Parkin, DJ-1, and LRRK2, has led to the development of numerous mouse models of PD. Although some of these models show modest decreases of striatal dopamine and associated motor impairments, they generally fail to recapitulate the progressive loss of dopaminergic neurons that is the pathological hallmark of PD (Dawson, Ko et al. 2010; Chesselet and Richter 2011). We find that dopaminergic neurons deficient in *Mfn2* exhibit early deficits at the nerve terminals and progressive loss over the course of several months. The time span between distal defects and cell loss presents a window for investigating the cellular mechanisms leading to degeneration of dopaminergic neurons.

## MATERIALS AND METHODS

**Generation of *Mfn* mutant mice.** Conditional mouse lines of *Mfn1* and *Mfn2* have been previously described (Chen, McCaffery et al. 2007). The PhAM Cre reporter is detailed (Pham, McCaffery et al. 2012). The *Slc6a3-Cre* driver was obtained from the Jackson Laboratory (B6.SJL-*Slc6a3tm1.1(cre)Bkmn*/J). All experiments were approved by the Caltech Institute Animal Care and Use Committee.

**Open field test.** Animals were placed in a 50 cm by 50 cm white Plexiglass box and allowed an adaptation period of 30-60 minutes prior to being analyzed. Activity was recorded for two consecutive sessions, each lasting 15 minutes, by a ceiling-mounted video camera. The Ethovision software (Noldus, Leesburg, VA) was used to measure the distance, velocity, rearing frequency, and immobility of the mice.

**Histological analysis.** Animals were sacrificed after anesthesia with halothane. Brains were dissected and fixed overnight at 4°C in 10% neutral buffered formalin. The caudal portions of the brains were trimmed in an acrylic matrix (2 mm from the end) before specimens were mounted and sectioned with the Leica VT1200S vibratome. Brains were sliced into consecutive sections of 50 µm for the striatum or 35 µm for the midbrain. For counting, every 4th midbrain slice was processed for TH (1:1000, Chemicon) immunohistochemistry following the manufacturer's protocol (Vectastain elite ABC kit, Vector Labs). To enhance antigenicity, slides were boiled for 40 min in 10 mM sodium citrate buffered at pH 6. Sections were developed with 3,3'-diaminobenzidine and subsequently immersed in a 0.1% cresyl violet acetate solution for Nissl counterstain. Each

slide contained a set of homozygous, heterozygous, and wild-type samples to minimize staining variability between samples. Two reviewers, blinded to the genotypes, counted TH-immunoreactive and Nissl-positive cells at 100X magnification. For each animal, 9 sections spanning the midbrain were counted. Total counts from the heterozygotes and homozygotes were normalized to the age-matched wild-type controls. Densitometry of the TH signal in the striatum has been described (Gunapala, Chang et al. 2010). Briefly, the Nikon Elements software was used for computer-assisted measurement of TH intensity in the striatal area. The same threshold was maintained across all samples on the slide. For each animal, 3 sections, spanning the rostral-caudal extent of the striatum, were measured, summed, and normalized to wild-type measurements.

**Imaging and microscopy analysis.** Images were acquired on a Zeiss LSM 710 confocal microscope using EC-Plan-Neofluar 40X/1.3 oil or Plan-APOCHROMAT 63X/1.4 oil objectives. Z-stack acquisitions oversampled twice the thickness of the optical slice, and Zen 2009 analysis software was used for maximum z-projections. To photoconvert Dendra2, a small region was irradiated with the 405 nm laser (4% laser power) for 60 iterations at a scan speed of 6.3–12.61  $\mu$ s/pixel. For live imaging, slices were submerged in Tyrode's buffer (Sigma) supplemented with 25 mM HEPES and 6.5mg/mL glucose and stabilized with a slice anchor (Warner Instruments). Slices were imaged on a stage-top heated platform maintained at 35°C. Four fields were imaged in each slice and time-lapse movies were acquired at 20 s intervals for 15 minutes. Custom macros were written for ImageJ software to produce kymographs and to measure velocity traces. In quantifying mitochondrial area, noise reduction in maximally z-projected images utilized the median

and Liptschitz top hat filters. Subsequently, the dynamic thresholding plugin was applied to segment mitochondria, and the *Analyze particles* algorithm in ImageJ provided quantitation of mitochondrial signal. Manual counts of mito-Dendra2-positive cells in the z-stacks used the *Cell counter* algorithm.

**Organotypic slice cultures.** Preparations of sagittal organotypic slices have been described (Kearns, Scheffler et al. 2006). We made modifications to the angle of sectioning to improve preservation of nigrostriatal projections (Beurrier, Ben-Ari et al. 2006). The rotating magnetic stage from the Leica VT1200S vibratome was tilted so that sections could be acquired between 10° and 15° from the midline. Pups were sacrificed at postnatal day 10-12. Typically, only two slices (one per hemisphere) of 330 µm thickness contained the nigrostriatal pathway. Slices acquired between 1 mm and 1.2 mm lateral from the midline were retained for culturing. Cultures were fed 3 times a week using Stoppini media (Stoppini, Buchs et al. 1991). Brain slices were equilibrated in culturing conditions for at least 2 weeks prior to experimentation. For immunofluorescence, membranes around the slices were trimmed and fixed in 4% paraformaldehyde-lysine-periodate overnight at 4°C. Slices were permeabilized with 1% Triton X-100 for 30 minutes and incubated with blocking buffer (2% goat serum, 1% BSA, and 0.1% Triton-X100) for 4-6 hours at room temperature. Samples were incubated with anti-TH antibody overnight at 4°C, followed by secondary antibody (goat anti-rabbit IgG Alexa 568, Molecular Probes) for 2 hours.

## FIGURE LEGENDS

**Figure 3.1.** Growth defect in *Mfn2* mutant mice. (A) Mating scheme. *Slc6a3-Cre* is controlled by the dopamine transporter locus and expressed in a subset of dopaminergic neurons, particularly the SNC, VTA, and retrorubral field (RRF) (Bäckman, Malik et al. 2006). (B) Representative image of a 22 week old *Mfn2* mutant (*Mfn2*-/-) compared to a heterozygous littermate (*Mfn2*+/-). Note the small size and severe kyphosis of the *Mfn2* mutant. (C) Plot showing weekly weight measurements. Each point represents the average weight  $\pm$  SEM (n = 10-15 for each genotype and sex). Both male and female *Mfn2* mutants are significantly smaller (p < 0.05, two-tailed Student *t*-test) than control animals by 5 weeks of age.

**Figure 3.2.** Longitudinal analysis of locomotive activity in *Mfn2* mutants. (A) Representative traces from open field analysis. The traces represent spontaneous movement in an open field during a 15-minute observation period. The genotypes and ages of the mice are indicated. The black square indicates the starting position of the mice. The open field analysis was quantified to obtain the (B) distance traversed, (C) average velocity, (D) rearing frequency, and (E) immobile periods between activity. In all graphs, values from the heterozygous and homozygous animals were normalized to that of the wild-type controls, and error bars represent propagated standard error. The Student *t*-test was used to obtain p-values between *Mfn2* mutants and wild-type controls (\* p < 0.05; \*\* p < 0.001; n = 6-10 animals per age and genotype).

**Figure 3.3.** Retrograde degeneration of SNC dopaminergic neurons. (A) Dopaminergic projections to the striatum (Str), nucleus accumbens (NAc), and olfactory tubercle (OT). The diagram delineates these regions. Sections were stained with TH antibody to label dopaminergic projections (brown pigment). At 3 weeks of age, *Mfn2* mutant animals show decreased TH-immunoreactive terminals in the dorsolateral striatum (outlined region). Later time points reveal widespread loss in the striatum. VTA projections to the Ac and OT are still present, albeit reduced, at 11 and 14 wks (outlined regions in bottom 2 panels). (B) Dopaminergic neurons at the SNC and VTA. Sections of the midbrain were stained with TH and counterstained with Cresyl violet (blue) to identify dopaminergic neurons. At 11 and 14 weeks, the *Mfn2* mutants exhibit reduced staining in the SNC, whereas the VTA is relatively preserved. The SNC and VTA regions are outlined. (C) Quantification of TH-staining. Measured values of TH-positive signal from heterozygous and homozygous animals were normalized to wild-type controls. For each animal, 3 sections were measured. The Student *t*-test was used to obtain p-values (\* p < 0.05; \*\* p < 0.001; n = 3-6) and error bars represent propagated error. (D) Quantitation of dopaminergic cell loss in the SNC. Counts from heterozygous and homozygous animals were normalized to wild-type controls (n = 3 for ages and genotype). For each animal, 9 sections spanning the rostro-caudal extent of the midbrain were manually counted. Statistical analysis was performed as in (C). (E) Magnified images of (B) showing loss of dopaminergic neurons and processes in *Mfn2* mutant.

**Figure 3.4.** Mitochondrial fragmentation and depletion in slice cultures of *Mfn2* mutants. Cre-mediated expression of mito-Dendra2 labels dopaminergic neurons. (A) Slice cultures

of heterozygous controls and *Mfn2* mutants. Slices were immunostained with TH (red). The first column shows a merged image of TH and mito-Dendra2 fluorescence (green) while the last column is an enlargement of the boxed zone. The asterisks highlight degenerating *Mfn2*-null neurons that have diminished or absent TH staining. (B) Mito-Dendra2 signal in neuronal projections. Marked depletion of mitochondria in both proximal and distal processes is evident in *Mfn2* mutant slices. (C) Quantification of mitochondrial mass normalized to the number of dopaminergic neurons. For each sample, the total mito-Dendra2-positive area in a 5 mm x 5 mm region was measured and normalized to the number of Dendra2-positive neurons. Mitochondrial mass is reported as percentage area of heterozygous control ± SEM. The Student *t*-test was used to evaluate statistical significance (\* p < 0.001; n = 5 for mutant slices; n = 7 for control). Scale bar is 10 µm for all images.

**Figure 3.5.** Decreased mitochondrial transport in *Mfn2* mutant cultures. (A) A representative tracking experiment of an *Mfn2* heterozygous control. A subset of mitochondria in the nerve process was photoconverted to red for time-lapse imaging. The image collection from the photoconverted signal was processed into a kymograph to visualize mitochondrial movement (binary image). Velocity measurements were calculated from the red tracks that overlay mitochondrial trajectories. (B) Representative tracking experiment in an *Mfn2* mutant showing loss of mitochondrial transport. (C) Quantification of mitochondrial transport in neuronal processes. For each region of photoconversion, a positive event was defined as directed movement of more than 5 µm during the 15 minute imaging session. The graph shows the frequency of photoconversion experiments that resulted in at least one positive event. For *Mfn2* heterozygous slices, 150 regions were

scored; for *Mfn2* mutant slices, 138 regions were scored. The Student *t*-test was used to calculate statistical significance (\*\* p < 0.001 ). (D) A scatter plot of the average velocity of moving mitochondria. The red dots indicate the population averages ± SD. Statistical significance was calculated as in (C) (n = 138 mitochondria in heterozygous slices, n = 38 mitochondria in mutant slices). Scale bar is 5 μm for all images.

**Figure 3.6.** Analysis of *Mfn1*-null mice. Representative images of TH-immunoreactivity in (A) striatum and (B) midbrain at 22 weeks of age. No loss of TH signal is evident in the striatum or the SNc. Open field summary of (C) total distance, (D) average velocity, (E) rearing frequency and (F) immobile duration. Results of heterozygous and homozygous *Mfn1* mutants were normalized to wild-type controls. Error bars represent propagated standard error.

**Figure 3.7.** Comparison of *Mfn*-double mutants with *Mfn2* mutants in the open field test. (A) Total distance traveled during a 15-minute period of observation. (B) Average velocity exhibited by animals. (C) Rearing frequency. (D) Average duration of immobility between bouts of activity. In all calculations, values were normalized to wild-type controls and error bars indicate the propagation of standard error. The Student *t*-test was used to calculate statistical significance (n=3-9 animals). \* p < 0.05; \*\* p < 0.01; \*\*\* p < 0.001.

Figure 3.1

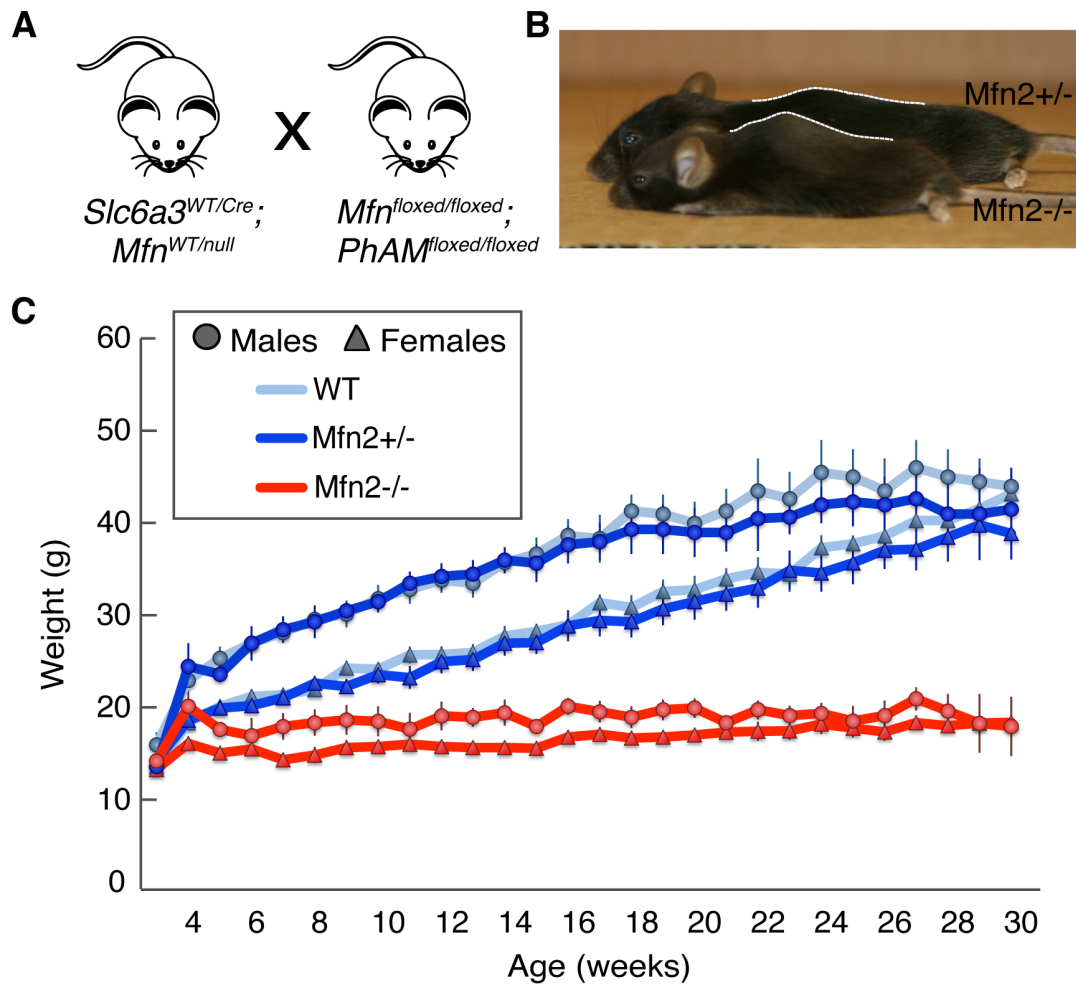


Figure 3.2

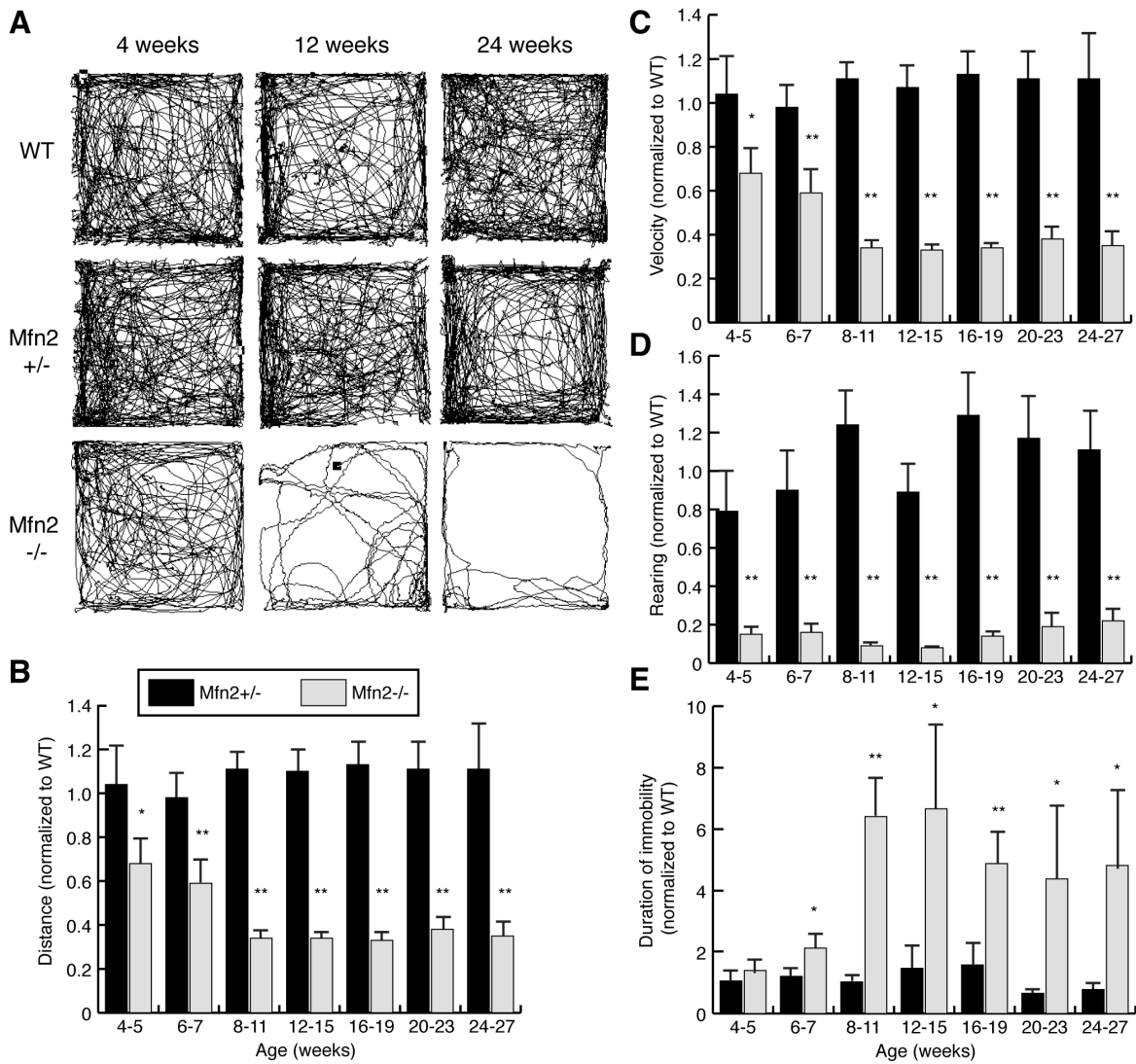


Figure 3.3

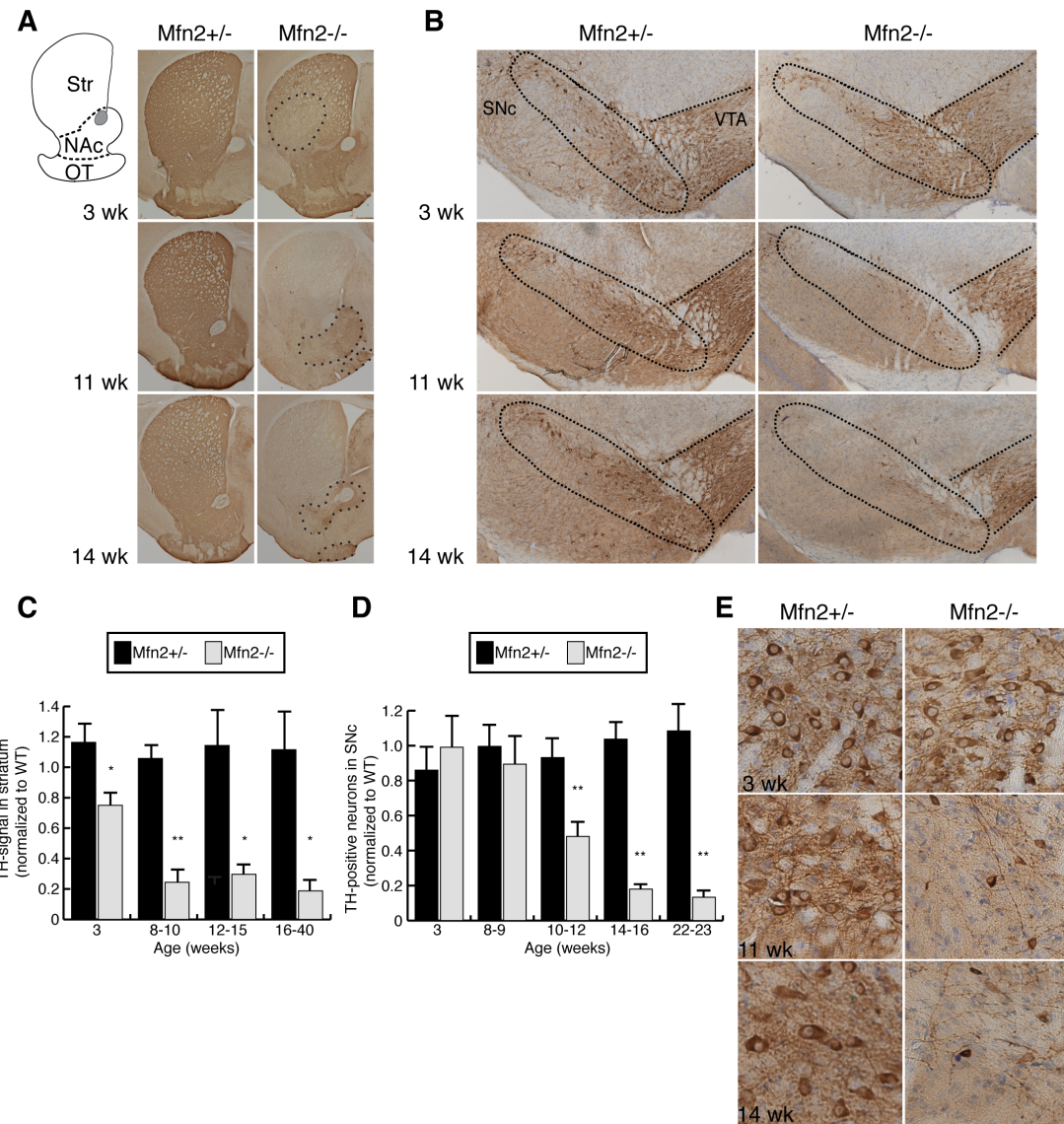


Figure 3.4

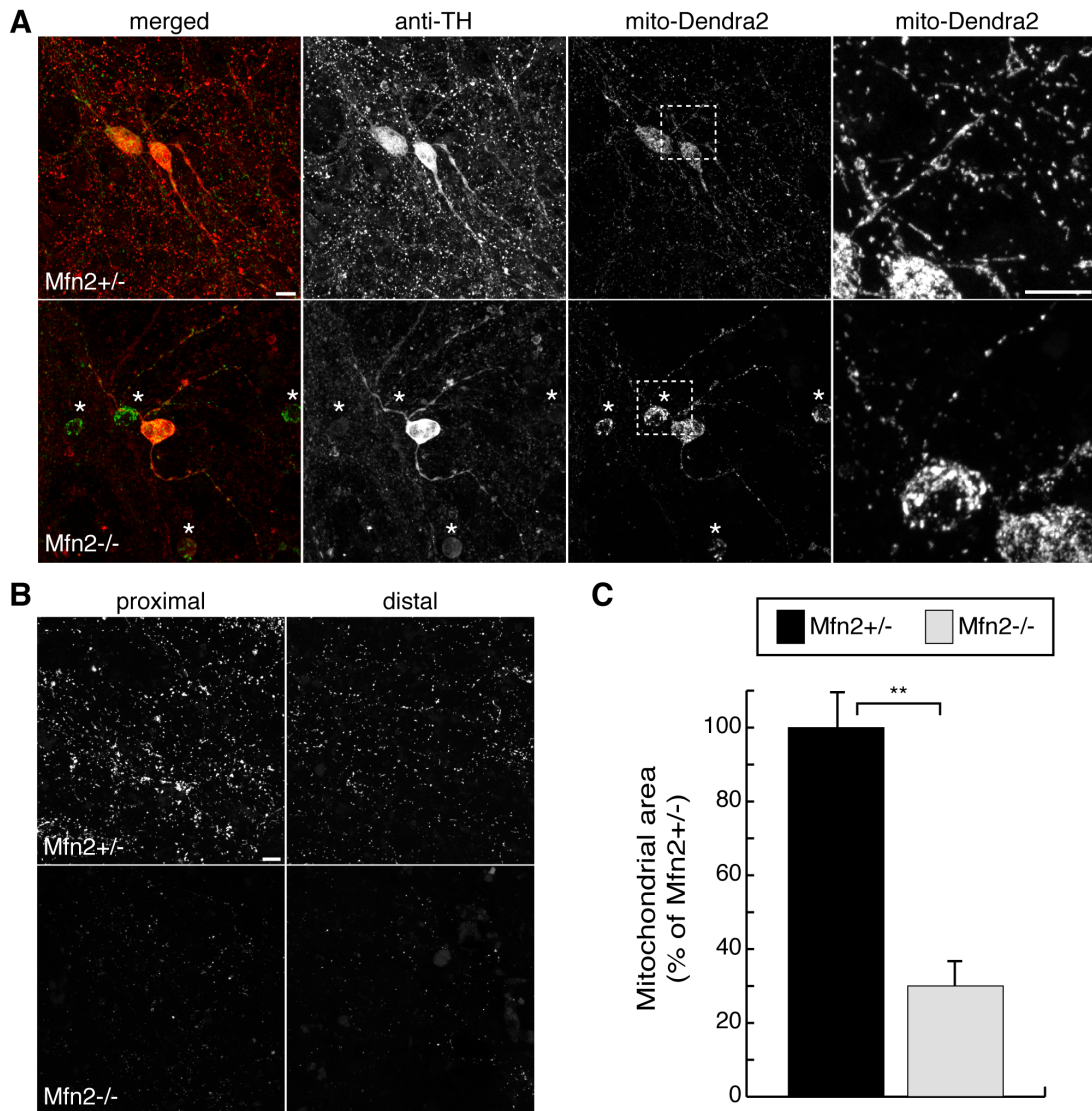


Figure 3.5

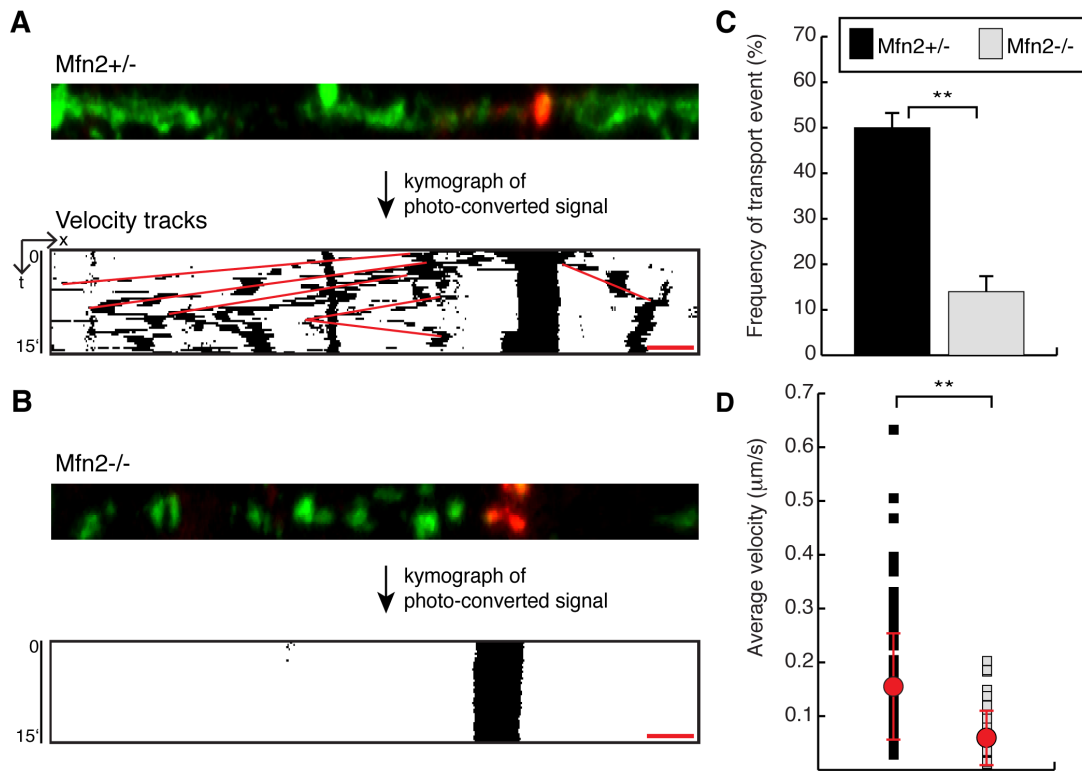


Figure 3.6

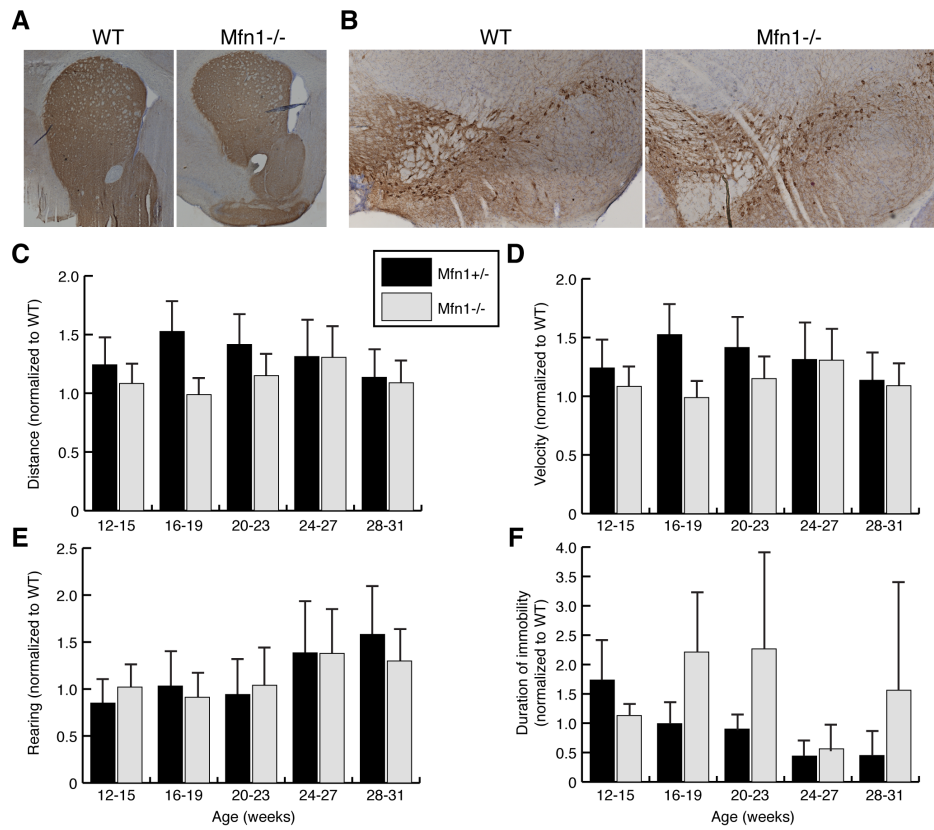
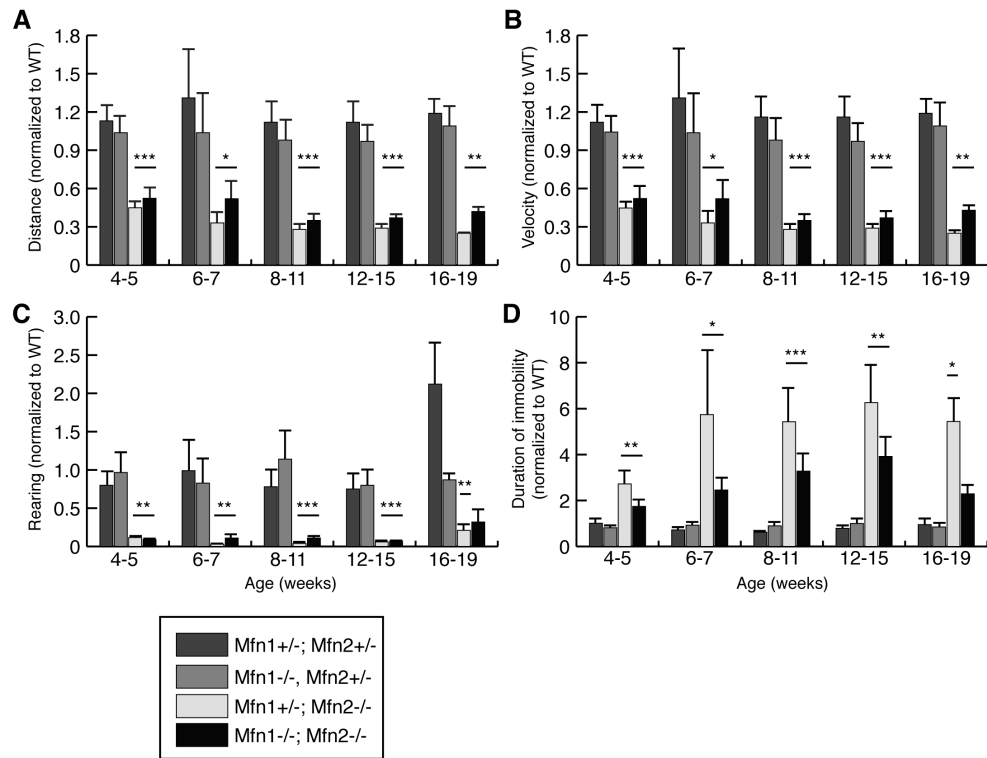


Figure 3.7



## REFERENCES

- Ammari, R., C. Lopez, et al. (2009). A mouse juvenile or adult slice with preserved functional nigro-striatal dopaminergic neurons. Neuroscience **159**(1): 3-6.
- Bäckman, C. M., N. Malik, et al. (2006). Characterization of a mouse strain expressing Cre recombinase from the 3' untranslated region of the dopamine transporter locus. Genesis **44**(8): 383-390.
- Beurrier, C., Y. Ben-Ari, et al. (2006). Preservation of the direct and indirect pathways in an in vitro preparation of the mouse basal ganglia. Neuroscience **140**(1): 77-86.
- Cannon, J. R. and J. T. Greenamyre (2010). Neurotoxic in vivo models of Parkinson's disease recent advances. Prog Brain Res **184**: 17-33.
- Chen, H. and D. C. Chan (2009). Mitochondrial dynamics--fusion, fission, movement, and mitophagy--in neurodegenerative diseases. Hum Mol Genet **18**(R2): R169-176.
- Chen, H., S. A. Detmer, et al. (2003). Mitofusins Mfn1 and Mfn2 coordinately regulate mitochondrial fusion and are essential for embryonic development. J Cell Biol **160**(2): 189-200.
- Chen, H., J. M. McCaffery, et al. (2007). Mitochondrial fusion protects against neurodegeneration in the cerebellum. Cell **130**(3): 548-562.
- Cheng, H. C., C. M. Ulane, et al. (2010). Clinical progression in Parkinson disease and the neurobiology of axons. Ann Neurol **67**(6): 715-725.
- Chesselet, M. F. and F. Richter (2011). Modelling of Parkinson's disease in mice. Lancet Neurol **10**(12): 1108-1118.

- Cho, S., A. Wood, et al. (2007). Brain slices as models for neurodegenerative disease and screening platforms to identify novel therapeutics. Curr Neuropharmacol **5**(1): 19-33.
- Clark, I. E., M. W. Dodson, et al. (2006). Drosophila pink1 is required for mitochondrial function and interacts genetically with parkin. Nature **441**(7097): 1162-1166.
- Damier, P., E. C. Hirsch, et al. (1999). The substantia nigra of the human brain. II. Patterns of loss of dopamine-containing neurons in Parkinson's disease. Brain **122** ( Pt 8): 1437-1448.
- Dawson, T. M., H. S. Ko, et al. (2010). Genetic animal models of Parkinson's disease. Neuron **66**(5): 646-661.
- Deng, H., M. W. Dodson, et al. (2008). The Parkinson's disease genes pink1 and parkin promote mitochondrial fission and/or inhibit fusion in Drosophila. Proc Natl Acad Sci USA **105**(38): 14503-14508.
- Detmer, S. A. and D. C. Chan (2007). Functions and dysfunctions of mitochondrial dynamics. Nat Rev Mol Cell Biol **8**(11): 870-879.
- Gahwiler, B. H., M. Capogna, et al. (1997). Organotypic slice cultures: a technique has come of age. Trends Neurosci **20**(10): 471-477.
- Greene, J. C., A. J. Whitworth, et al. (2003). Mitochondrial pathology and apoptotic muscle degeneration in Drosophila parkin mutants. Proc Natl Acad Sci USA **100**(7): 4078-4083.
- Gunapala, K. M., D. Chang, et al. (2010). Striatal pathology underlies prion infection-mediated hyperactivity in mice. Prion **4**(4): 302-315.

- Hirsch, E., A. M. Graybiel, et al. (1988). Melanized dopaminergic neurons are differentially susceptible to degeneration in Parkinson's disease. Nature **334**(6180): 345-348.
- Hornykiewicz, O. (1998). Biochemical aspects of Parkinson's disease. Neurology **51**(2 Suppl 2): S2-9.
- Irrcher, I., H. Aleyasin, et al. (2010). Loss of the Parkinson's disease-linked gene DJ-1 perturbs mitochondrial dynamics. Hum Mol Genet **19**(19): 3734-3746.
- Kang, J. S., J. H. Tian, et al. (2008). Docking of axonal mitochondria by syntaphilin controls their mobility and affects short-term facilitation. Cell **132**(1): 137-148.
- Kearns, S. M., B. Scheffler, et al. (2006). A method for a more complete in vitro Parkinson's model: slice culture bioassay for modeling maintenance and repair of the nigrostriatal circuit. J Neurosci Methods **157**(1): 1-9.
- Kish, S. J., K. Shannak, et al. (1988). Uneven pattern of dopamine loss in the striatum of patients with idiopathic Parkinson's disease. Pathophysiologic and clinical implications. N Engl J Med **318**(14): 876-880.
- Krebiehl, G., S. Ruckerbauer, et al. (2010). Reduced basal autophagy and impaired mitochondrial dynamics due to loss of Parkinson's disease-associated protein DJ-1. PLoS One **5**(2): e9367.
- Langston, J. W., P. Ballard, et al. (1983). Chronic Parkinsonism in humans due to a product of meperidine-analog synthesis. Science **219**(4587): 979-980.
- Misgeld, T., M. Kerschensteiner, et al. (2007). Imaging axonal transport of mitochondria in vivo. Nat Meth **4**: 559-561.

- Misko, A., S. Jiang, et al. (2010). Mitofusin 2 is necessary for transport of axonal mitochondria and interacts with the Miro/Milton complex. *J Neurosci* **30**(12): 4232-4240.
- Palmiter, R. D. (2008). Dopamine signaling in the dorsal striatum is essential for motivated behaviors: lessons from dopamine-deficient mice. *Ann N Y Acad Sci* **1129**: 35-46.
- Park, J., S. B. Lee, et al. (2006). Mitochondrial dysfunction in Drosophila PINK1 mutants is complemented by parkin. *Nature* **441**(7097): 1157-1161.
- Parker, W. D., Jr. and R. H. Swerdlow (1998). Mitochondrial dysfunction in idiopathic Parkinson disease. *Am J Hum Genet* **62**(4): 758-762.
- Pham, A. H., J. M. McCaffery, et al. (2012). Mouse lines with photo-activatable mitochondria to study mitochondrial dynamics. *Genesis*.
- Pifl, C., G. Schingnitz, et al. (1991). Effect of 1-methyl-4-phenyl-1,2,3,6-tetrahydropyridine on the regional distribution of brain monoamines in the rhesus monkey. *Neuroscience* **44**(3): 591-605.
- Poole, A. C., R. E. Thomas, et al. (2008). The PINK1/Parkin pathway regulates mitochondrial morphology. *Proc Natl Acad Sci USA* **105**(5): 1638-1643.
- Schapira, A. H., J. M. Cooper, et al. (1989). Mitochondrial complex I deficiency in Parkinson's disease. *Lancet* **1**(8649): 1269.
- Sheng, Z. H. and Q. Cai (2012). Mitochondrial transport in neurons: impact on synaptic homeostasis and neurodegeneration. *Nat Rev Neurosci* **13**(2): 77-93.
- Stoessl, A. J. (2011). Neuroimaging in Parkinson's disease. *Neurotherapeutics* **8**(1): 72-81.
- Stoppini, L., P. A. Buchs, et al. (1991). A simple method for organotypic cultures of nervous tissue. *J Neurosci Methods* **37**(2): 173-182.

- Tanaka, A., M. M. Cleland, et al. (2010). Proteasome and p97 mediate mitophagy and degradation of mitofusins induced by Parkin. J Cell Biol **191**(7): 1367-1380.
- Thomas, K. J., M. K. McCoy, et al. (2011). DJ-1 acts in parallel to the PINK1/parkin pathway to control mitochondrial function and autophagy. Hum Mol Genet **20**(1): 40-50.
- Twig, G., A. Elorza, et al. (2008). Fission and selective fusion govern mitochondrial segregation and elimination by autophagy. EMBO J **27**(2): 433-446.
- Wang, X., T. G. Petrie, et al. (2012). Parkinson's disease-associated DJ-1 mutations impair mitochondrial dynamics and cause mitochondrial dysfunction. J Neurochem.
- Wang, X., M. H. Yan, et al. (2012). LRRK2 regulates mitochondrial dynamics and function through direct interaction with DLP1. Hum Mol Genet.
- Yang, Y., S. Gehrke, et al. (2006). Mitochondrial pathology and muscle and dopaminergic neuron degeneration caused by inactivation of Drosophila Pink1 is rescued by Parkin. Proc Natl Acad Sci USA **103**(28): 10793-10798.
- Yang, Y., Y. Ouyang, et al. (2008). Pink1 regulates mitochondrial dynamics through interaction with the fission/fusion machinery. Proc Natl Acad Sci USA **105**(19): 7070-7075.
- Zhou, Q. Y. and R. D. Palmiter (1995). Dopamine-deficient mice are severely hypoactive, adipsic, and aphagic. Cell **83**(7): 1197-1209.

*C h a p t e r 4*

## MONITORING MITOCHONDRIAL DYNAMICS IN SKELETAL MUSCLE

Anh H. Pham<sup>1</sup>, Prashant Mishra<sup>1</sup>, and David C. Chan<sup>1,2</sup>

<sup>1</sup>From the Division of Biology

<sup>2</sup>Howard Hughes Medical Institute

California Institute of Technology

Pasadena, CA 91125

## INTRODUCTION

Live-imaging analysis of mitochondria in different cell types demonstrate that mitochondria are dynamic organelles that continually remodel its size and shape and actively redistribute throughout the cells. However, in ultrastructural images of skeletal muscles, mitochondria appear as doublets rigidly organized along the electrodense Z-discs (Ogata and Yamasaki 1997). Multiple reports have suggested an important role for mitochondrial dynamics in muscle function and development (Bo, Zhang et al. 2010; Chen, Vermulst et al. 2010; Zorzano, Hernandez-Alvarez et al. 2010). In particular, decreased expression of *Mfn2* has been detected in skeletal muscles of obese and diabetic patients and obese rodent models (Bach, Pich et al. 2003; Bach, Naon et al. 2005). These studies suggest that mitochondrial dynamics may be critical regulators of muscle function. However, assessment of mitochondria in live skeletal muscles has been precluded by the lack of tools available for imaging mitochondria in tissues. By using the mouse lines we have previously developed with photoactivatable mitochondria (PhAM), we explore and characterize the dynamic properties of mitochondria.

Muscles are composed of multinucleated myofibers that extend the length of the muscle. Myofibers compose single cell units in muscle tissue. Postnatal development of skeletal muscles is a dynamic period that involves rapid changes in myofiber size and architecture of organellar networks. Between the postnatal ages of 7 and 21 days, the fast twitch extensor digitorum longus (EDL) muscle undergoes significant hypertrophy, characterized by the expansion of myofiber cross-section and accumulation of myonuclei attributed to fusion of satellite cells (White, Biérinx et al. 2010). Maturation of the triad connections between the sarcoplasmic reticulum, mitochondria, and the transverse T-

tubules also occur during this stage (Boncompagni, Rossi et al. 2009). A past study from our lab has shown that mitochondrial fusion plays an important role for the development of fast twitch muscles and the maintenance of mitochondrial DNA integrity (Chen, Vermulst et al. 2010). In support of these findings, we demonstrated in chapter 2 that mitochondrial network undergoes dramatic rearrangement during postnatal development of the extensor digitorum longus (EDL) muscle, a fast twitch muscle. Developing muscles exhibited tubular interconnected mitochondria oriented along the long axis of the myofiber. In adult EDL muscles, mitochondria rearrange as fragmented doublets aligned at the Z-discs. The tubular morphology of mitochondria in young muscles suggests that rates of mitochondrial fusion may be occurring more frequently in developing muscles. In this chapter, we take advantage of the photoswitchable properties of Dendra2 in the PhAM mouse lines to quantify mitochondrial fusion during muscle development.

Muscle fibers are classified by its contractile, metabolic, and molecular properties. Fast twitch muscle fibers exhibit higher contraction and faster fatigue rates relative to slow twitch fibers. Furthermore, fast twitch fibers are more reliant on glycolysis for ATP synthesis while slow twitch fibers mainly utilize aerobic respiration to generate fuel. The compositions of the myosin heavy chains, part of the contractile units in muscles, also differ between fiber types (Schiaffino, Gorza et al. 1989; Schiaffino and Reggiani 1994). Recent reports support the existence of fiber-type specialization of mitochondrial function (Leary, Lyons et al. 2003; Picard, Hepple et al. 2012).

Although the multinucleated organization of myofibers suggests that individual muscle cells act as a syncytium, there are numerous evidences to suggest that myofibers are

compartmentalized. Serial sections of different rodent muscles demonstrate isolated segments of atrophy within the fiber that correlated with age (Cao, Wanagat et al. 2001; Wanagat, Cao et al. 2001; Bua, McKiernan et al. 2002). These segments of sarcopenia, loss of muscle mass with aging, exhibited diminishment of mitochondrial-encoded enzymes involved in the electron transport system and an accumulation of deleted fragments of mitochondrial DNA (mtDNA) (Cao, Wanagat et al. 2001; Wanagat, Cao et al. 2001; Bua, McKiernan et al. 2002). Interestingly, the positional correlation between fiber atrophy and mitochondrial defects suggests a causal link between mtDNA deletions and sarcopenia (Herbst, Pak et al. 2007; Hiona and Leeuwenburgh 2008). Similar serial analysis in aging muscles from humans also shows detrimental accumulation of mtDNA deletions in fiber segments with defects in the electron transport system (Bua, Johnson et al. 2006). These pathological findings suggest that myofibers may have functionally independent compartments wherein a damaged region can be isolated from the remaining healthy parts of the fiber. Nonetheless, the segmentation of myofibers has never been directly visualized under nonpathological states.

Muscle fibers are complex tissues that exhibit dynamic changes in structural and organelle compositions during various stages, including development, adaptation, and aging. Multiple lines of evidence suggest that mitochondrial properties may also fluctuate in response to these transitions. In this chapter, we apply the *PhAM* mouse models to assess mitochondrial morphology and metabolic properties during development. We also compare mitochondrial profiles across fiber types. To explore the compartmentalization of myofibers, we describe a novel system that enables quantification and comparison of muscle segments in different fiber types.

## RESULTS

### Developing fast twitch muscles exhibit higher rates of mitochondrial fusion

In chapter 2, we previously showed that young EDL muscles exhibited more tubular mitochondria oriented along the long axis of the myofiber. To determine whether these elongated mitochondria result from higher fusion or decreased fission rates, we directly quantified mitochondrial fusion. We utilized the *PhAM<sup>excised</sup>* line which expresses mito-Dendra2 ubiquitously to assess mitochondrial morphology and dynamics in the EDL muscle. The photoswitchable properties of mito-Dendra2 enable quantification of mitochondrial fusion based on the dilution of the photoconverted signal. A subset of mitochondria in the myofiber has been photoswitched to red fluorescence and the red signal is monitored over time (Figure 4.1). A positive fusion event is characterized by an increase in the area of photoconverted signal and a corresponding decrease in the intensity of the original mitochondrion. In a young EDL myofiber, several mitochondrial fusion events are indicated while a representative adult EDL myofiber shows minimal changes in the area or intensity of the red signal (Fig 4.1 A and B). To quantify the frequency of myofibers with fusing mitochondria, we determined the number of myofibers that exhibited a statistically significant change in the intensity of photoconverted signal by the end of the timelapse. We noted that fusion events were detected in 43% of myofibers at postnatal ages between 9 and 13 days (Fig 4.1C). The frequency of mitochondrial fusion events decreases as the muscle develops into adulthood. By 4 months old, only 18% of myofibers exhibited mitochondrial fusion within the observation period.

### Mitochondrial profile is fiber-type dependent

From chapter 2, we noted that mitochondrial network rearranges from tubular to fragmented doublets during the development of the EDL muscle. We decided to extend the analysis toward oxidative type I fibers such as the soleus. Interestingly, oxidative myofibers retained tubular mitochondrial network along the long axis of the fiber (figure 4.2 C and D). Consistent with published reports, there is a striking difference in mitochondrial mass, with the soleus exhibiting higher mitochondrial content (Picard, Hepple et al. 2012). In contrast, mitochondrial network in the EDL appear more scarce and oriented along the transverse axis of the myofiber (figure 4.2 A and B). To determine whether there are differences in mitochondrial function between these fibers, we utilized a mitochondrial dye called TMRM that is readily taken up by metabolically active mitochondria. We observed that mitochondria in the soleus exhibited intense uniform TMRM signal, which is consistent with a higher metabolic status for oxidative fibers (figure 4.3 E-H). In the EDL, the TMRM staining is more heterogeneous (figure 4.3A). Myofibers that have elongated mitochondria and high mitochondrial density show greater uptake of the dye whereas the myofibers with sparse and punctate mitochondria exhibit less TMRM intensity (figure 4.3 B-D).

### A tool for measuring mitochondrial domains in myofibers

To assess whether myofibers have distinct functional domain of mitochondria, we designed a mosaic fluorescent reporter system for visualizing mitochondria in myofibers. Previously, we generated a *PhAM*<sup>flaxed</sup> line that relies on Cre recombinase for expression of mito-Dendra2. To create a system wherein Cre recombinase is sparsely expressed in the myofiber, we took advantage of the developmental transitions during postnatal growth of

muscle. During the first three weeks of postnatal development, myofibers undergo significant hypertrophy, which is characterized by an increase in the size and number of myonuclei per myofiber (White, Biérinx et al. 2010). Myofiber hypertrophy is attributed to the differentiation of satellite cells, the muscle stem cells, into myoblasts and the subsequent incorporation of myoblasts into the myofiber (Seale and Rudnicki 2000; Seale, Sabourin et al. 2000; Zammit, Relaix et al. 2006). Since the regions where myoblast-derived satellite cells fuse with myofibers occur at random, a Cre driver expressed in satellite cells provides a way to achieve sparse distribution of Cre-positive myonuclei. We selected the *Pax7-CreER* driver (Lepper and Fan 2010) because Pax7 expression is restricted to satellite cells and the tamoxifen inducible Cre provides further tunable induction of Cre.

In a preliminary study, we crossed the *Pax7-CreER* line with the *PhAM*<sup>flaxed/flaxed</sup> line and analyzed young EDL muscle from the pups. Consistent with a previous study which reported some leaky activity of CreER in the absence of tamoxifen induction (Nishijo, Hosoyama et al. 2009), we observed excision of the floxed terminal signal and expression of mito-Dendra2 in the myofibers (figure 4.4A). In this system, the leakiness of CreER activity provided stochastic and mosaic expression of mito-Dendra2 that is conducive for assessing the mitochondrial domain along the myofiber. In live-imaging analysis, we used TMRM as a counterstain for identifying healthy and metabolically active myofibers. When mito-Dendra2 signal is measured along the longitudinal axis of the myofiber, the fluorescence is distributed as individual peaks demonstrating that the myonuclear compartment is discrete (figure 4.4 B and C). Furthermore, the multimodal

distribution of mito-Dendra2 also suggests that the mitochondrial network may be compartmentalized along the myofiber.

Since our previous observations showed a drastic difference in mitochondrial profiles across fiber types, we applied a similar analysis to examine the soleus muscle. In contrast to the EDL, discrete mito-Dendra2 peaks were difficult to identify (compare figure 4.5 A and B). By plotting the intensity of mito-Dendra2 along the horizontal axis of the myofiber, it is evident that the peak widths of the soleus myofibers are broader (compare figure 4.5 C-F). The expansive activation of mito-Dendra2 may make it difficult to measure the muscle compartmentalization in the soleus. Nonetheless, the diffuseness of the mitochondrial domain in the soleus is striking and may be attributed to any of the following scenarios. In the first scenario, more incorporation of myoblast-derived satellite cells along the myofiber may result in higher numbers of Cre positive myonuclei. A second possibility could be that the myonuclear compartment is larger in oxidative fibers. And lastly, frequent rates of mitochondrial fusion and exchange of matrix content may increase the spread of the mito-Dendra2 signal. Future studies aimed at elucidating the mechanisms underlying our observations may yield insights into how mitochondrial networks may determine or affect the physiology of different fiber types.

## DISCUSSION

Mitochondrial dynamics play important roles for the health and maintenance of muscle tissues. However, few studies have explored the dynamics of mitochondria in the complexities of muscle development or different fiber types. In this chapter, we applied the *PhAM* mouse lines to elucidate mitochondrial properties in muscle tissues. We showed that mitochondrial fusion decreases with maturation of myofibers, but this phenomena is fiber-type dependent. Oxidative muscles such as the soleus retain the elongated and interconnected mitochondrial network into adulthood, whereas the fast-twitch EDL muscle switch to fragmented doublets with maturation. Using TMRM staining as a measure of mitochondrial metabolism, we observed that myofibers with elongated mitochondria exhibited greater retention and uptake of TMRM irrespective of the fiber type. In the EDL, TMRM intensity was heterogeneous with myofibers having predominantly tubular mitochondria showing higher TMRM signal. Although the EDL muscle is considered fast twitch containing mostly glycolytic components, 4% of myofibers in the EDL are oxidative in origin (Agbulut, Noirez et al. 2003). It is unclear whether the fibers with higher TMRM intensity belong to the oxidative type. Since the tools for classifying myofibers in live tissues are limiting, future studies are needed to clarify the link between mitochondrial morphology and mitochondrial membrane potential. Nonetheless, several studies have observed the correlation between loss of mitochondrial fusion and diminished membrane potential (Chen, Detmer et al. 2003; Olichon, Baricault et al. 2003). Consistent with the previous reports, we found that myofibers with fragmented mitochondria exhibited dimmer TMRM in the EDL muscle.

To assess whether the multi-nucleated organization of myofibers behave as a syncytium or discrete compartments, we have designed a powerful platform for visualizing the mitochondrial domain contributed by individual myonuclei. We achieved a low stochastic distribution of Cre positive myonuclei using *Pax7-CreER* to track sites of myoblast fusion into the myofiber. The leaky activity of CreER afforded minimally mosaic expression of mito-Dendra2 to track the mitochondrial domain in the myofiber. Our analysis demonstrated that glycolytic muscles such as the EDL exhibit more segmentation compared to the oxidative soleus muscle. The mito-Dendra2 fluorescence in the EDL was easily resolved into single or multimodal peaks whereas the soleus muscle showed diffuse distribution of mito-Dendra2 signal. Interestingly, studies have observed that fast twitch glycolytic muscle undergo greater susceptibility to segmental sarcopenia and mitochondrial defects (Wanagat, Cao et al. 2001; Bua, McKiernan et al. 2002). Taken together, our findings are consistent with a model wherein glycolytic muscles have discrete compartments that may be apt for containing and segregating defects along the myofiber. Future studies will need to explore how the expansive compartments in oxidative fibers are protective for sarcopenia. Our characterization of tubular mitochondria in the soleus muscle suggests that the larger compartment may result in greater complementation of defects, and thereby may confer protection against metabolic defects and sarcopenia. Our characterization of mitochondrial dynamics in skeletal muscles may lead to a better understanding of mechanisms underlying myopathies.

## MATERIALS AND METHODS

**Mouse colonies and mating.** Generation of the PhAM mouse lines has been described (Anh, Michael et al. 2012). The *Pax7CreER* driver was obtained from the Jackson Laboratory (B6;129-*Pax7tm2.1(cre/ERT2)Fan/J*). All experiments were approved by the Caltech Institute Animal Care and Use Committee.

**Muscle preparation.** Animals were euthanized by halothane. Whole EDL or soleus muscles were dissected and rinsed in Tyrodes salt solution (Sigma T2145) containing with 1 g/L of bicarbonate and 25 mM HEPES and pH to 7.4. For mitochondrial fusion measurements, muscles were imaged in DMEM (Gibco, 21063-029) supplemented with 1 mM sodium pyruvate (Gibco), 10% heat-inactivated horse serum, and 1X of penicillin-streptomycin (Gibco). For TMRM staining, muscles were transferred to DMEM (Sigma, D5030) supplemented with 2 mM of sodium pyruvate, 5 mM of D-glucose, 10% dialyzed horse serum, 1X penicillin-streptomycin, 25 mM HEPES, and pH to 7.4. Muscles were incubated with 200 nM of TMRM for 3 hrs at 37°C prior to live imaging.

**Imaging analysis.** Images were acquired on a Zeiss LSM 710 confocal microscope using Plan-Apochromat 63X/1.4 oil or Plan-Apochromat 20X/0.8 objectives. Z-stack acquisitions oversampled twice the thickness of the optical slice. To photoconvert Dendra2, a small region was irradiated with the 405 nm laser (4% laser power) for 90 iterations at a scan speed of 6.3–12.61 μs/pixel. For live imaging, muscle samples were placed in a coverglass bottom dish, stabilized with a slice anchor (Warner Instruments), and imaged on a stage-top heated platform maintained at 35°C. To measure mitochondrial

fusion, one region per myofiber was photoswitched and recorded for 20 minutes at 1 min intervals. Myofibers were recorded over a Z-depth of 4  $\mu\text{m}$ , and 4-5 regions of the tissue would be imaged during the experiment. Custom scripts were written in Matlab by Dr. Prashant Mishra to analyze the voxel intensity over time and to apply the two-sample Kolmogorov-Smirnov test for statistical comparison. A fusion event is scored when there is statistically significant differences between the voxel intensities at the beginning and the end of the time lapse. To avoid drifting artifacts that may change voxel intensities, the last 3-5 frames of the time lapse must be statistically significant for a fusion event to be scored.

The ImageJ software was used to generate line analysis of mitochondrial compartments in myofibers. Briefly, myofibers were straightened and the *Plot* algorithm measured intensity values along a drawn line of 200  $\mu\text{m}$  thickness.

## FIGURE LEGENDS

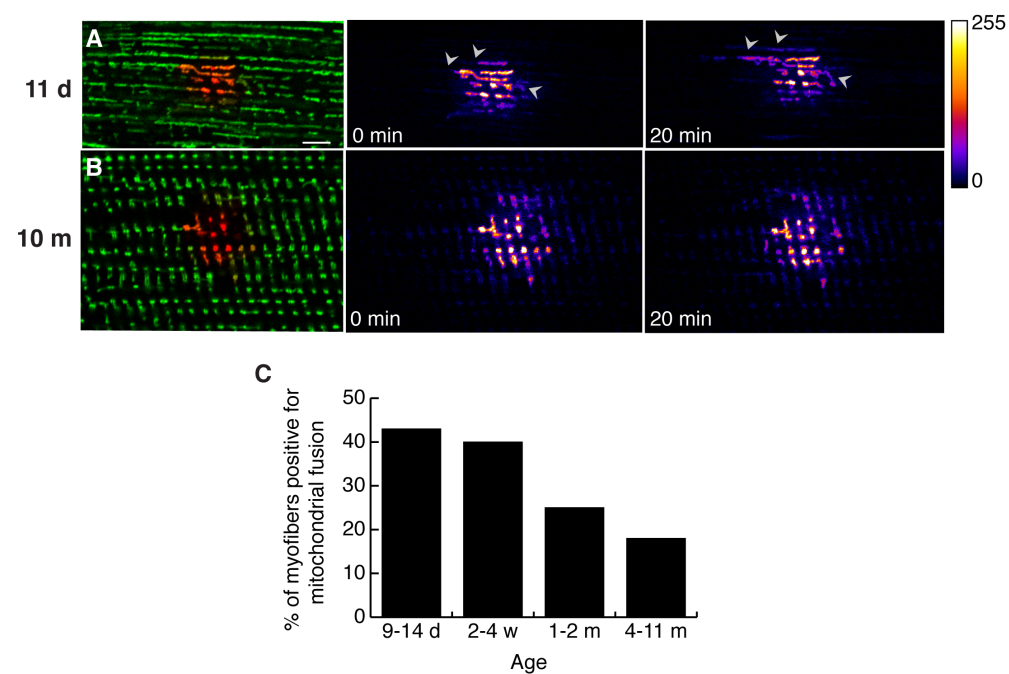
**Figure 4.1. Mitochondrial fusion declines with age in EDL.** Mitochondrial fusion was monitored over a duration of 20 minutes in EDL muscles at indicated ages. (A) Representative images of a young myofiber wherein a subset of mitochondria was photoswitched (colored red) and tracked. The heat map shows the photoconverted signal at the beginning and the end of the time lapse. The heat intensity values are indicated by the gradient. Mitochondrial fusion results in a spread of the photoconverted signal and a concurrent decrease in intensity (denoted by arrowheads). Scale bar is 5  $\mu\text{m}$ . (B) Representative images of adult EDL. (C) Quantification of myofibers that exhibits fusogenic mitochondria at various ages. A positive fusion event is scored when there is a statistically significant change ( $p < 0.05$ ) in the intensity of the photoconverted signal by the end of the recording.  $n = 24\text{-}56$  myofibers for each age group.

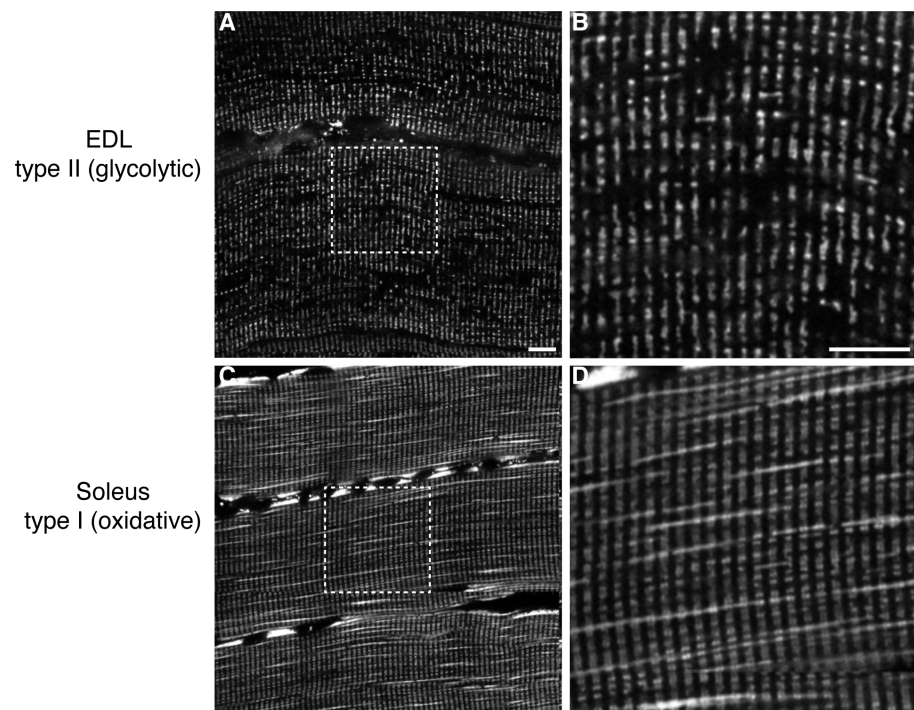
**Figure 4.2. Mitochondrial morphology is dependent on muscle type.** Mitochondrial profile in adult EDL (A and B) and soleus (C and D) muscles at 3.5 months of age. Last column shows magnified images of the boxed regions. Scale bar 10  $\mu\text{m}$ .

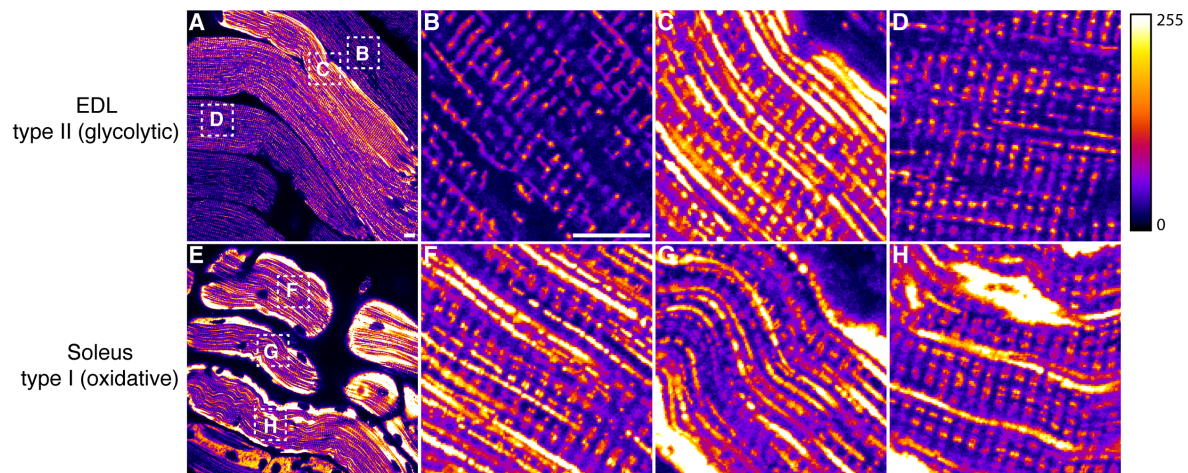
**Figure 4.3. Myofibers with tubular mitochondria exhibit higher membrane potential.** TMRM staining of myofibers in the EDL (A-D) and soleus (E-H) muscles at 3 months of age. The intensity of TMRM signal is shown in the gradient. (B-D) Magnified images of the boxed zones in (A). Although most myofibers in the EDL have low TMRM signal, a myofiber containing tubular mitochondria exhibit TMRM staining that is comparable to soleus myofibers. (F-H) Magnified images of boxed regions in (E). Scale bar 10  $\mu\text{m}$ .

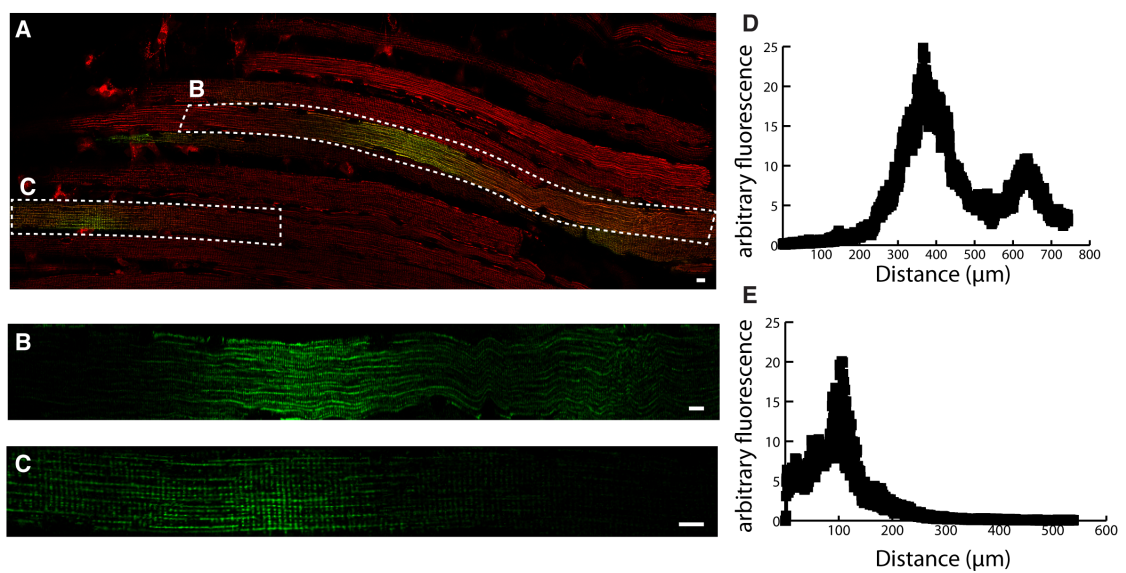
**Figure 4.4. Discrete mitochondrial domains along the myofiber.** EDL muscle was isolated from offsprings of the *Pax7CreER/PhAM*<sup>flaxed/flaxed</sup> mating at the postnatal age of 15 days. TMRM staining (red) was used as a counterstain for healthy myofibers. (A) Minimal mosaic activation of mito-Dendra2 (green) demonstrates compartments of mitochondrial network within the myofiber. (B and C) Mito-Dendra2 images of the labeled myofibers in (A) after linearizing along the horizontal axis of the myofiber. (D) Histogram showing the summed intensity of mito-Dendra2 signal along the horizontal axis of (B). (E) A similar plot analysis for (C). Scale bar 10  $\mu\text{m}$ .

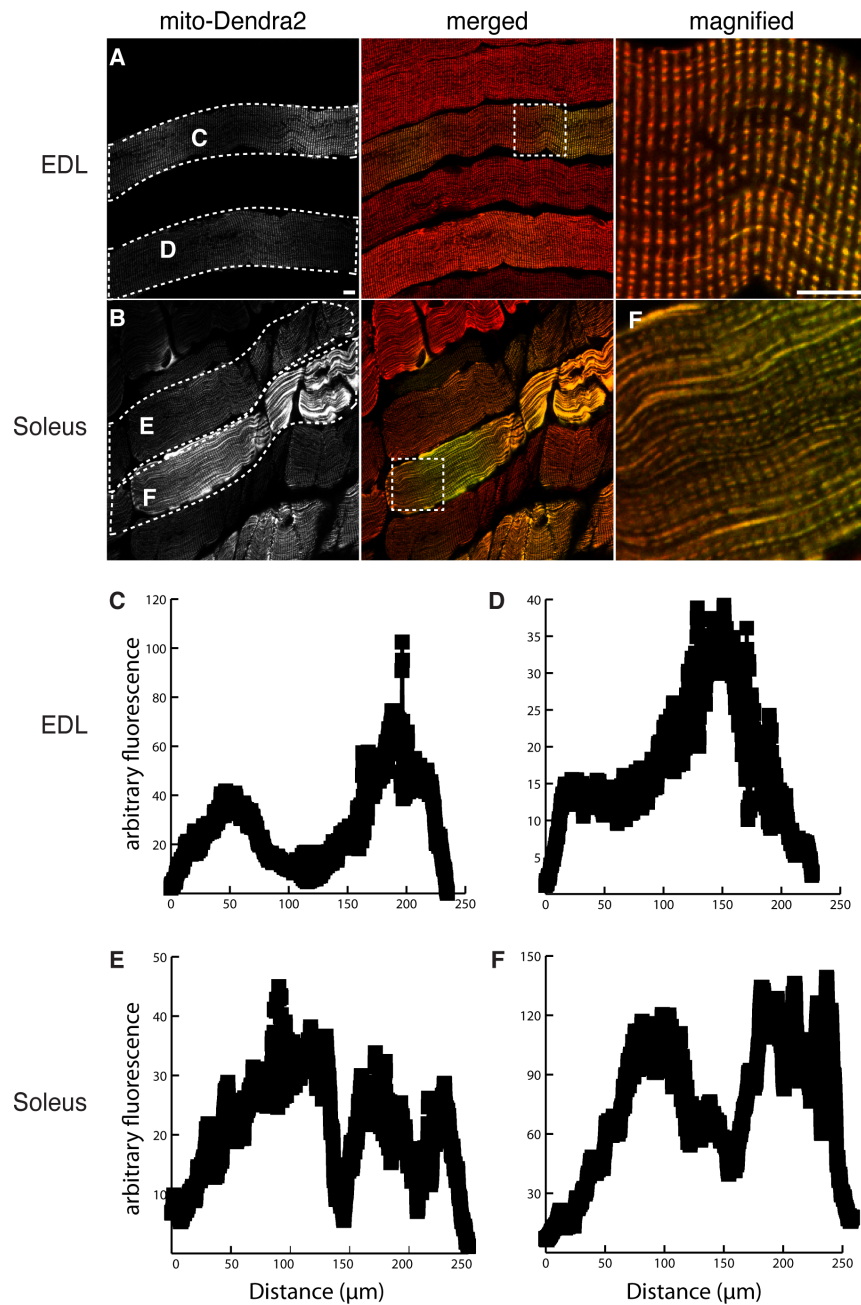
**Figure 4.5. Expansive mitochondrial domain in the soleus muscle.** EDL (A) and soleus (B) muscles were isolated from animals in the *Pax7CreER/PhAM*<sup>flaxed/flaxed</sup> mating at 3 months of age. Single channel images of mito-Dendra2 signal are shown in the first column. The merged images contain TMRM counterstain (red). The last column shows magnified images of the respective boxed region. (C and D) Intensity plots of the EDL myofibers labeled in (A). (E and F) Intensity plots of the soleus myofibers in (B). Scale bar 10  $\mu\text{m}$ .

**FIGURES****Figure 4.1**

**Figure 4.2**

**Figure 4.3**

**Figure 4.4**

**Figure 4.5**

## REFERENCES

- Agbulut, O., P. Noirez, et al. (2003). Myosin heavy chain isoforms in postnatal muscle development of mice. *Biol Cell* **95**: 399-406.
- Bach, D., D. Naon, et al. (2005). Expression of Mfn2, the Charcot-Marie-Tooth neuropathy type 2A gene, in human skeletal muscle: effects of type 2 diabetes, obesity, weight loss, and the regulatory role of tumor necrosis factor alpha and interleukin-6. *Diabetes* **54**(9): 2685-2693.
- Bach, D., S. Pich, et al. (2003). Mitofusin-2 determines mitochondrial network architecture and mitochondrial metabolism. A novel regulatory mechanism altered in obesity. *J Biol Chem* **278**(19): 17190-17197.
- Bo, H., Y. Zhang, et al. (2010). Redefining the role of mitochondria in exercise: a dynamic remodeling. *Ann N Y Acad Sci* **1201**: 121-128.
- Boncompagni, S., A. E. Rossi, et al. (2009). Mitochondria are linked to calcium stores in striated muscle by developmentally regulated tethering structures. *Molecular Biology of the Cell* **20**: 1058-1067.
- Bua, E., J. Johnson, et al. (2006). Mitochondrial DNA-deletion mutations accumulate intracellularly to detrimental levels in aged human skeletal muscle fibers. *Am J Hum Genet* **79**(3): 469-480.
- Bua, E. A., S. H. McKiernan, et al. (2002). Mitochondrial abnormalities are more frequent in muscles undergoing sarcopenia. *J Appl Physiol* **92**(6): 2617-2624.
- Cao, Z., J. Wanagat, et al. (2001). Mitochondrial DNA deletion mutations are concomitant with ragged red regions of individual, aged muscle fibers: analysis by laser-capture microdissection. *Nucleic Acids Res* **29**(21): 4502-4508.

- Chen, H., S. A. Detmer, et al. (2003). Mitofusins Mfn1 and Mfn2 coordinately regulate mitochondrial fusion and are essential for embryonic development. J Cell Biol **160**(2): 189-200.
- Chen, H., M. Vermulst, et al. (2010). Mitochondrial fusion is required for mtDNA stability in skeletal muscle and tolerance of mtDNA mutations. Cell. **141**: 280-289.
- Herbst, A., J. W. Pak, et al. (2007). Accumulation of mitochondrial DNA deletion mutations in aged muscle fibers: evidence for a causal role in muscle fiber loss. J Gerontol A Biol Sci Med Sci **62**(3): 235-245.
- Hiona, A. and C. Leeuwenburgh (2008). The role of mitochondrial DNA mutations in aging and sarcopenia: implications for the mitochondrial vicious cycle theory of aging. Exp Gerontol **43**(1): 24-33.
- Leary, S. C., C. N. Lyons, et al. (2003). Fiber-type differences in muscle mitochondrial profiles. Am J Physiol Regul Integr Comp Physiol **285**(4): R817-826.
- Lepper, C. and C. M. Fan (2010). Inducible lineage tracing of Pax7-descendant cells reveals embryonic origin of adult satellite cells. Genesis **48**(7): 424-436.
- Nishijo, K., T. Hosoyama, et al. (2009). Biomarker system for studying muscle, stem cells, and cancer in vivo. FASEB J **23**(8): 2681-2690.
- Ogata, T. and Y. Yamasaki (1997). Ultra-high-resolution scanning electron microscopy of mitochondria and sarcoplasmic reticulum arrangement in human red, white, and intermediate muscle fibers. Anat Rec **248**(2): 214-223.

- Olichon, A., L. Baricault, et al. (2003). Loss of OPA1 perturbs the mitochondrial inner membrane structure and integrity, leading to cytochrome c release and apoptosis. *J Biol Chem.* **278**: 7743-7746.
- Pham, A. H., J. M. McCaffery, et al. (2012). Mouse lines with photo-activatable mitochondria to study mitochondrial dynamics. *Genesis.*
- Picard, M., R. T. Hepple, et al. (2012). Mitochondrial functional specialization in glycolytic and oxidative muscle fibers: tailoring the organelle for optimal function. *Am J Physiol Cell Physiol* **302**(4): C629-641.
- Schiaffino, S., L. Gorza, et al. (1989). Three myosin heavy chain isoforms in type 2 skeletal muscle fibres. *J Muscle Res Cell Motil.* **10**: 197-205.
- Schiaffino, S. and C. Reggiani (1994). Myosin isoforms in mammalian skeletal muscle. *Journal of Applied Physiology.* **77**: 493-501.
- Seale, P. and M. A. Rudnicki (2000). A new look at the origin, function, and stem-cell status of muscle satellite cells. *Dev Biol.* **218**: 115-124.
- Seale, P., L. A. Sabourin, et al. (2000). Pax7 is required for the specification of myogenic satellite cells. *Cell.* **102**: 777-786.
- Wanagat, J., Z. Cao, et al. (2001). Mitochondrial DNA deletion mutations colocalize with segmental electron transport system abnormalities, muscle fiber atrophy, fiber splitting, and oxidative damage in sarcopenia. *FASEB J* **15**(2): 322-332.
- White, R. B., A.-S. Biérinx, et al. (2010). Dynamics of muscle fibre growth during postnatal mouse development. *BMC Dev Biol.* **10**: 21.
- Zammit, P. S., F. Relaix, et al. (2006). Pax7 and myogenic progression in skeletal muscle satellite cells. *J Cell Sci.* **119**: 1824-1832.

Zorzano, A., M. I. Hernandez-Alvarez, et al. (2010). Alterations in the mitochondrial regulatory pathways constituted by the nuclear co-factors PGC-1alpha or PGC-1beta and mitofusin 2 in skeletal muscle in type 2 diabetes. Biochim Biophys Acta **1797**(6-7): 1028-1033.

*Chapter 5*

## FUTURE DIRECTIONS

Although it is evident that mitochondrial dynamics is critical for the survival of many cell types, the function of mitochondrial fusion in cellular physiology is evolving as more tools are generated for monitoring mitochondria in tissues and disease models. Future avenues for research include elucidating other mechanistic roles for mitofusins in primary cells, assessing the redundancy of mitofusins in multiple tissues, and exploring the mitochondrial dynamics in sarcopenia.

**Roles of Mitofusins in Primary Cells**

Although mitofusins have been classically associated with mediating mitochondrial fusion, multiple lines of evidences suggest that these GTPases have potential roles in ER tethering, maintaining mtDNA, and organelle trafficking (Baloh, Schmidt et al. 2007; Detmer, Velde et al. 2007; de Brito and Scorrano 2008; Chen, Vermulst et al. 2010; Misko, Jiang et al. 2010). It is unclear whether mitofusins directly mediate these processes or exert indirect impact. Live imaging of fluorescently labeled ER and mitochondria may yield dynamic interactions between mitochondrial morphology and the ER network. The incorporation of calcium reporters as indicators of ER function may also provide some insight into the functional interactions between mitochondrial-ER contacts. To understand the prevalence of mitofusins in protecting mtDNA, it may be worthwhile to determine mtDNA levels in our dopaminergic mouse model. Since a previous report from our lab has demonstrated the importance of mitofusins in maintaining the integrity of mtDNA in

skeletal muscles (Chen, Vermulst et al. 2010), it would be worthwhile to determine the prevalence of this function in different tissues.

In the case of mediating mitochondrial transport in neurons, studies from our labs and others suggest that Mfn2 play an essential role in mitochondrial trafficking in multiple neuronal subtypes including the dorsal root ganglion, motor neurons, and dopaminergic neurons (Baloh, Schmidt et al. 2007; Detmer, Velde et al. 2007). A recent report has shown that Mfn2 can immunoprecipitate with the motor protein complexes, but the mechanistic function of Mfn2 in transport remains elusive (Misko, Jiang et al. 2010). Future experiments may be aimed at testing rescue strategies to address whether Mfn2 play complementary or independent roles with components of the motor complex. These efforts will be aided by the generation of conditional knockout mouse models of motor proteins.

It is also important to address these questions in an appropriate cellular model. Defects in any of these processes may not be critical for the survival of fibroblast cells or cell lines, but may lead to lethal effects in primary and terminally differentiated cells. Perhaps the primary and tissue models provide more physiological environments and stresses that recapitulate the vulnerability of the cells toward mitochondrial defects. Using the PhAM mouse lines we have generated, it is possible to visualize mitochondrial function and dynamics in any tissue or primary cells.

### **Dissecting the Tissue Specific Redundancy of *Mfn1* and *Mfn2***

Many studies support a complementary function for both mitofusins, but several knockout mouse models suggest a tissue-specific pattern of redundancy. Results from our

dopaminergic animal model clearly demonstrate the lack of defects when *Mfn1* is deleted in the single or double mitofusin deletion (Pham, Meng et al. 2012). Similarly, targeted deletion of *Mfn1* in cardiac tissues or post-placental development causes no defects compared to the *Mfn2* knockout mutants (Chen, Mccaffery et al. 2007; Papanicolaou, Khairallah et al. 2011; Papanicolaou, Ngoh et al. 2012). These reports suggest that *Mfn1* may be completely redundant to *Mfn2*. Nonetheless, in mouse embryonic fibroblasts and during placental and skeletal muscle development, Mfn1 exert nonredundant functions with Mfn2 for sustaining cell health (Chen, Detmer et al. 2003; Chen, Chomyn et al. 2005; Chen, Vermulst et al. 2010). Further characterization of the relative expression levels of mitofusins in specific tissues may help resolve the differential pattern of redundancy observed. The predominant expression of one mitofusin may determine the vulnerability of a particular tissue to the abrogation of *Mfn1* versus *Mfn2*. Interestingly, a recent *in vitro* assay of mitochondrial fusion suggests that heterotypic interactions between Mfn1-Mfn2 are more efficient (Hoppins, Edlich et al. 2011). Perhaps the relative expression levels of mitofusins may sensitize a particular tissue to defects in mitochondrial fusion.

### **Mitochondrial Dynamics in Sarcopenia**

Our preliminary analysis of mitochondria in skeletal muscles demonstrates differential patterns of mitochondrial dynamics across muscle types and developmental transitions. Studies from human tissues and animal models find a prevalence of mitochondrial defects occurring in fast twitch muscles (Wanagat, Cao et al. 2001; Bua, McKiernan et al. 2002; Hoppins, Edlich et al. 2011). These results provide the motivation to explore whether these vulnerabilities may be linked to differences in mitochondrial

dynamics. In our Pax7 analysis of mitochondrial domains, we observed variable mitochondrial domains between glycolytic and oxidative fibers. This result suggests that the complementation of mitochondrial defects may differ across fiber types. Whether mitochondrial complementation can lead to susceptibilities towards sarcopenia require further exploration. It will be prudent to quantify the exact mitochondrial domain in different fiber types and developmental ages.

## REFERENCES

- Baloh, R. H., R. E. Schmidt, et al. (2007). Altered Axonal Mitochondrial Transport in the Pathogenesis of Charcot-Marie-Tooth Disease from Mitofusin 2 Mutations. *Journal of Neuroscience*. **27**: 422-430.
- Bua, E. A., S. H. McKiernan, et al. (2002). Mitochondrial abnormalities are more frequent in muscles undergoing sarcopenia. *J Appl Physiol* **92**(6): 2617-2624.
- Chen, H., A. Chomyn, et al. (2005). Disruption of fusion results in mitochondrial heterogeneity and dysfunction. *J Biol Chem* **280**(28): 26185-26192.
- Chen, H., S. A. Detmer, et al. (2003). Mitofusins Mfn1 and Mfn2 coordinately regulate mitochondrial fusion and are essential for embryonic development. *The Journal of Cell Biology*. **160**: 189-200.
- Chen, H., J. McCaffery, et al. (2007). Mitochondrial Fusion Protects against Neurodegeneration in the Cerebellum. *Cell*. **130**: 548-562.
- Chen, H., M. Vermulst, et al. (2010). Mitochondrial fusion is required for mtDNA stability in skeletal muscle and tolerance of mtDNA mutations. *Cell*. **141**: 280-289.
- de Brito, O. M. and L. Scorrano (2008). Mitofusin 2 tethers endoplasmic reticulum to mitochondria. *Nature*. **456**: 605-610.
- Detmer, S. A., C. V. Velde, et al. (2007). Hindlimb gait defects due to motor axon loss and reduced distal muscles in a transgenic mouse model of Charcot-Marie-Tooth type 2A. *Human Molecular Genetics*. **17**: 367-375.
- Hoppins, S., F. Edlich, et al. (2011). The soluble form of Bax regulates mitochondrial fusion via MFN2 homotypic complexes. *Mol Cell* **41**(2): 150-160.

Misko, A., S. Jiang, et al. (2010). Mitofusin 2 is necessary for transport of axonal mitochondria and interacts with the Miro/Milton complex. *J Neurosci.* **30:** 4232-4240.

Papanicolaou, K. N., R. J. Khairallah, et al. (2011). Mitofusin-2 maintains mitochondrial structure and contributes to stress-induced permeability transition in cardiac myocytes. *Mol Cell Biol* **31**(6): 1309-1328.

Papanicolaou, K. N., G. A. Ngoh, et al. (2012). Cardiomyocyte deletion of mitofusin-1 leads to mitochondrial fragmentation and improves tolerance to ROS-induced mitochondrial dysfunction and cell death. *Am J Physiol Heart Circ Physiol* **302**(1): H167-179.

Pham, A. H., S. Meng, et al. (2012). Loss of Mfn2 results in progressive, retrograde degeneration of dopaminergic neurons in the nigrostriatal circuit. *Hum Mol Genet.* (In press)

Wanagat, J., Z. Cao, et al. (2001). Mitochondrial DNA deletion mutations colocalize with segmental electron transport system abnormalities, muscle fiber atrophy, fiber splitting, and oxidative damage in sarcopenia. *FASEB J* **15**(2): 322-332.

*A p p e n d i x A*

## PREPARING PARASAGITTAL ORGANOTYPIC SLICES

**I. Dissection tools**

Scalpel (to cut skin overlying the cranium)  
 Two spatula (filed at one edge to increase sharpness)  
 Big blunted scissor (head dissection)  
 Iris scissors-delicate (FST 14060-10)  
 Forceps to remove cranium  
 2 Individually wrapped transfer pipets with fine tip (VWR #**414004-037**)  
 - Cut the fine tip of the pipet to obtain a larger bore size. This is used to transfer tissue sections onto the chamber wells.  
 - One uncut fine tip pipet for removing media from the slices on the membrane  
 One medium fine brush (Robert Simmons White Sables #3 for transferring sections out of the vibratome media chamber  
 50 mL conicals to keep brain in submerged in cold 1X GBSS solution before sectioning  
 Prechilled metal plates as a cold cutting surface

**II. Equipment**

Leica vibratome (VT1200S)  
 Feather Double Edge Carbon Steel blade razor for tissue chopper (Ted Pella #**1219**)  
 Vacuum filter sterilizer for medium, 0.22 µm pore size (Millipore Stericup & Steritop #**SCGPU02RE**)  
 Cell culture incubator at 35°C, 95% air, 5% CO<sub>2</sub>  
 Sterilized culture plate inserts, 0.4 µm membrane thickness (Millipore Millicell membrane, 30 mm diameter, #**PICM03050**)  
 6-well culture plates  
 12-well culture dishes  
 Converters blue film self seal sterilization pouch 5" x 10" (VWR #**11213-241**)

**III. Reagents**

<b>MEM 1X</b> Contains Earle's salts and L-glutamine	Invitrogen	SKU <b>11095-080</b>
<b>MEM 1X (Phenol-red Free)</b> Contains Earle's salts and no L-Glutamine		SKU 51200-038
<b>10X HBSS (Hank's Balanced Salt Solution)</b> No calcium chloride, magnesium chloride, magnesium sulfate, sodium bicarbonate, or phenol red	Invitrogen	SKU <b>14185-052</b>
<b>Horse serum, heat-inactivated</b> EIA tested (negative) serum from a donor herd	Invitrogen	SKU <b>26050-088</b>

<b>1M HEPES buffer solution</b>	Invitrogen	<b>SKU 15630-080</b>
<b>100X GlutaMAX I supplement</b> 200 mM supplied in 0.85% NaCl. Extremely stable in aqueous solution.	Invitrogen	<b>SKU 35050-061</b> Lot# 612197
<b>100X Penicillin/Streptomycin</b> 10,000 U/mL & 10,000 µg/mL (100X stock)	Invitrogen	<b>SKU 15140-122</b>
<b>GBSS (Gey's Balanced Salt Solution)</b> Sterile-filtered, cell culture tested Add 6.5mg/mL D-glucose to supplement	Sigma	<b>G9779-500ML</b> Lot# 128K2368

#### IV. Preparation

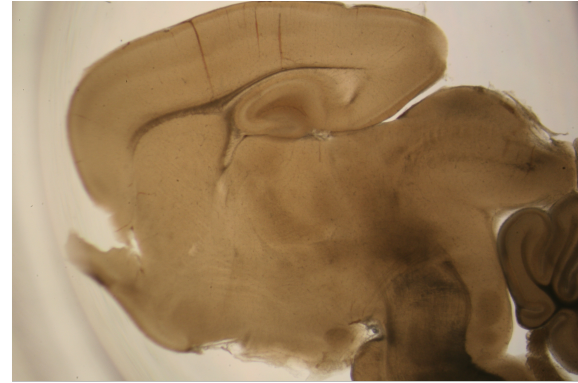
- a. Autoclave the vibratome plastic media chamber and the following dissection equipment in the sterilization pouch.
  - 1. Scalpel handle
  - 2. Forceps
  - 3. Scissors

b. Spray the fine paint brushes with 70% EtOH to sterilize.

#### V. Technique

- a. Add 1 mL of Stoppini media into each well of a six-well plate and place one membrane insert into each well. Keep plate in the incubator to warm during the dissection.
- b. Aliquot 1X GBSS supplemented with 6.5 mg/mL of glucose into 12-well plate & 50 mL conical.
- c. Place several filter papers on the prechilled metal plates and wet filter paper with GBSS solution.
- d. Transect head of P10-P12 pups.
- e. Disinfect the head and scissors with 70% EtOH.
- f. Use the scalpel to make a midline longitudinal cut and push the skin rostrally to visualize the skull.
- g. Use the sharp scissor to cut the cranium at midline from caudal to rostral (beginning from spinal cord towards forebrain).
- h. Use forceps to open the cranium and expose the brain. Gently remove the brain from the rostral end (begin at the olfactory tubercle) using a spoon spatula.
- i. Place brain in 50 mL conical containing GBSS and place on ice until ready for sectioning. Continue dissecting until 3-4 brains are on ice.
- j. Use a spoon spatula to transfer the brain onto the GBSS wetted filter paper.
- k. Trim the lateral edges of the cortex to create a flat surface for gluing the brain on the specimen holder. Make a longitudinal cut at midline to separate the brain hemisphere.

- l. Place a small strip of tape in the center of the specimen holder and add 2 drops of glue (one for each hemisphere). Place the brain hemispheres in parallel such that the medial surface faces upward (an open book position).
- m. Position the specimen plate onto the magnetic stage. Orient the brain such that the caudal end (cerebellar end) is closest to the blade. Tilt the specimen at the maximum angle up toward you).
- n. Settings for the vibratome:
  1. Speed: 0.22 mm/s
  2. Amplitude: 2.00 mm
  3. Thickness: 330  $\mu\text{m}$
- o. Keep slices that look like the image below (this should occur within 3-4 sections).
- p. Transfer the brain slices into 12-well plate (on ice) containing GBSS solution and keep the plate on ice until 6 brains have been dissected & sectioned.
- q. Transfer brains onto membrane inserts using the large bore transfer pipette. Remove as much GBSS as possible using the fine tip transfer pipette. Place the 6-well plate into the cell incubator.
- r. Change the media 24 hours after the dissection. Subsequently, feed slices 3 times per week every other day.



## VI. Immunostaining for slice health

Antibodies	Type	Host	Company	Cat#	Dilution	
<b>anti-Tyrosine Hydroxylase (TH)</b>	Polyclonal	Rabbit	Millipore/C hemicon	AB152	1:500	IF
<b>anti-Microtubule associated protein (MAP2)</b>	Monoclonal	Mouse	Sigma	M4403	1:1000	IF
<b>Fluoro-Jade C</b>	Dye		Millipore	AG325	0.0001%	IHC
<b>anti-Dopamine Transporter (DAT)</b>	Monoclonal	Rat	Millipore	MAB369	1:75	IF

### a. Supplies:

16% Formaldehyde (w/v) [Thermo-Scientific, 10 mL ampules, #28908]  
 L-Lysine monohydrochloride [Sigma # L5626]  
 Sodium (meta)periodate [Sigma # S1878-25G]

Glycine [JT Baker #4059-06]  
 Richard-Allan Cytoseal XYL 60 mounting medium [Thermo Scientific #8310-4]  
 Normal Goat Serum

0.2M Sodium phosphate monobasic (anhydrous)	<b>500 mL</b> 12 g	<b>200 mL</b> 4.8 g
0.2 M Sodium phosphate dibasic (anhydrous)	<b>1L</b> 28.3 g	<b>500 mL</b> 14.2 g
0.1M PBS (pH 7.3-7.4)	<b>1L</b> 100 mL sodium phosphate <u>monobasic</u> 400 mL sodium phosphate <u>dibasic</u> Add 450 mL ddH <sub>2</sub> O pH to 7.3-7.4 Add water for total of 1 L	<b>500 mL</b> 50 mL sodium phosphate <u>monobasic</u> 200 mL sodium phosphate <u>dibasic</u> Add 200 mL ddH <sub>2</sub> O pH to 7.3-7.4 Add water for total of 500 mL
Lysine-phosphate buffer	3.66 g L-Lysine monohydrochloride 100 mL ddH <sub>2</sub> O pH to 7.4 with dibasic sodium phosphate Double the total volume with the 0.1M PBS	
16% Paraformaldehyde	16 g paraformaldehyde in 100 mL ddH <sub>2</sub> O heated slowly to 60°C. Add drops of 1N NaOH with stirring until paraformaldehyde dissolves. Add 5.4 g glucose.	
Periodate-lysine-phosphate fixative (~ lasts 1-2 months if stored at 4°C)	10 mL preprepared 16% formaldehyde ampule 0.54 g glucose 30 mL of lysine-phosphate buffer 0.084 g periodate	
Stop solution (50 mM glycine in 0.1M phosphate buffer)	<b>50 mL</b> 0.1876 g	<b>200 mL</b> 0.7507g
1% Triton X permeabilization in 0.1M phosphate buffer	<b>20 mL</b> 2 mL 10% TX-100	<b>40 mL</b> 4 mL 10% TX-100
Deerinck Block (in 0.1M phosphate buffer)	<b>100 mL</b> 2 mL Normal Goat serum (2% final) 1 g BSA (1% final) 2.5 mL of 10% Triton X (0.25% final)	<b>200 mL</b> 4 mL Normal Goat serum (2% final) 2 g BSA (1% final) 5 mL of 10% Triton X (0.25% final)
Deerinck working solution (for antibody & washing)	<b>100 mL</b> 0.2 mL Normal goat serum (0.2% final)	<b>200 mL</b> 0.4 mL Normal goat serum (0.2% final)

	0.1 g BSA (0.1% final) 1 mL of 10% Triton X (0.1% final)	0.2 g BSA (0.1% final) 2 mL of 10% Triton X (0.1% final)
--	---	---

b. Protocol

1. Trim the Millicell insert and transfer the membrane & slice to a 24 well plate containing PLP fixative. Fix for 5 min at 37°C and subsequently fix for O.N. at 4°C.
2. Wash fixative 3X with PBS for 5 min each time.
3. Inhibit the fixation with 5 min incubation of 0.1M of glycine
4. Permeabilize with 1% Triton-X for 30 min at RT.
5. Block in Deerinck block buffer for 4-6 hrs at RT or O.N. at 4°C.
6. Apply primary antibody diluted in Deerinck working solution and incubate for O.N. at 4°C.
7. Rinse primary antibody 3X with PBS for 10 min each time.
8. Apply secondary antibody for 2 hrs at RT

**1X Gey's Balanced Salt Solution (GBSS) [1 L]**

**pH to 7.1-7.2 (10X solution does not dissolve)**

CaCl <sub>2</sub>	0.2251 g
CaCl <sub>2</sub> ·2H <sub>2</sub> O	0.298 g
MgCl <sub>2</sub> ·6H <sub>2</sub> O	0.21 g
MgSO <sub>4</sub> (anhydrous)	0.0342 g
MgSO <sub>4</sub> ·7H <sub>2</sub> O	0.0700 g
KCl	0.37 g
KH <sub>2</sub> PO <sub>4</sub> (anhydrous)	0.03 g
NaHCO <sub>3</sub>	2.27 g
NaCl	7.0 g
Na <sub>2</sub> HPO <sub>4</sub> (anhydrous)	0.1196 g
Na <sub>2</sub> HPO <sub>4</sub> ·7H <sub>2</sub> O	0.2258 g
D-glucose	1.0 g

Supplement with D-glucose (6.5 mg/mL) when using for slice preparation

**Stoppini Media (100 mL)**

MEM	50 mL
Heat inactivated horse serum	25 mL
10X HBSS	1 mL
1 M HEPES	1 mL
100X L-GlutaMAX-I	0.5 mL
100X L-Glutamine	1 mL
100X Pen-Strep	1 mL
ddH <sub>2</sub> O	18.5 mL
D-glucose	0.65 g
pH to 7.2 with NaOH	

# Broad activation of the ubiquitin–proteasome system by Parkin is critical for mitophagy

Nickie C. Chan<sup>1,2</sup>, Anna M. Salazar<sup>1</sup>, Anh H. Pham<sup>1</sup>, Michael J. Sweredoski<sup>1,3</sup>, Natalie J. Kolawa<sup>1</sup>, Robert L.J. Graham<sup>1,3</sup>, Sonja Hess<sup>1,3</sup> and David C. Chan<sup>1,2,\*</sup>

<sup>1</sup>Division of Biology, <sup>2</sup>Howard Hughes Medical Institute and <sup>3</sup>Proteome Exploration Laboratory/Beckman Institute, California Institute of Technology, Pasadena, CA 91125, USA

Received January 27, 2011; Revised and Accepted February 1, 2011

Parkin, an E3 ubiquitin ligase implicated in Parkinson's disease, promotes degradation of dysfunctional mitochondria by autophagy. Using proteomic and cellular approaches, we show that upon translocation to mitochondria, Parkin activates the ubiquitin–proteasome system (UPS) for widespread degradation of outer membrane proteins. This is evidenced by an increase in K48-linked polyubiquitin on mitochondria, recruitment of the 26S proteasome and rapid degradation of multiple outer membrane proteins. The degradation of proteins by the UPS occurs independently of the autophagy pathway, and inhibition of the 26S proteasome completely abrogates Parkin-mediated mitophagy in HeLa, SH-SY5Y and mouse cells. Although the mitofusins Mfn1 and Mfn2 are rapid degradation targets of Parkin, we find that degradation of additional targets is essential for mitophagy. These results indicate that remodeling of the mitochondrial outer membrane proteome is important for mitophagy, and reveal a causal link between the UPS and autophagy, the major pathways for degradation of intracellular substrates.

## INTRODUCTION

Parkin and PINK1 are Parkinson's disease (PD)-related proteins that operate in a common pathway to ensure mitochondrial integrity (1–5). Recent studies indicate that Parkin monitors the quality of the mitochondrial population and translocates from the cytosol onto dysfunctional mitochondria (6–11). Once on mitochondria, it promotes their degradation via mitophagy, an autophagic pathway specific for mitochondria (8). Loss of this surveillance mechanism presumably contributes to the accumulation of degenerative mitochondria observed in Parkin mutant flies (1,2,4).

Molecular models of Parkin function have evolved over the last decade. Parkin is an E3 ubiquitin ligase (12), and some disease alleles have impaired enzymatic activity (6,12,13). Because PD is characterized pathologically by intracellular protein aggregates termed Lewy bodies, early models postulated that Parkin functioned to promote the ubiquitin–proteasome system (UPS), which is activated by K48-linked polyubiquitination of substrate proteins (14). Mutation of Parkin would impair

the ubiquitin–proteasome pathway (UPS) of protein degradation, leading to the toxic accumulation of misfolded or aggregated proteins. Since the discovery that Parkin promotes mitophagy (8), however, recent models have instead emphasized the ability of Parkin to mediate K63-linked polyubiquitin chains, distinct from the classic K48-linked polyubiquitin chains associated with the UPS. The topology of the polyubiquitin chain linkage determines the cellular outcome of polyubiquitination (15). It has been shown that the K63-linked ubiquitination of mitochondrial proteins by Parkin activates the autophagic machinery through recruitment of ubiquitin binding adaptors, such as HDAC6 and p62/SQSTM1 (6,13,16). The importance of this mechanism requires clarification, however, because p62/SQSTM1 null cells have no defect in Parkin-mediated mitophagy (17,18). Thus, the key molecular events occurring between Parkin-mediated ubiquitination of mitochondrial proteins and the degradation of mitochondria by the autophagic pathway remain unresolved.

To elucidate the proximal function of Parkin, we used quantitative proteomics to define, in an unbiased and highly comprehensive

\*To whom correspondence should be addressed at: California Institute of Technology, Howard Hughes Medical Institute, 1200 E. California Blvd., MC114-96, Pasadena, CA 91125, USA. Tel: +1 6263952670; Fax: +1 6263958826; Email: dchan@caltech.edu

**Table 1.** Proteins with altered abundance in the mitochondria of CCCP-treated cells

Protein	Biological function	SILAC ratio <sup>a</sup>	Significance <sup>b</sup>
Increased proteins			
PARKIN	E3 ubiquitin ligase	13	4.42E-20
DRP1	Mitochondrial fission	6.3	4.78E-07
Autophagy related			
NBR1	Autophagy adaptor	8.3	2.90E-06
p62/SQSTM1	Autophagy adaptor	5.8	1.75E-06
MAP1LC3B2;MAP1LC3B	Autophagosome component	5.4	3.70E-06
GABARAPL2	Autophagosome component	3.4	7.87E-06
ATP6V1B2	V-type proton ATPase subunit	3.3	1.64E-05
ATP6V1E1	V-type proton ATPase subunit	3.1	4.77E-03
ATP6V1C1	V-type proton ATPase subunit	2.9	7.23E-03
ATP6V1A	V-type proton ATPase subunit	2.9	2.45E-03
UPS related			
Ubiquitin	Protein modification	8.9	9.58E-15
PSMA2	20S proteasome subunit	4.2	8.08E-05
PSMB5	20S proteasome subunit	4.2	4.21E-04
PSMA1	20S proteasome subunit	4.0	5.38E-04
PSMB3	20S proteasome subunit	4.0	6.20E-04
PSMB6	20S proteasome subunit	3.9	2.30E-04
PSMA6	20S proteasome subunit	3.7	1.18E-03
PSMB4	20S proteasome subunit	3.7	1.96E-03
PSMA7	20S proteasome subunit	3.7	1.29E-03
PSMA4	20S proteasome subunit	3.6	4.70E-04
PSMA3	20S proteasome subunit	3.6	4.85E-04
PSMB1	20S proteasome subunit	3.3	2.66E-03
PSMA5	20S proteasome subunit	3.2	9.68E-04
PSMD6	19S proteasome subunit	2.7	6.22E-03
PSMD2	19S proteasome subunit	2.5	6.38E-03
Decreased proteins <sup>c</sup>			
MFN1	Mitochondrial fusion	0.09	6.94E-18
MFN2	Mitochondrial fusion	0.10	2.51E-35
TOM70	Mitochondrial import	0.13	3.78E-40
MIRO1/RHOT1	Mitochondrial transport	0.16	4.29E-15
CPT1A	Fatty acid metabolism	0.23	1.62E-21
MOSC2	Oxidoreductase	0.26	6.67E-10
MITONEET/CISD1	Regulation of respiration	0.26	8.74E-18
GPAM	Glycerolipid synthesis	0.42	3.39E-04
MIRO2/RHOT2	Mitochondrial transport	0.44	4.94E-06
FIS1	Mitochondrial fission	0.55	1.33E-03

Summary of the most significantly altered proteins in mitochondria isolated from Parkin-expressing HeLa S3 cells after treatment with or without CCCP for 2 h.

<sup>a</sup>Combined SILAC ratio from three independent mass spectrometry experiments consisting of two independent biological samples, and one technical replicate. In one of the experiments, the SILAC cells were reverse labeled with SILAC. The ratio represents the protein level in mitochondria of CCCP-treated cells divided by the level in untreated cells.

<sup>b</sup>Corresponds to the significance calculated in MaxQuant.

<sup>c</sup>Only MitoCarta proteins annotated as 'outer membrane proteins' in Uniprot are shown.

manner, how the mitochondrial proteome changes in response to Parkin activity. Our results indicate that in addition to K63-linked polyubiquitination, the K48-mediated UPS pathway has a major role in Parkin-dependent mitophagy. We observe robust recruitment of the 26S proteasome onto mitochondria, leading to widespread degradation of mitochondrial outer membrane proteins via the UPS. Strikingly, activation of the UPS not only precedes mitophagy, but is required for mitophagy. Inhibition of the UPS causes complete abrogation of mitophagy.

## RESULTS

### Parkin activation results in changes to the mitochondrial proteome

We performed stable isotope labeling by amino acids in cell culture (SILAC) analysis (19) to monitor changes in the

mitochondrial proteome in a clonal Parkin-expressing HeLa S3 cell line after a 2 h treatment with carbonyl cyanide m-chlorophenylhydrazone (CCCP). CCCP dissipates the mitochondrial membrane potential, resulting in recruitment of Parkin to mitochondria and Parkin-dependent mitophagy (8). With this mass spectrometry-based approach, we quantified 2979 unique protein groups. Of these, 766 were mapped to proteins in the human MitoCarta inventory (20), which contains 1013 mitochondrial proteins. This represents a highly comprehensive coverage of the mitochondrial proteome, especially given that cultured cell lines express fewer mitochondrial proteins than tissues.

To sort through the proteins with altered SILAC ratios, we set a stringent threshold by considering only those with a calculated significance of <0.01 (Table 1 and Supplementary Material, Tables S1–S4). As expected, Parkin was highly

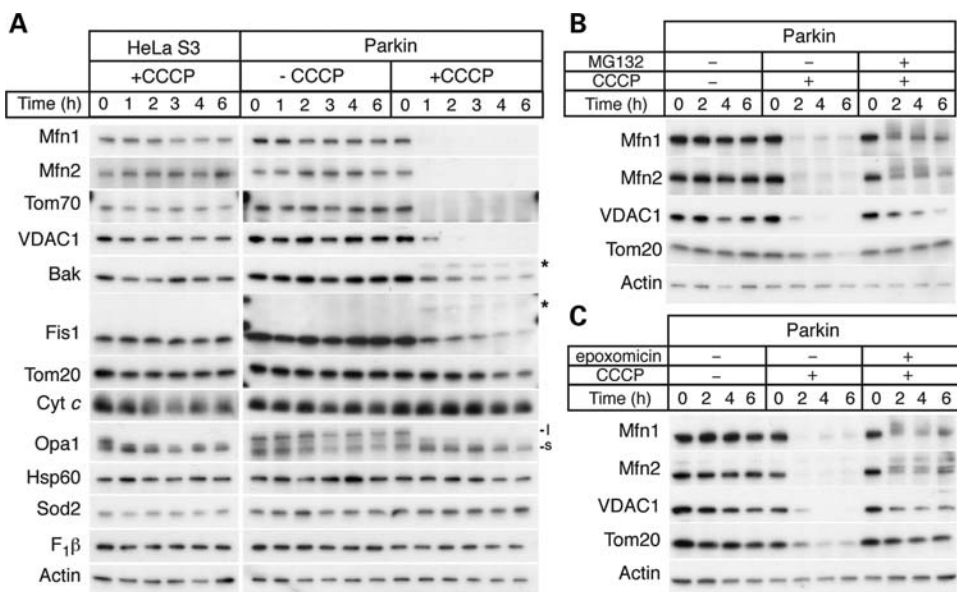


**Figure 1.** Parkin mediates extensive proteolysis of outer membrane proteins via the UPS. (A) Parkin- and CCCP-dependent proteolysis of mitochondrial outer membrane proteins. HeLa S3 cells or clonal Parkin-expressing HeLa S3 cells were treated with vehicle or 20  $\mu$ M CCCP to dissipate the mitochondrial membrane potential. Total cell lysates at the indicated time points were analyzed by immunoblotting for the indicated proteins. Outer membrane proteins: Mfn1, Mfn2, Tom70, VDAC1, Bak, Fis1, Tom20. Intermembrane space protein: cytochrome *c*. Inner membrane protein: Opa1. Matrix proteins: Hsp60, Sod2, F1 $\beta$ . Loading control: actin. (B) Inhibition of outer membrane protein degradation by the proteasome inhibitor MG132. Immunoblot analysis of Mfn1, Mfn2, VDAC1, Tom20 and actin (loading control) levels after CCCP with or without treatment with the proteasome inhibitor MG132 (10  $\mu$ M). (C) Inhibition of outer membrane protein degradation by the proteasome inhibitor epoxomicin. Same as (B), except epoxomicin (2  $\mu$ M), a more specific proteasome inhibitor, was used.

enriched (13-fold) in mitochondria after CCCP treatment. Consistent with studies indicating that Parkin translocation leads to mitophagy, we found enrichment of several autophagy-related proteins, including p62/SQSTM1, NBR1, LC3 and the LC3 family member GABARAPL2. In addition, we found an increase in several subunits of the V-type proton ATPase, which is a component of acidic organelles, such as endosomes and lysosomes. The mitochondrial fission factor Drp1 was also substantially enriched, and probably contributes to the fragmentation of mitochondria observed after CCCP treatment.

In addition to the autophagy pathway, the SILAC data provided evidence for a major induction of the ubiquitin–proteasome system (UPS). Firstly, ubiquitin was 9-fold more abundant in the mitochondria of CCCP-treated cells (Table 1). Secondly, numerous subunits of the proteasome were identified as enriched. This included subunits of both the 20S core particle and the 19S regulatory particle, thereby suggesting that 26S proteasomes are recruited to CCCP-treated mitochondria. Finally, we found a number of mitochondrial proteins that were substantially underrepresented after CCCP treatment. Among them, there are proteins from all four mitochondrial sub-compartments. Because Parkin translocates to the surface of mitochondria, we focused on outer membrane proteins, which are more likely to represent proximal effects of Parkin translocation.

Mitochondrial outer membrane proteins were overrepresented in the list of mitochondrial proteins with reduced abundance (Table 1). Although mitochondrial outer membrane proteins make up only 5% of the quantified mitochondrial proteins in our SILAC experiment, they constitute

20% of the reduced abundance proteins ( $P = 0.00014$ ). The most severely reduced outer membrane proteins include the mitofusins Mfn1 and Mfn2, which mediate mitochondrial fusion. In addition, Miro1 and Miro2, which are involved in mitochondrial transport along microtubules, are also highly reduced. These data, along with the increase in Drp1, support the recent suggestion that Parkin, as part of a quality control mechanism, may serve to restrict defective mitochondria from fusing with neighboring mitochondria (11,21). Although several proteins involved in mitochondrial dynamics are degraded by Parkin, the list of rapidly degraded mitochondrial proteins is broad and includes ones involved in protein import and various biosynthetic pathways. For example, the mitochondrial import receptor subunit Tom70 is one of the most severely reduced proteins.

### Parkin promotes degradation of mitochondrial outer membrane proteins

To extend these findings, we used immunoblotting to monitor the abundance of specific mitochondrial proteins in response to CCCP treatment. In agreement with our SILAC data, we found rapid degradation of Mfn1, Mfn2 and Tom70 upon CCCP treatment of Parkin-expressing cells (Fig. 1A). Almost complete degradation of these proteins occurred within the first hour of CCCP treatment. Such degradation was dependent on Parkin, because the levels of Mfn1, Mfn2 and Tom70 remained unchanged with CCCP in the parental HeLa S3 cells (Fig. 1A), which do not express Parkin (Supplementary Material, Fig. S1A). Similarly, we found Parkin-dependent degradation of other outer membrane proteins,

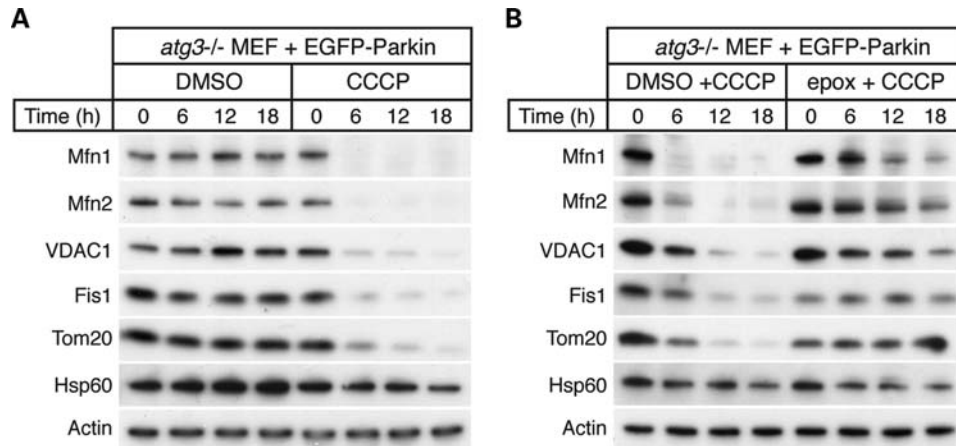


**Figure 2.** Proteolysis of the outer membrane occurs independently of the autophagy pathway. (A) CCCP-dependent degradation of mitochondrial outer membrane proteins in Atg3-null MEFs expressing Parkin. Atg3-null MEFs expressing EGFP-Parkin were treated with dimethyl sulfoxide (DMSO) (vehicle) or 20 µM CCCP for the indicated time. Total cell lysates were isolated and immunoblotted against the indicated proteins. (B) Inhibition of outer membrane protein degradation by the proteasome inhibitor epoxomicin. Atg3-null MEFs expressing EGFP-Parkin were treated with DMSO (vehicle) or the proteasome inhibitor epoxomicin (2 µM) for 2 h prior to treatment with 20 µM CCCP for the indicated times. Total cell lysates were isolated and immunoblotted against the indicated proteins.

although with slower kinetics. These proteins support a range of mitochondrial activities, including solute transport (VDAC1), regulation of apoptosis (Bak), mitochondrial fission (Fis1) and protein import (Tom20). Because of the slower kinetics, some of these proteins were not identified as reduced in the SILAC experiment, where cells were analyzed after 2 h of CCCP treatment. For Bak and Fis1, higher molecular weight species appeared after CCCP treatment (asterisks, Fig. 1A). No significant changes were observed for several mitochondrial matrix proteins, as well as the intermembrane space protein cytochrome *c*. In addition, there was only a slight reduction in the short isoforms of Opa1, an inner membrane protein. As reported previously, the long isoform of Opa1 is degraded in response to CCCP treatment (22,23), but in a Parkin-independent manner.

To determine whether the observed Parkin-mediated degradation of outer membrane proteins is dependent on the UPS, we incubated cells with proteasome inhibitors before treatment with CCCP (Fig. 1B and C). Indeed, inhibition of the proteasome with either MG132 or epoxomicin substantially blocked the degradation of Mfn1, Mfn2, VDAC1 and Tom20. In the case of Mfn1, Mfn2 and VDAC, this treatment also resulted in higher molecular weight species (asterisks, Fig. 1B and C). Therefore, we conclude that a proximal function of Parkin recruitment to depolarized mitochondria is to mediate the proteasome-dependent degradation of multiple mitochondrial outer membrane proteins. The degradation of outer membrane proteins was less efficient in HeLa cells expressing the R275W mutant, which has a partial defect in ubiquitination (Supplementary Material, Fig. S1B) (6).

We obtained similar protein degradation profiles by treating cells with valinomycin, a potassium ionophore that dissipates the electric potential across the inner membrane of mitochondria (Supplementary Material, Fig. S1C). In contrast, treatment with the complex I inhibitor rotenone did not result in outer membrane protein degradation (Supplementary Material, Fig. S1C). These results support the view that Parkin is activated by severe mitochondrial depolarization, rather than by

mitochondrial dysfunction *per se* (24). Indeed, Parkin does not localize to mitochondria upon treatment with rotenone (25).

#### Degradation of outer membrane proteins occurs independently of autophagy

As in HeLa cells, expression of Parkin in mouse embryonic fibroblasts (MEFs) results in CCCP-induced mitophagy (8,17,18,26). We took advantage of the genetic tractability of this system to determine whether Parkin-dependent degradation of mitochondrial outer membrane proteins occurs independently of the autophagy pathway. Atg3 is an E2-like enzyme that is essential for conjugation of Atg8/LC3 to phosphatidylethanolamine, an early step in the induction of autophagosomes. Atg3-null MEFs do not show LC3 conjugation and are defective in autophagy (27). We found that Parkin-expressing Atg3-null MEFs underwent mitochondrial outer membrane protein degradation in response to CCCP (Fig. 2A). This degradation was blocked by epoxomicin (Fig. 2B). These results indicate that Parkin-mediated degradation of outer membrane proteins occurs via the proteasome and independently of the autophagy pathway.

#### Recruitment of the proteasome to depolarized mitochondria

The UPS is classically associated with polyubiquitination via the K48 residue of ubiquitin (15). In our SILAC analysis, we found a substantial increase in both K48-linked (9-fold) and K63-linked (28-fold) polyubiquitination in mitochondria of cells treated with CCCP (Fig. 3A). We independently confirmed these mass spectrometric observations by immunoblot analysis using anti-polyubiquitin antibodies that are linkage specific (Fig. 3B). The increases in K48-linked and K63-linked polyubiquitin are both Parkin- and CCCP-dependent. Our SILAC data also indicated the accumulation of multiple 26S proteasome subunits to CCCP-treated mitochondria

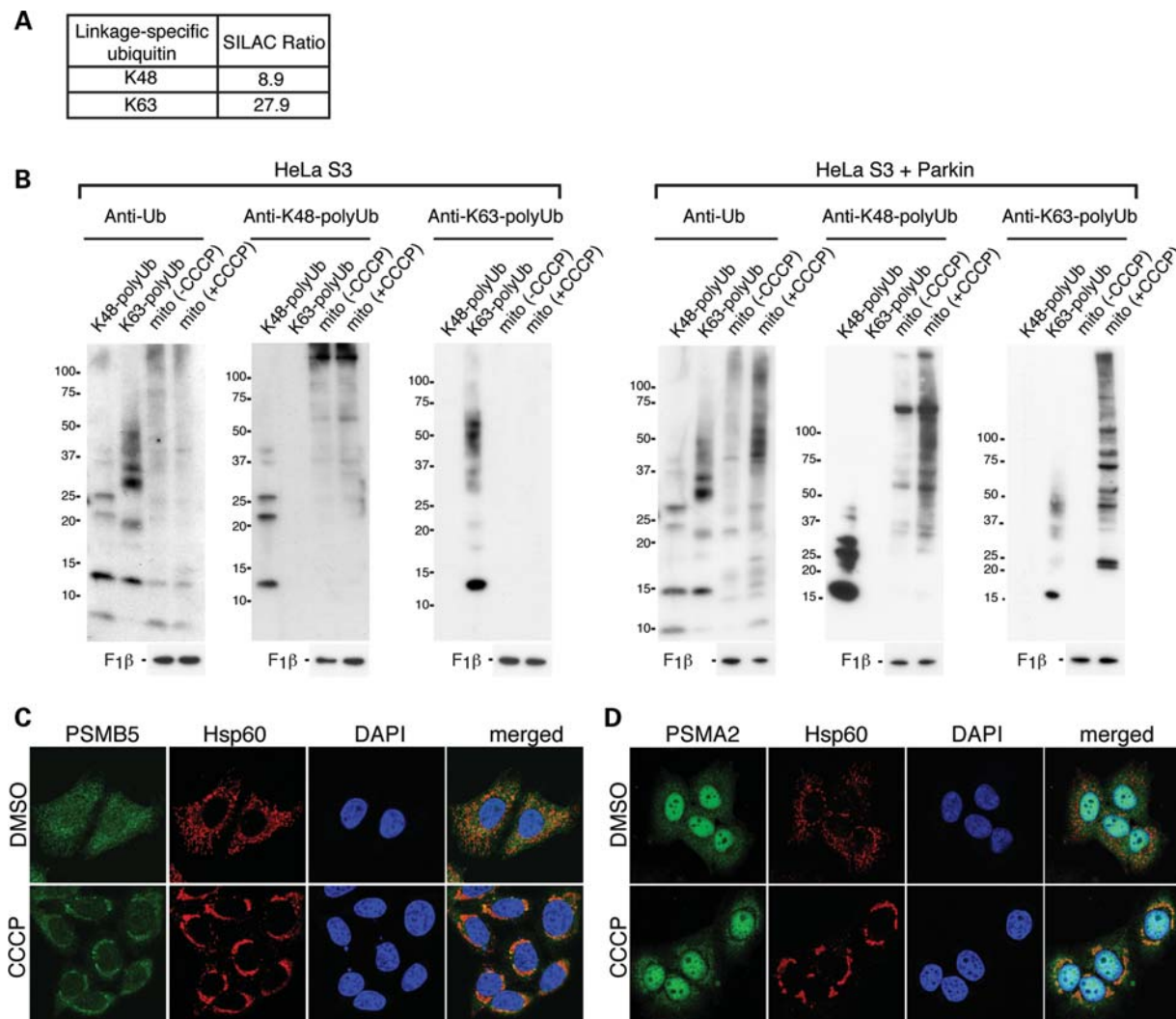


**Figure 3.** Parkin activation results in mitochondrial K48-linked and K63-linked polyubiquitination and proteasome recruitment. (A) The SILAC ratio for K48-linked and K63-linked polyubiquitination obtained from mass spectrometric analysis of mitochondria isolated after 2 h of CCCP treatment. Both modifications yield unique diglycine signature peptides that can be quantified (41). Mitochondria were isolated under conditions where the activity of the 26S proteasome was not inhibited. (B) Accumulation of K48- and K63-linked polyubiquitinated proteins in mitochondria of CCCP-treated cells. Immunoblot analysis of mitochondria isolated from HeLa S3 or Parkin-expressing HeLa S3 cells, with or without CCCP treatment. Blots were probed with the following antibodies: anti-ubiquitin, anti-K48-linked polyubiquitin, anti-K63-linked polyubiquitin and anti-F1β (loading control). Purified polyubiquitin chains of the K48-linked or K63-linked type were used as controls to verify the specificity of the antibodies used. Cells were pretreated with the proteasome inhibitor MG132 (10 μM) together with CCCP, and mitochondria were isolated in the presence of N-ethylmaleimide (10 mM) to prevent deubiquitination. (C) Analysis of proteasome localization. HeLa cells expressing Parkin were treated with DMSO (vehicle) or 20 μM CCCP for 4 h. Formalin-fixed cells were stained for the β subunit PSMB5 of the proteasome (green), Hsp60 (red) and nuclei [4',6-diamidino-2-phenylindole (DAPI), blue]. (D) Same as (C), except cells were immunostained for PSMA2 (green), an α subunit of the proteasome.

(Table 1). We confirmed this observation by immunostaining against α and β subunits of the proteasome. In Parkin-expressing HeLa cells, the anti-proteasome staining was diffusely cytosolic, but a clear enrichment on mitochondria was found upon CCCP treatment (Fig. 3C and D).

#### Degradation of mitochondrial outer membrane proteins precedes mitophagy

Given our finding that Parkin mediates proteolysis of outer membrane proteins, we investigated the temporal relationship of this process to mitophagy. We compared the behavior of the outer membrane marker Tom20 to the matrix marker Hsp60,

which is not degraded by the UPS (Fig. 1A). When Parkin-expressing HeLa cells were treated with CCCP for 4 h, two populations of mitochondria could be distinguished (Fig. 4A). The bulk of the mitochondria aggregated around the perinuclear region, consistent with previous studies (6,10,17). These perinuclear aggregates were positive for both Tom20 and Hsp60, although discrete patches were negative for Tom20 (Fig. 4B, filled arrowhead). The second population consisted of individual mitochondria dispersed in the cell periphery. Remarkably, in all cells, this second mitochondrial population was strongly positive for Hsp60, but devoid of any Tom20 signal (Fig. 4A and B). These results indicate that the loss of Tom20 is distinct from mitophagy. Both the

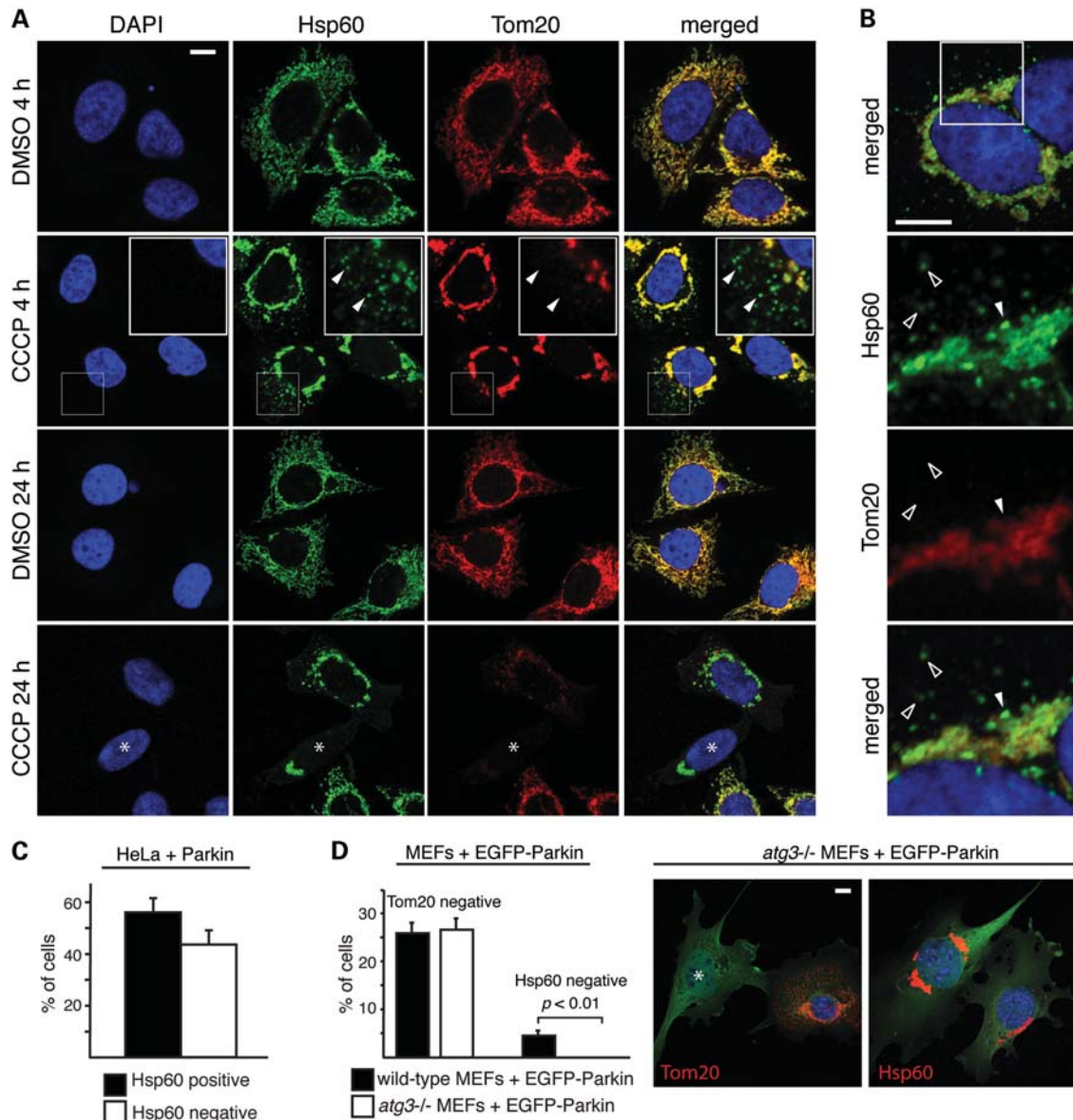


**Figure 4.** Degradation of Tom20 occurs prior to mitophagy and does not require the autophagy pathway. **(A)** Degradation of Tom20 induced by CCCP treatment. After 4 and 24 h of CCCP (20  $\mu$ M) or vehicle treatment, HeLa cells expressing Parkin were stained for Hsp60 (green), Tom20 (red) and nuclei (DAPI, blue). In the second row, the insets show enlarged views of the boxed area. Arrowheads mark examples of dispersed mitochondria that are positive for Hsp60 but negative for Tom20. In the fourth row, the asterisk indicates a cell with Tom20-negative/Hsp60-positive mitochondria. **(B)** Loss of Tom20 in both dispersed mitochondria and within patches of the mitochondrial aggregate. HeLa cells expressing Parkin were treated with CCCP for 4 h and stained for Hsp60 (green), Tom20 (red) and nuclei (DAPI, blue). The lower three panels correspond to the boxed area in the top panel. The filled arrowhead marks a patch in the perinuclear mitochondrial aggregate that is positive for Hsp60, but negative for Tom20. Unfilled arrowheads mark dispersed mitochondria that are Tom20 negative/Hsp60 positive. **(C)** Quantitation of the 24 h time point in (A). Cells that were Tom20 negative were scored for Hsp60 immunoreactivity. Error bars indicate standard deviations from three independent experiments; 100 cells were scored per experiment. **(D)** Tom20 degradation in Atg3-null MEFs. Wild-type and Atg3-null MEFs expressing EGFP-Parkin were treated with 20  $\mu$ M CCCP for 24 h and immunostained for Tom20 or Hsp60. Cells were scored for complete loss of Tom20 or Hsp60. Representative images of Atg3-null cells are shown on the right. The left image shows an example of a Tom20-negative cell (asterisk). No Hsp60-negative cells were ever found (right image). Error bars represent standard deviations from three independent experiments; 100 cells were analyzed per experiment. The *P*-value was calculated using the *t*-test. All scale bars are 10 microns.

perinuclear clustering and loss of Tom20 signal were Parkin-dependent, as these events do not occur in HeLa cells lacking Parkin (Supplementary Material, Fig. S3A).

Later time points showed an even more dramatic discrepancy between Tom20 and Hsp60 staining. After 24 h of CCCP treatment, ~20% of the cells showed complete loss of Tom20 immunostaining (Fig. 4A), consistent with previous

studies. Among these cells, ~40% have no detectable Hsp60 signal, whereas the other ~60% retained strong Hsp60 signals despite an obvious reduction in overall mitochondrial biomass (Fig. 4A and C). The above observations are not specific to Hsp60, as immunostaining against two independent matrix proteins, TRAP-1 (Supplementary Material, Fig. S3B) and F1 $\beta$  (Supplementary Material, Fig. S3C), revealed a

similar staining pattern. Previous studies have used the outer membrane protein Tom20 as a marker to monitor loss of mitochondria through Parkin-mediated mitophagy (6,8,9,13). Our observations indicate that, in some cases, the loss of Tom20 staining reflects Tom20 degradation by the UPS, rather than frank removal of the organelle. Our data therefore provide evidence that the Parkin-mediated proteolysis of outer membrane proteins precedes, and is distinct from, degradation of mitochondria via mitophagy.

We compared wild-type versus autophagy-deficient Atg3-null MEFs to further clarify the distinction between outer membrane protein degradation and mitophagy. After CCCP treatment, Parkin-expressing Atg3-null MEFs failed to undergo mitophagy (as indicated by preservation of Hsp60 staining) but still showed loss of Tom20 staining (Fig. 4D). These observations clearly demonstrate that degradation of mitochondrial outer membrane proteins, but not mitophagy, occurs independently of the autophagy machinery.

### The UPS is essential for Parkin-mediated mitophagy

When Parkin-expressing cells were treated with CCCP for 4 h, dispersed mitochondria at the cell periphery are Tom20 negative but Hsp60 positive (Figs 4A and B and 5B). Intriguingly, the autophagosome marker LC3B is selectively associated with these dispersed mitochondria (Fig. 5A). LC3B is present in ~90% of the dispersed mitochondria, but generally absent from the aggregated mitochondria. Treatment with the proteasome inhibitor MG132 prevented the formation of dispersed, Tom20 negative, mitochondria at 4 h after CCCP treatment (Fig. 5B), without affecting the recruitment of Parkin to mitochondria (Supplementary Material, Fig. S4A and B). Quantification showed that, in the absence of MG132, ~90% of CCCP-treated cells show 30 or more Tom20-negative mitochondria that are dispersed in the cell periphery (Fig. 5B). In contrast, >90% of MG132-treated cells show no dispersed, Tom20-negative mitochondria (Fig. 5B). Similar results were obtained with epoxomicin (Supplementary Material, Fig. S4C and D). To understand the dynamics of Tom20 loss, we performed additional immunostaining experiments at early time points after CCCP treatment. In the absence of epoxomicin treatment, some Tom20-negative mitochondria arise prior to the overt perinuclear aggregation of mitochondria (Supplementary Material, Fig. S3D). After aggregation of the mitochondria, Tom20-negative mitochondria continue to accumulate. The latter observation suggests that the 26S proteasome may facilitate dispersion of mitochondria from the perinuclear aggregate, and thereby their uptake by the autophagy machinery. In addition, however, it is clear that Tom20-negative mitochondria can also arise without first being part of the perinuclear mitochondrial aggregate.

Because Parkin-dependent proteolysis occurs prior to mitophagy, we asked whether this proteolysis is functionally coupled to mitophagy. When cells are treated with a 100 min pulse of CCCP and allowed to recover for 12 h, >90% of the cells show highly fragmented and dispersed mitochondria (Fig. 5C). By 24 h, ~30% of the cells show complete loss of mitochondria, reflecting a high level of mitophagy (Fig. 5D). Pretreatment of cells with MG132 or epoxomicin dramatically changed the cellular outcome of the CCCP

pulse. At 12 h, the cells showed an obvious preservation of mitochondria mass and tubular mitochondria, compared with cells without MG132 or epoxomicin (Fig. 5C and Supplementary Material, Fig. S4C and E). Most remarkably, at 24 h, all cells treated with MG132 or epoxomicin retained abundant mitochondria (Fig. 5D), indicating that the 26S proteasome is critical for Parkin-mediated mitophagy. Inhibition of the proteasome also blocked mitophagy in MEFs expressing Parkin (Supplementary Material, Fig. S4G). The degradation of mitochondria was reduced in HeLa cells overexpressing the K48R ubiquitin mutant (Supplementary Material, Fig. S2), consistent with the idea that K48-linked polyubiquitination is involved in Parkin-mediated mitophagy.

To determine whether these results apply to neuronal cells, we utilized the dopaminergic neuroblastoma cell line SH-SY5Y, which also undergoes CCCP-induced mitophagy upon expression of Parkin (6). As in HeLa cells, CCCP treatment of Parkin-expressing SH-SY5Y cells led to, at 4 h post-treatment, the appearance of peripheral mitochondria that were Tom20 negative but Hsp60 positive. Treatment with epoxomicin prevented the appearance of such Tom20-negative mitochondria (Fig. 5E and Supplementary Material, Fig. S4F). At 24 h post-CCCP treatment, epoxomicin also completely blocked mitophagy in the SH-SY5Y cells (Fig. 5F and Supplementary Material, Fig. S4F).

Because Mfn1 and Mfn2 are rapidly degraded downstream of Parkin in response to mitochondrial depolarization, we wondered whether inhibition of their degradation was responsible for the ability of proteasome inhibitors to block Parkin-mediated mitophagy. To address this issue, we tested whether epoxomicin could inhibit Parkin-mediated mitophagy in Mfn-null MEFs that lack both Mfn1 and Mfn2. We found that mitophagy in these cells, as in wild-type MEFs, was still completely blocked by epoxomicin (Fig. 6), indicating that degradation of proteins beyond Mfn1 and Mfn2 are essential for mitophagy caused by Parkin activation.

### DISCUSSION

Previous studies showed that, upon recruitment to dysfunctional mitochondria, Parkin predominantly mediates K63-linked polyubiquitination, which facilitates recruitment of the autophagic adaptor p62 (6,13,16–18). However, p62 appears to be involved in controlling mitochondrial distribution and is not essential for degradation of mitochondria (17,18). In addition to the enrichment of K63-linked polyubiquitination, our proteomics and biochemical experiments revealed significant enrichment of K48-linked polyubiquitination, which is the linkage-type that classically targets proteins for degradation via the UPS. Given the rapid degradation of K48-linked proteins, effective detection of this type of polyubiquitination requires sensitive methods such as mass spectrometry, unless degradation of K48-linked proteins is prevented by inhibition of the UPS. Thus, it is not surprising that the role of K48-polyubiquitination in Parkin-mediated mitophagy was previously underappreciated. Taken together, these results indicate a dual molecular function for the ubiquitin ligase activity of Parkin. Polyubiquitination of mitochondrial proteins is used as an interaction module to recruit the

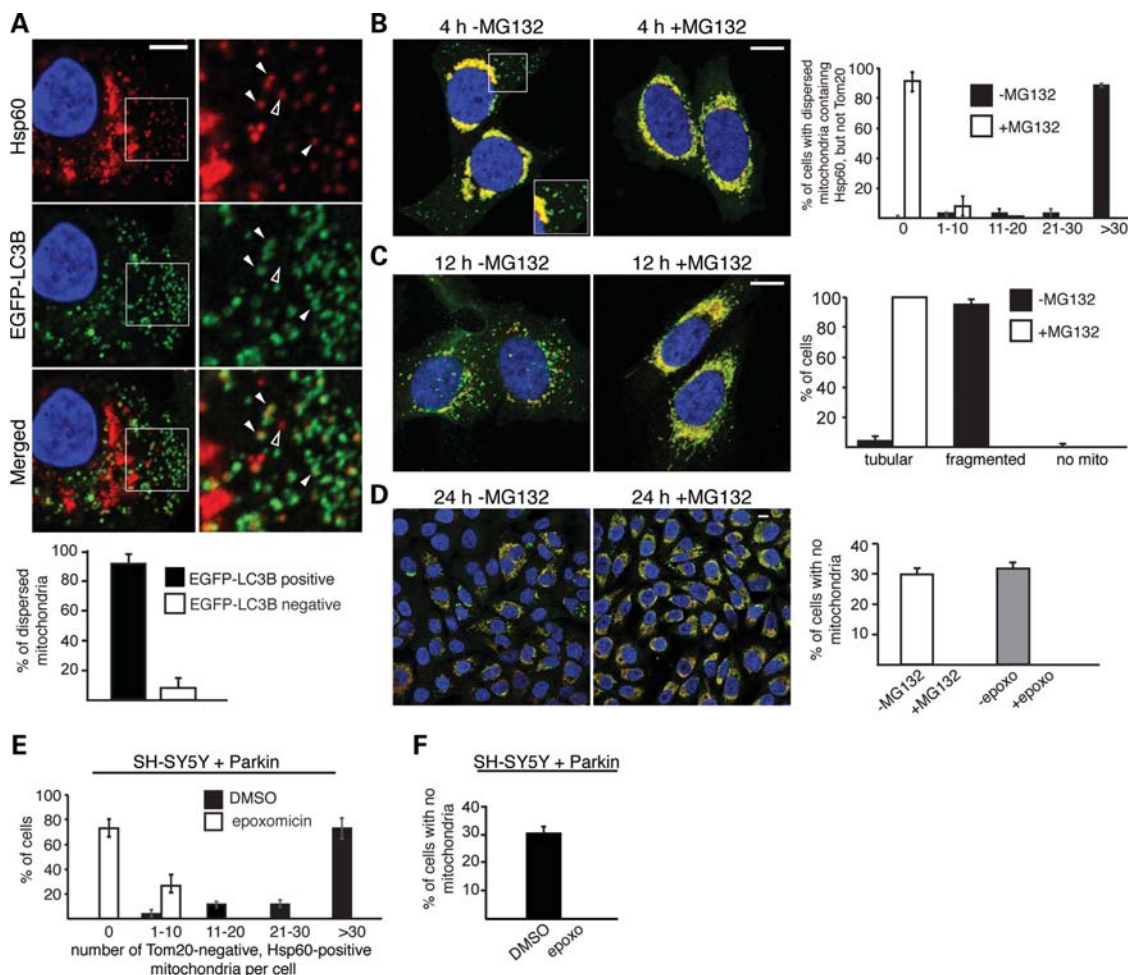


**Figure 5.** Activation of the ubiquitin–proteasome pathway is essential for mitophagy. (A) Co-localization of dispersed mitochondria and LC3B in CCCP-treated cells. HeLa cells expressing Parkin and EGFP-LC3B were treated with 100 nm baflomycin A1 and CCCP for 4 h, and stained for Hsp60 (red), EGFP-LC3B (green) and nuclei (DAPI, blue). Enlarged views of the boxed area are shown in the right column. Filled arrowheads mark examples of co-localization between dispersed mitochondria and EGFP-LC3B. The unfilled arrowhead marks an example of a dispersed mitochondrion that does not co-localize with EGFP-LC3B. Quantitation of this experiment is shown in the graph below. Error bars represent standard deviations from three independent experiments. Twenty cells were analyzed for each replicate, and ~2400 dispersed mitochondria were manually assessed in total. In (B)–(D), Parkin-expressing HeLa cells were treated with CCCP in the presence or absence of the proteasome inhibitor MG132 (10  $\mu$ M). Cells were immunostained for Hsp60 (green), Tom20 (red) and nuclei (DAPI, blue). (B) MG132 inhibits Tom20 loss after 4 h of persistent CCCP treatment. Inset shows an enlarged view of the boxed area, highlighting the presence of dispersed, Tom20-negative mitochondria when MG132 is not present. The graph on the right shows quantification of this experiment. Each cell was scored into one of the five indicated bins, depending on the number of dispersed mitochondria that are Tom20 negative, but Hsp60 positive. Error bars indicate standard deviations from three independent experiments; 100 cells were scored per experiment. (C) MG132 preserves mitochondrial morphology at 12 h after a 100 min pulse treatment with CCCP. The graph on the right shows quantification of mitochondrial morphology. Cells were scored as having tubular mitochondria, fragmented mitochondria or no mitochondria. Error bars indicate standard deviations from three independent experiments; 500 cells were scored per experiment. (D) MG132 or epoxomicin abrogates CCCP-induced mitophagy. The images show cells 24 h after a 100 min pulse treatment with CCCP in the presence or absence of MG132 (10  $\mu$ M). The graph on the right shows quantification of this experiment and a related one with epoxomicin (2  $\mu$ M). Cells without mitochondria were defined by the complete lack of both Tom20 and Hsp60 signal. Error bars indicate standard deviations from three independent experiments. 1000 cells were scored for each MG132 experiment, and 200 cells were scored for each epoxomicin experiments. Scale bars equal 10  $\mu$ m for (A)–(D). (E) Degradation of Tom20 in human neuroblastoma SH-SY5Y cells expressing exogenous Parkin. Cells were treated with DMSO (vehicle) or CCCP (20  $\mu$ M) for 4 h. Cells were scored into one of the indicated five bins, depending on the number of dispersed mitochondria lacking Tom20, as described for (B). Error bars indicate standard deviations in three independent experiments; 100 cells were scored per experiment. (F) Epoxomicin abrogates CCCP-induced mitophagy in SH-SY5Y cells expressing Parkin. Cells were treated as in (D) in the presence or absence of epoxomicin (2  $\mu$ M) and stained for Hsp60 and nuclei (DAPI). Cells without mitochondria were identified by complete loss of Hsp60 signal around the DAPI-stained nucleus. Error bars represent standard deviations from three independent experiments; 200 cells were analyzed per experiment.

autophagic machinery, as well as a signal for outer membrane protein degradation.

Several recent studies have focused on mitofusins as a degradation target of Parkin. In Drosophila, mitofusin (dmfn) is ubiquitinated and downregulated by Parkin (11,21). This relationship may underlie, in part, the strong

genetic interactions between mitochondrial fusion/fission and the Pink1/Parkin pathway (28–30). In mammals, Mfn1 and Mfn2 are polyubiquitinated (31) and degraded (32) in response to Parkin activation. These studies in mammalian and Drosophila cells suggest that degradation of mitofusins may serve to segregate dysfunctional

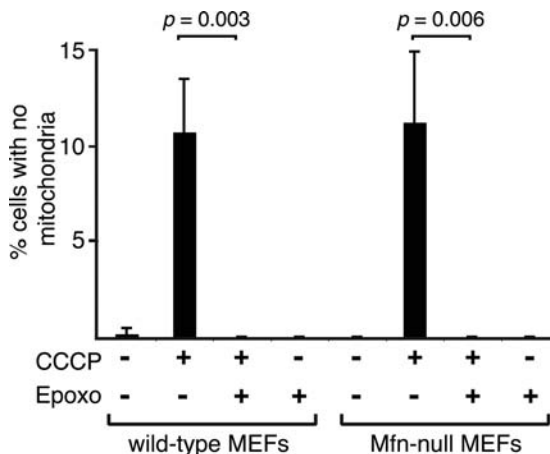


**Figure 6.** Parkin-mediated mitophagy in Mfn-null cells is blocked by the proteasome inhibitor epoxomicin. EGFP-Parkin was expressed in wild-type (WT) and Mfn1/Mfn2-null MEFs containing matrix-targeted TagRFP-T. Cultures were treated with the indicated drugs, and EGFP-positive cells were scored for the presence of mitochondria. Error bars indicate standard deviations from three experiments; 200 cells were scored per experiment. The *P*-values were calculated using the *t*-test.

mitochondria, thereby enhancing the functional benefits of mitophagy (32–34).

During preparation of this manuscript, it was reported that Parkin-mediated degradation of mitofusins is prevented by over-expression of dominant-negative p97 or the proteasome inhibitor MG132 (32). Inhibition of either p97 or the proteasome also blocks mitophagy, but it is unclear whether this effect is due to the prevention of mitofusin degradation (32). Given that inhibition of the proteasome inhibits mitophagy, it is important to characterize the role of the UPS in this pathway and to evaluate whether mitofusins are the critical degradation targets of Parkin. Our proteomics and cell biological experiments demonstrate robust recruitment of the 26S proteasome to mitochondria and enrichment of K48-linked polyubiquitin, thus supporting a direct role of the UPS in Parkin-mediated mitophagy. In addition to mitofusins, we identified a broad range of mitochondrial outer membrane proteins that are degraded in a Parkin- and UPS-dependent manner. Importantly, we find that Parkin-mediated mitophagy in Mfn1/Mfn2-null cells is still blocked by inhibition of the proteasome. Therefore, although degradation of mitofusins may indeed serve to segregate dysfunctional mitochondria, our results provide strong evidence that additional remodeling of the mitochondrial outer membrane proteome, involving widespread proteolysis, is necessary to promote mitophagy. As a technical point, we note that accurate assessment of mitophagy in future studies will require the use of a marker protein located in the mitochondrial matrix, and not an outer membrane protein such as the commonly used Tom20.

Further work will be necessary to understand mechanistically how the UPS facilitates mitophagy. Two general models, not mutually exclusive, can be proposed. First, removal of outer membrane proteins may facilitate engulfment of mitochondria by autophagosomes. We speculate that aggregation of depolarized mitochondria depends on outer membrane proteins, and that degradation of such proteins by the

UPS may help disperse mitochondria into small individual units so that they can be substrates for autophagy. This model is consistent with the broad degradation of outer membrane proteins by Parkin, and the observation that fragmentation of mitochondria is important for mitophagy (35). Alternatively, Parkin-mediated degradation may serve to remove one or more negative regulators of mitophagy on the mitochondrial surface, thereby triggering a signal for engulfment of a defective mitochondrion by an autophagosome.

By linking Parkin-mediated polyubiquitination to the UPS, our results support, in a general sense, earlier models postulating a role for Parkin in cellular protein quality control (14). In PD and other neurodegenerative disorders—including Alzheimer's, prion and polyglutamine diseases—defects in the UPS are thought to contribute to toxic accumulation of misfolded or aggregated proteins in the cytosol (14,36). Distinct from these earlier models, however, we show that for Parkin, the UPS operates within a separate cellular pathway involving mitochondrial quality control.

Our results provide evidence for the concept that the two major degradative pathways—the UPS and autophagy—are functionally linked (37). In future studies, it will be important to explore whether activation of the UPS is important for other forms of autophagy. In addition, although the UPS is clearly essential for Parkin-mediated mitophagy, it remains possible that activation of the UPS by Parkin has additional functions for mitochondria. Clarification of this issue will have important implications for the pathogenesis of PD.

## MATERIALS AND METHODS

### Cell culture and stable isotope labeling by amino acid in cell culture (SILAC)

Parkin-expressing cell lines were generated via lentivirus-mediated transduction of HeLa S3, HeLa cells and SH-SY5Y cells, followed by isolation of clones where indicated. Expression of Parkin is driven from the cytomegalovirus promoter. The wild-type and Atg3-null MEFs were kindly provided by Yu-Shin Sou and Masaaki Komatsu (27). Enhanced green fluorescent protein (EGFP)-tagged mouse Parkin was expressed in MEFs via retrovirus-mediated transduction, and EGFP-Parkin-expressing cells were selected by G418 (400 µg/ml). HeLa, HeLa S3 and MEF cell lines were cultured in Dulbecco's modified Eagle's medium (DMEM) containing 10% bovine serum (for HeLa and HeLa S3), or 10% fetal bovine serum supplemented with non-essential amino acids (for MEFs). For SILAC, DMEM lacking arginine and lysine was used, along with 10% dialyzed fetal bovine serum. For heavy labeling, Arg6 (U-13C6) and Lys8 (U-13C6, U-15N2) (Cambridge Isotopes) were supplemented at the same concentration as in the standard DMEM formulation. For light labeling, regular DMEM was used.

To dissipate the mitochondrial membrane potential, 20 µM carbonyl cyanide CCCP (Sigma) was used. For pulse treatments, cells were incubated in media with 20 µM CCCP for 100 min, followed by incubation in media without CCCP for the indicated time. For inhibition of the proteasome, cells were pretreated with 10 µM MG132 (Sigma), or 2 µM epoxomicin (Sigma) prior to treatment with CCCP.

## Isolation of mitochondria

For immunoblot analysis, mitochondria were isolated as previously described (20). For SILAC, mitochondria were isolated from a 1:1 mixture of heavy and light SILAC-labeled, Parkin-expressing HeLa S3 cells. Cells were lysed using a nitrogen bomb (Parr) at 200 psi for 10 min, followed by mechanical homogenization with a glass–glass dounce homogenizer. Crude mitochondria were purified by differential centrifugation and further purified by a discontinuous Percoll gradient consisting of 80, 52 and 21% Percoll.

## Isoelectric focusing of peptides

In-solution digested peptides (150 µg) were separated according to their isoelectric point with the Agilent 3100 OFFGEL fractionator (Agilent). The system was set up according to the manufacturers' guidelines (Agilent, 5969-1582), but strips were exchanged by 13 cm Immobiline™ DryStrip, pH 3–10 (GE Healthcare), and ampholytes were substituted by IPG buffer, pH 3–10 (GE Healthcare). Peptides were focused for 20 kilovolt hours at a maximum current of 50 µA, maximum voltage of 8000 V and maximum power of 200 mW into 12 fractions. Each peptide fraction was acidified by adding 1% trifluoroacetic acid, then desalted and concentrated on a reversed-phase C<sub>18</sub> StageTips (Proxeon Biosystems) utilizing a reported adaptation (38). StageTips were first washed with 80% acetonitrile: 0.5% acetic acid, then methanol, followed by 2% acetonitrile: 1% trifluoroacetic acid. Peptides were then loaded onto StageTips, washed with 0.5% acetic acid and eluted with 80% acetonitrile: 0.5% acetic acid.

## Mass spectrometric analysis

All mass spectrometry experiments were performed on an EASY-nLC connected to a hybrid LTQ–Orbitrap classic (Thermo Fisher Scientific) equipped with a nanoelectrospray ion source (Proxeon Biosystems) essentially as previously described (39) with some modifications. Peptides were separated on a 15 cm reversed-phase analytical column (75 µm internal diameter) in-house packed with 3 µm C<sub>18</sub> beads (ReproSil-Pur C18-AQ medium; Dr Maisch GmbH) with a 160 min gradient from 5 to 35% acetonitrile in 0.2% formic acid at a flow rate of 350 nl per minute. The mass spectrometer was operated in data-dependent mode to automatically switch between full-scan MS and tandem MS acquisition. Survey full scan mass spectra were acquired in the Orbitrap (300–1700 m/z), after accumulation of 500 000 ions, with a resolution of 60 000 at 400 m/z. The top 10 most intense ions from the survey scan were isolated and, after the accumulation of 5000 ions, fragmented in the linear ion trap by collisionally induced dissociation (collisional energy 35% and isolation width 2 Da). Precursor ion charge state screening was enabled and all singly charged and unassigned charge states were rejected. The dynamic exclusion list was set with a maximum retention time of 90 s, a relative mass window of 10 ppm and early expiration was enabled.

## Data analysis

Raw data files were analyzed by MaxQuant (v 1.0.13.13) (40) and searched against the IPI human database (v 3.54) with tryptic digestion, maximum of two missed cleavages, fixed carboxyamidomethyl modifications of cysteine, variable oxidation modifications of methionine and variable protein N-terminus acetylations with 1% false discovery rate thresholds for both peptides and proteins. At least two different peptide sequences were required for protein identification and two different ratio measurements were required for protein quantitation. Protein groups whose overall ratios were significantly different ( $P < 0.01$ ) and whose ratios in at least two out of three replicates were also significantly different ( $P < 0.05$ ) were considered to be significantly altered. Mitochondrial annotations were derived from MitoCarta (20) and mitochondrial outer membrane annotations were derived from Uniprot. Quantification of K48-linked and K63-linked polyubiquitin was performed by analysis of unique diglycine signature peptides associated with each modification (41).

## Fluorescence microscopy

All images were acquired using a Plan-Apochromat 63X/1.4 oil objective on a LSM 710 confocal microscope with Zen 2009 software (Carl Zeiss) and processed (to crop out irrelevant areas, brightness and contrast adjustment) using ImageJ software.

## Antibodies

The following commercially available antibodies were used: anti-actin (Mab1501R, Millipore), anti-Bak (Y164, Abcam), anti-cytochrome *c* (Mitosciences), anti-F<sub>1</sub>β (Mitosciences), anti-Fis1 (Alexis), anti-Hsp60 (SC-1052, Santa Cruz Biotech), anti-Mfn2 (Sigma), anti-Parkin (PRK8, Cell Signaling), anti-Parkin (Abcam), anti-Psma2 (BioMol), anti-Psmb5 (Abcam), anti-Sod2 (Abcam), anti-Tom20 (FL-145, Santa Cruz), anti-Tom70 (Novus Biologicals), anti-TRAP-1 (Abcam), anti-ubiquitin (Enzo), anti-K48-polyubiquitin (Cell Signaling), anti-K63-polyubiquitin (Enzo) and anti-VDAC (Molecular Probes). The following antibodies were raised in-house: anti-Opa1 monoclonal 1E8 and anti-Mfn1 (42).

## SUPPLEMENTARY MATERIAL

Supplementary Material is available at *HMG* online.

## ACKNOWLEDGEMENTS

We thank Ray Deshaies and the Chan lab for critical discussions and reading of the manuscript. We are grateful to Drs Yu-Shin Sou and Masaaki Komatsu for providing the Atg3-null MEFs, and to Willem den Besten and Ray Deshaies for providing ubiquitin plasmids.

*Conflict of Interest statement:* None declared.

## FUNDING

This work was supported by the National Institute of Health (GM062967) and the Thomas Hartman Foundation for Parkinson's Research. Funding to pay the Open Access publication charges for this article was provided by the Howard Hughes Medical Institute.

## REFERENCES

- Clark, I.E., Dodson, M.W., Jiang, C., Cao, J.H., Huh, J.R., Seol, J.H., Yoo, S.J., Hay, B.A. and Guo, M. (2006) Drosophila pink1 is required for mitochondrial function and interacts genetically with parkin. *Nature*, **441**, 1162–1166.
- Greene, J.C., Whitworth, A.J., Kuo, I., Andrews, L.A., Feany, M.B. and Pallanck, L.J. (2003) Mitochondrial pathology and apoptotic muscle degeneration in Drosophila parkin mutants. *Proc. Natl Acad. Sci. USA*, **100**, 4078–4083.
- Palacino, J.J., Sagi, D., Goldberg, M.S., Krauss, S., Motz, C., Wacker, M., Klose, J. and Shen, J. (2004) Mitochondrial dysfunction and oxidative damage in parkin-deficient mice. *J. Biol. Chem.*, **279**, 18614–18622.
- Park, J., Lee, S.B., Lee, S., Kim, Y., Song, S., Kim, S., Bae, E., Kim, J., Shong, M., Kim, J.M. et al. (2006) Mitochondrial dysfunction in Drosophila PINK1 mutants is complemented by parkin. *Nature*, **441**, 1157–1161.
- Gautier, C.A., Kitada, T. and Shen, J. (2008) Loss of PINK1 causes mitochondrial functional defects and increased sensitivity to oxidative stress. *Proc. Natl Acad. Sci. USA*, **105**, 11364–11369.
- Geisler, S., Holmstrom, K.M., Skujat, D., Fiesel, F.C., Rothfuss, O.C., Kahle, P.J. and Springer, W. (2010) PINK1/Parkin-mediated mitophagy is dependent on VDAC1 and p62/SQSTM1. *Nat. Cell Biol.*, **12**, 119–131.
- Matsuda, N., Sato, S., Shiba, K., Okatsu, K., Saisho, K., Gautier, C.A., Sou, Y.S., Saiki, S., Kawajiri, S., Sato, F. et al. (2010) PINK1 stabilized by mitochondrial depolarization recruits Parkin to damaged mitochondria and activates latent Parkin for mitophagy. *J. Cell Biol.*, **189**, 211–221.
- Narendra, D., Tanaka, A., Suen, D.F. and Youle, R.J. (2008) Parkin is recruited selectively to impaired mitochondria and promotes their autophagy. *J. Cell Biol.*, **183**, 795–803.
- Narendra, D.P., Jin, S.M., Tanaka, A., Suen, D.F., Gautier, C.A., Shen, J., Cookson, M.R. and Youle, R.J. (2010) PINK1 is selectively stabilized on impaired mitochondria to activate Parkin. *PLoS Biol.*, **8**, e1000298.
- Vives-Bauza, C., Zhou, C., Huang, Y., Cui, M., de Vries, R.L., Kim, J., May, J., Tocilescu, M.A., Liu, W., Ko, H.S. et al. (2010) PINK1-dependent recruitment of Parkin to mitochondria in mitophagy. *Proc. Natl Acad. Sci. USA*, **107**, 378–383.
- Ziviani, E., Tao, R.N. and Whitworth, A.J. (2010) Drosophila parkin requires PINK1 for mitochondrial translocation and ubiquitinates mitofusin. *Proc. Natl Acad. Sci. USA*, **107**, 5018–5023.
- Shimura, H., Hattori, N., Kubo, S., Mizuno, Y., Asakawa, S., Minoshima, S., Shimizu, N., Iwai, K., Chiba, T., Tanaka, K. et al. (2000) Familial Parkinson disease gene product, parkin, is a ubiquitin-protein ligase. *Nat. Genet.*, **25**, 302–305.
- Lee, J.Y., Nagano, Y., Taylor, J.P., Lim, K.L. and Yao, T.P. (2010) Disease-causing mutations in parkin impair mitochondrial ubiquitination, aggregation, and HDAC6-dependent mitophagy. *J. Cell Biol.*, **189**, 671–679.
- Ciechanover, A. and Brundin, P. (2003) The ubiquitin proteasome system in neurodegenerative diseases: sometimes the chicken, sometimes the egg. *Neuron*, **40**, 427–446.
- Deshais, R.J. and Joazeiro, C.A. (2009) RING domain E3 ubiquitin ligases. *Annu. Rev. Biochem.*, **78**, 399–434.
- Ding, W.X., Ni, H.M., Li, M., Liao, Y., Chen, X., Stoltz, D.B., Dorn II, G.W. and Yin, X.M. (2010) Nix is critical to two distinct phases of mitophagy: reactive oxygen species (ROS)-mediated autophagy induction and Parkin-ubiquitin-p62-mediated mitochondria priming. *J. Biol. Chem.*, **285**, 27879–27890.
- Okatsu, K., Saisho, K., Shimanuki, M., Nakada, K., Shitara, H., Sou, Y.S., Kimura, M., Sato, S., Hattori, N., Komatsu, M. et al. (2010) p62/SQSTM1 cooperates with Parkin for perinuclear clustering of depolarized mitochondria. *Genes Cells*, **15**, 887–900.
- Narendra, D.P., Kane, L.A., Hauser, D.N., Fearnley, I.M. and Youle, R.J. (2010) p62/SQSTM1 is required for Parkin-induced mitochondrial clustering but not mitophagy; VDAC1 is dispensable for both. *Autophagy*, **6**, 1090–1106.
- Ong, S.E., Blagoev, B., Kratchmarova, I., Kristensen, D.B., Steen, H., Pandey, A. and Mann, M. (2002) Stable isotope labeling by amino acids in cell culture, SILAC, as a simple and accurate approach to expression proteomics. *Mol. Cell. Proteomics*, **1**, 376–386.
- Pagliarini, D.J., Calvo, S.E., Chang, B., Sheth, S.A., Vafai, S.B., Ong, S.E., Walford, G.A., Sugiana, C., Boneh, A., Chen, W.K. et al. (2008) A mitochondrial protein compendium elucidates complex I disease biology. *Cell*, **134**, 112–123.
- Poole, A.C., Thomas, R.E., Yu, S., Vincow, E.S. and Pallanck, L. (2010) The mitochondrial fusion-promoting factor mitofusin is a substrate of the PINK1/parkin pathway. *PLoS ONE*, **5**, e10054.
- Song, Z., Chen, H., Fiket, M., Alexander, C. and Chan, D.C. (2007) OPA1 processing controls mitochondrial fusion and is regulated by mRNA splicing, membrane potential, and Yme1L. *J. Cell Biol.*, **178**, 749–755.
- Griparic, L., Kanazawa, T. and van der Bliek, A.M. (2007) Regulation of the mitochondrial dynamin-like protein Opal by proteolytic cleavage. *J. Cell Biol.*, **178**, 757–764.
- Narendra, D., Tanaka, A., Suen, D.F. and Youle, R.J. (2009) Parkin-induced mitophagy in the pathogenesis of Parkinson disease. *Autophagy*, **5**, 706–708.
- Kuroda, Y., Mitsui, T., Kunishige, M., Shono, M., Akaike, M., Azuma, H. and Matsumoto, T. (2006) Parkin enhances mitochondrial biogenesis in proliferating cells. *Hum. Mol. Genet.*, **15**, 883–895.
- Yao, D., Gu, Z., Nakamura, T., Shi, Z.Q., Ma, Y., Gaston, B., Palmer, L.A., Rockenstein, E.M., Zhang, Z., Masliah, E. et al. (2004) Nitrosative stress linked to sporadic Parkinson's disease: S-nitrosylation of parkin regulates its E3 ubiquitin ligase activity. *Proc. Natl Acad. Sci. USA*, **101**, 10810–10814.
- Sou, Y.S., Waguri, S., Iwata, J., Ueno, T., Fujimura, T., Hara, T., Sawada, N., Yamada, A., Mizushima, N., Uchiyama, Y. et al. (2008) The Atg8 conjugation system is indispensable for proper development of autophagic isolation membranes in mice. *Mol. Biol. Cell*, **19**, 4762–4775.
- Deng, H., Dodson, M.W., Huang, H. and Guo, M. (2008) The Parkinson's disease genes pink1 and parkin promote mitochondrial fission and/or inhibit fusion in Drosophila. *Proc. Natl Acad. Sci. USA*, **105**, 14503–14508.
- Poole, A.C., Thomas, R.E., Andrews, L.A., McBride, H.M., Whitworth, A.J. and Pallanck, L.J. (2008) The PINK1/Parkin pathway regulates mitochondrial morphology. *Proc. Natl Acad. Sci. USA*, **105**, 1638–1643.
- Yang, Y., Ouyang, Y., Yang, L., Beal, M.F., McQuibban, A., Vogel, H. and Lu, B. (2008) Pink1 regulates mitochondrial dynamics through interaction with the fission/fusion machinery. *Proc. Natl Acad. Sci. USA*, **105**, 7070–7075.
- Gegg, M.E., Cooper, J.M., Chau, K.Y., Rojo, M., Schapira, A.H. and Taunman, J.W. (2010) Mitofusin 1 and mitofusin 2 are ubiquitinated in a PINK1/parkin-dependent manner upon induction of mitophagy. *Hum. Mol. Genet.*, **19**, 4861–4870.
- Tanaka, A., Cleland, M.M., Xu, S., Narendra, D.P., Suen, D.F., Karbowski, M. and Youle, R.J. (2010) Proteasome and p97 mediate mitophagy and degradation of mitofusins induced by Parkin. *J. Cell Biol.*, **191**, 1367–1380.
- Ziviani, E. and Whitworth, A.J. (2010) How could Parkin-mediated ubiquitination of mitofusin promote mitophagy? *Autophagy*, **6**, 660–662.
- Pallanck, L.J. (2010) Culling sick mitochondria from the herd. *J. Cell Biol.*, **191**, 1225–1227.
- Twig, G., Elorza, A., Molina, A.J., Mohamed, H., Wikstrom, J.D., Walzer, G., Stiles, L., Haigh, S.E., Katz, S., Las, G. et al. (2008) Fission and selective fusion govern mitochondrial segregation and elimination by autophagy. *EMBO J.*, **27**, 433–446.
- Tai, H.C. and Schuman, E.M. (2008) Ubiquitin, the proteasome and protein degradation in neuronal function and dysfunction. *Nat. Rev. Neurosci.*, **9**, 826–838.

37. Korolchuk, V.I., Mansilla, A., Menzies, F.M. and Rubinsztein, D.C. (2009) Autophagy inhibition compromises degradation of ubiquitin-proteasome pathway substrates. *Mol. Cell.*, **33**, 517–527.
38. Rappaport, J., Ishihama, Y. and Mann, M. (2003) Stop and go extraction tips for matrix-assisted laser desorption/ionization, nanoelectrospray, and LC/MS sample pretreatment in proteomics. *Anal. Chem.*, **75**, 663–670.
39. de Godoy, L.M.F., Olsen, J.V., Cox, J., Nielsen, M.L., Hubner, N.C., Frohlich, F., Walther, T.C. and Mann, M. (2008) Comprehensive mass-spectrometry-based proteome quantification of haploid versus diploid yeast. *Nature*, **455**, 1251–1254.
40. Cox, J. and Mann, M. (2008) MaxQuant enables high peptide identification rates, individualized p.p.b.-range mass accuracies and proteome-wide protein quantification. *Nat. Biotechnol.*, **26**, 1367–1372.
41. Kirkpatrick, D.S., Hathaway, N.A., Hanna, J., Elsasser, S., Rush, J., Finley, D., King, R.W. and Gygi, S.P. (2006) Quantitative analysis of in vitro ubiquitinated cyclin B1 reveals complex chain topology. *Nat. Cell Biol.*, **8**, 700–710.
42. Chen, H., Detmer, S.A., Ewald, A.J., Griffin, E.E., Fraser, S.E. and Chan, D.C. (2003) Mitofusins Mfn1 and Mfn2 coordinately regulate mitochondrial fusion and are essential for embryonic development. *J. Cell Biol.*, **160**, 189–200.

# Postsynaptic Decoding of Neural Activity: eEF2 as a Biochemical Sensor Coupling Miniature Synaptic Transmission to Local Protein Synthesis

Michael A. Sutton,<sup>1,3</sup> Anne M. Taylor,<sup>1</sup> Hiroshi T. Ito,<sup>1</sup> Anh Pham,<sup>1</sup> and Erin M. Schuman<sup>1,2,\*</sup>

<sup>1</sup> Division of Biology 114-96

<sup>2</sup> Howard Hughes Medical Institute

California Institute of Technology, Pasadena, CA 91125, USA

<sup>3</sup> Present address: Molecular and Behavioral Neuroscience Institute and Department of Molecular and Integrative Physiology, 5067 BSRB, University of Michigan, Ann Arbor, MI 48109-2200, USA.

\*Correspondence: schumane@its.caltech.edu

DOI 10.1016/j.neuron.2007.07.030

## SUMMARY

Activity-dependent regulation of dendritic protein synthesis is critical for enduring changes in synaptic function, but how the unique features of distinct activity patterns are decoded by the dendritic translation machinery remains poorly understood. Here, we identify eukaryotic elongation factor-2 (eEF2), which catalyzes ribosomal translocation during protein synthesis, as a biochemical sensor in dendrites that is specifically and locally tuned to the quality of neurotransmission. We show that intrinsic action potential (AP)-mediated network activity in cultured hippocampal neurons maintains eEF2 in a relatively dephosphorylated (active) state, whereas spontaneous neurotransmitter release (i.e., miniature neurotransmission) strongly promotes the phosphorylation (and inactivation) of eEF2. The regulation of eEF2 phosphorylation is responsive to bidirectional changes in miniature neurotransmission and is controlled locally in dendrites. Finally, direct spatially controlled inhibition of eEF2 phosphorylation induces local translational activation, suggesting that eEF2 is a biochemical sensor that couples miniature synaptic events to local translational suppression in neuronal dendrites.

## INTRODUCTION

Recent work has implicated local dendritic protein synthesis in many enduring forms of synaptic plasticity, such as long-term potentiation and long-term depression (e.g., Kang and Schuman, 1996; Huber et al., 2000; Bradshaw et al., 2003), although the means by which synaptic activity is coupled to the protein synthetic machinery in dendrites remains poorly understood. The fact that these

forms of synaptic modification require different patterns of synaptic activity for their induction raises the question of how the local translational machinery decodes these unique activity patterns. Here, we explore this issue in the context of endogenous levels of two qualitatively distinct forms of synaptic transmission: (1) action potential (AP)-triggered release of neurotransmitter and (2) miniature synaptic transmission (minis) mediated by spontaneous, AP-independent neurotransmitter release (Fatt and Katz, 1952). Previous results have shown that these two forms of neurotransmission regulate local translation in opposite directions—blocking APs alone inhibits, whereas blocking both APs and minis stimulates, dendritic protein synthesis (Sutton et al., 2004, 2006). These observations suggest that neuronal dendrites possess a biochemical sensor that is specifically tuned to miniature synaptic transmission and capable of engaging the dendritic translation machinery.

In principle, this sensor could be represented by a general signaling pathway that is broadly coupled to protein translation, or alternatively, it could be a signal that is dedicated to the regulation of protein translation machinery itself. One candidate in the latter category is eukaryotic elongation factor-2 (eEF2) and its associated kinase, Ca<sup>2+</sup>/calmodulin-dependent protein kinase III (CaMKIII; Nairn and Palfrey, 1987), now known as eEF2 kinase. eEF2 catalyzes ribosomal translocation during polypeptide elongation. Phosphorylation of eEF2 at Thr56 strongly inhibits its activity, thereby inhibiting protein synthesis (Ryazanov et al., 1988; Redpath et al., 1993). In addition, eEF2 phosphorylation is known to be stimulated by strong activation of ionotropic glutamate receptors (GluRs; Marin et al., 1997; Scheetz et al., 2000; Chotiner et al., 2003) and can be regulated in isolated synaptic biochemical fractions (Scheetz et al., 2000; Carroll et al., 2004). These findings raise the possibility that eEF2 phosphorylation might serve to couple particular patterns of synaptic input to local translational suppression in neuronal dendrites.

Here, we demonstrate that eEF2 is a biochemical sensor tuned to ongoing levels of miniature synaptic transmission in hippocampal neurons. Similar to the regulation of dendritic protein synthesis, basal AP-dependent

and miniature transmission regulate eEF2 phosphorylation in opposite directions, with miniature events positively associated with the amount of eEF2 that is in its phosphorylated (translationally inactive) state. The regulation of eEF2 phosphorylation by miniature transmission is bidirectional—blocking minis markedly reduces, whereas enhancing minis stimulates, eEF2 phosphorylation. Moreover, miniature events regulate eEF2 locally in dendrites, and this regulation in turn inhibits dendritic translation in a spatially specific fashion. Taken together, our results suggest that eEF2 is a local sensor of miniature synaptic activity in dendrites that serves to couple this form of neurotransmission to local translational suppression.

## RESULTS

### Miniature Synaptic Events Inhibit Dendritic Protein Synthesis Locally

Previous work has shown that AP-dependent and miniature synaptic transmission regulate dendritic protein synthesis in opposite directions—blocking APs with tetrodotoxin (TTX) inhibits dendritic translation, whereas blocking miniature events stimulates dendritic protein synthesis (Sutton et al., 2004, 2006). Bath application of TTX, however, blocks both presynaptic and postsynaptic APs. To confine the effects of TTX to presynaptic neurons, we used a microfluidic chamber (Taylor et al., 2005) in which presynaptic or postsynaptic neurons can be fluidically isolated (Figures 1A and 1B). Application of TTX to the presynaptic compartment blocked spiking of presynaptic neurons but did not prevent postsynaptic neurons from spiking (Figure 1C). We then followed the presynaptic TTX application with postsynaptic APV to examine the effects of blocking the NMDA receptor (NMDAR)-mediated component of miniature neurotransmission on dendritic protein synthesis. Time-lapse imaging of dendrites expressing a fluorescent translation reporter (Figure 1D; Aakalu et al., 2001) revealed that, whereas control dendrites treated with TTX alone exhibited a small decline in fluorescence over time, inhibition of NMDAR minis resulted in an increase in dendritic protein synthesis (Figures 1E and 1F). These results indicate that the translational activation accompanying mini blockade is evident during selective elimination of presynaptic APs.

To examine the spatial specificity of this translational regulation, we used a dual micropipette delivery system to locally perfuse different dendritic regions of conventionally cultured neurons expressing the dendritic protein synthesis reporter. Pyramidal-like hippocampal neurons in culture were perfused continuously in HEPES-buffered saline (HBS) containing TTX (1 μM) to block all AP-induced evoked neurotransmission. After a baseline image series was taken, dendritic segments were locally perfused with TTX plus a cocktail of GluR antagonists (the AMPA receptor [AMPAR] antagonist, CNQX [40 μM] and the NMDAR antagonist APV [60 μM]), and changes in the rate of reporter synthesis over time were monitored. A fluorescent dye (Alexa 568) was included in the delivery

perfusate to monitor the perfusion area throughout the experiment. We compared changes in reporter expression in the treated dendritic segment with those of other segments of the same dendrite outside the perfused area both prior to and following local perfusion. As shown in Figures 2A–2D, we found that the change in reporter expression in the treated area was initially comparable with that of other segments of the same dendrite (at t = 0 min), but following local mini blockade, perfused areas demonstrated a progressive increase in reporter expression over the next 100 min (Figures 2B–2D). Restricted perfusion of vehicle alone (Figures 2E and 2F) was ineffective in altering local reporter synthesis, and the stimulation of local protein synthesis by mini blockade was completely prevented by bath application of the protein synthesis inhibitor anisomycin (40 μM; Figure 2F). These results indicate that local blockade of excitatory miniature neurotransmission enhances dendritic protein synthesis in a spatially specific fashion.

### eEF2: A Biochemical Sensor Uniquely Regulated by Miniature Neurotransmission

How do postsynaptic neurons distinguish minis from AP-driven input, and how is this distinction conveyed to the translation machinery in dendrites? To begin to address this question, we first examined the regulation of two signaling pathways strongly linked to translational control in most eukaryotic systems: the ERK-MAPK and PI3 kinase pathways (for reviews, see Holland, 2004; Ruggero and Sonenberg, 2005). We measured the phosphorylation status of ERK isoforms and Akt, a well-known downstream target of the PI3 kinase pathway, under conditions of AP block alone (with TTX) or block of both APs and excitatory miniature neurotransmission (TTX+CNQX+APV). Whereas the phosphorylation of Akt was unaltered by either manipulation, the phosphorylation (and presumably activity) of both ERK isoforms (p42 and p44) exhibited strong activity sensitivity: phosphorylation was depressed by AP blockade (Figure 3A) and exhibited an even stronger depression when minis were also blocked. These results identify the ERK-MAPK signaling pathway as a system that is highly sensitive to levels of postsynaptic activity, but it does not appear differentially responsive to evoked and spontaneous neurotransmission.

We next examined if posttranslational regulation of eEF2 accompanies mini blockade. eEF2 catalyzes ribosomal translocation during polypeptide elongation, and phosphorylation of eEF2 near the N terminus (at Thr56) is known to strongly inhibit its activity in the elongation phase of protein synthesis (Ryazanov et al., 1988; Redpath et al., 1993). We found that unlike ERK phosphorylation, the regulation of eEF2 phosphorylation by AP-dependent and miniature neurotransmission was both qualitatively and quantitatively distinct. Relative to control, AP blockade alone induced significantly greater phosphorylation of eEF2 at Thr56, whereas additional blockade of miniature transmission produced significantly diminished levels of eEF2 phosphorylated at that site

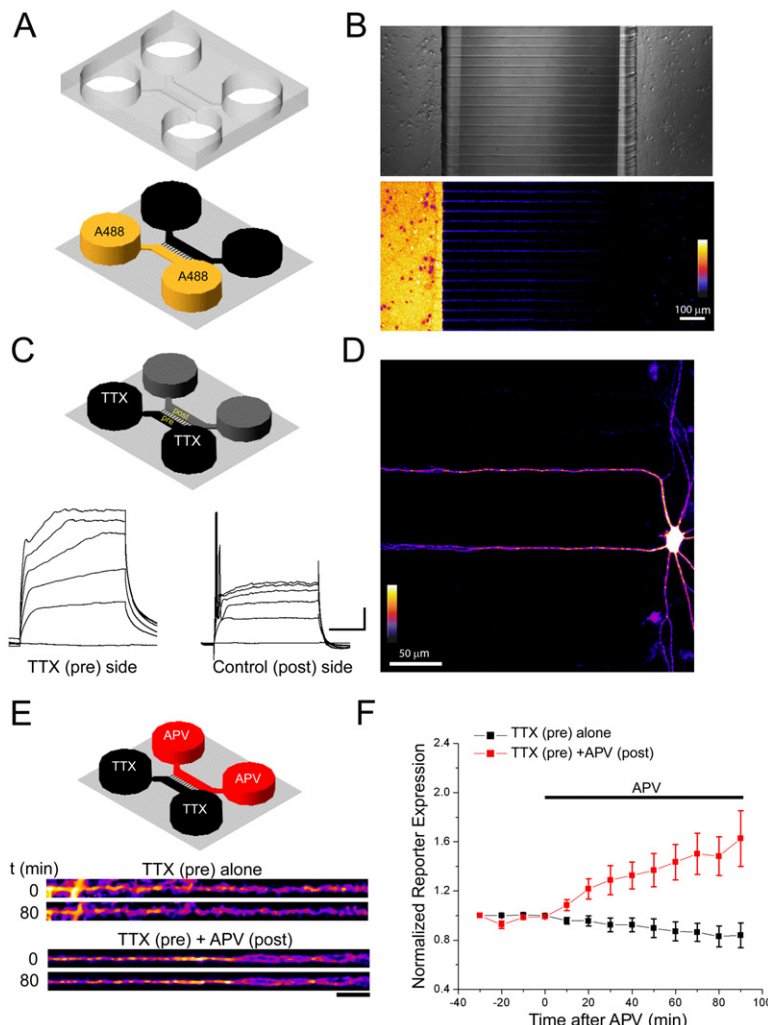


**Figure 1. Selective Blockade of Presynaptic APs with Postsynaptic Block of NMDAR Minis Leads to an Enhancement of Dendritic Protein Synthesis**

(A) Schematic of microfluidic culture chamber containing two (one “presynaptic” and one “postsynaptic”) somatic compartments connected by microgrooves. A volume difference between the somatic compartments ( $\sim 50 \mu\text{l}$ ) established a pressure difference between them, allowing each chemical microenvironment to be isolated for several hours.

(B) DIC image of a microfluidic chamber; cell bodies are evident in both somatic compartments and axons and dendrites can be observed in the microgrooves. Addition of Alexa Fluor 488 (MW 570) to the presynaptic cell body compartment shows that the dye only extends partially into the proximal grooves and negligibly affects the dendritic or somatic region at the other end of the chamber after 3 hr of isolation. Alexa 488 fluorescence intensity is indicated by the color look-up table.

(C) TTX was added to the presynaptic somatic compartment. After 60 min, current-clamp recordings were obtained from cell bodies in either presynaptic or postsynaptic compartments. TTX addition blocked spiking in presynaptic neurons in response to current injection, but did not block spiking of postsynaptic neurons. Scale bar, 10mV, 100 ms. These data indicate that TTX acts selectively on presynaptic neurons in this experiment.

(D) Example of a neuron expressing the GFP translation reporter in the postsynaptic compartment. Dendrites extend into microgrooves where they come into contact with axons (not visible here); fluorescence intensity (reporter expression) is indicated by the color look-up table.

(E) Design of experiment. TTX ( $5 \mu\text{M}$ ) (see Experimental Procedures) was added to the

presynaptic compartment to block APs; 1–1.5 hr later, baseline images were taken every 10 min, then APV ( $250 \mu\text{M}$ ) (see Experimental Procedures) was added to the postsynaptic compartment. In control experiments, TTX was isolated to the presynaptic compartment for the baseline images, then buffer (instead of APV) was added to the postsynaptic somatic side. Fluorescence images of dendrites expressing the GFP translation reporter were obtained before ( $t = 0$  min) and after ( $t = 80$  min) the addition of APV to block the NMDAR component of miniature excitatory synaptic events; fluorescence intensity as in (D). Scale bar,  $20 \mu\text{m}$ . Inhibition of NMDAR minis led to an enhancement of dendritic translation, as compared with control (TTX alone)-treated dendrites.

(F) Ensemble average of all control (TTX alone,  $n = 3$  experiments, five dendrites) and NMDAR mini block (TTX pre + APV post,  $n = 4$  experiments, eight dendrites) experiments. Inhibition of NMDAR minis led to a significant and rapid enhancement of dendritic protein synthesis.

(Figure 3A). Total levels of eEF2 protein were not different between the groups, suggesting that minis regulate eEF2 phosphorylation posttranslationally. These results indicate that eEF2 phosphorylation is differentially tuned to AP-dependent and miniature synaptic transmission, and the direction of the changes are consistent with eEF2 playing a causal role in the local translational suppression mediated by excitatory miniature events.

#### Bidirectional Regulation of eEF2 Phosphorylation by Miniature Synaptic Transmission

If eEF2 is a sensor of miniature neurotransmission, then an increase in Thr56 phosphorylation should occur when

miniature transmission is enhanced. To address this question, we used  $\alpha$ -latrotoxin ( $\alpha$ -LTX), which is known to stimulate the release of predocked synaptic vesicles from presynaptic terminals (e.g., Ceccarelli et al., 1973). In whole-cell voltage-clamp recordings ( $n = 8$ ), we confirmed that a low concentration of  $\alpha$ -LTX ( $100 \text{ pM}$ ; in combination with  $0.1 \text{ mM} \text{LaCl}_3$  to prevent formation of  $\alpha$ -LTX pores; Ashton et al., 2001) stimulates miniature release by approximately 1.5- to 2-fold (Figure 3B1; see also Sutton et al., 2004). We thus examined whether augmenting miniature neurotransmission enhances eEF2 phosphorylation during AP blockade. As shown in Figure 3B, treatment with TTX alone enhanced eEF2 phosphorylation

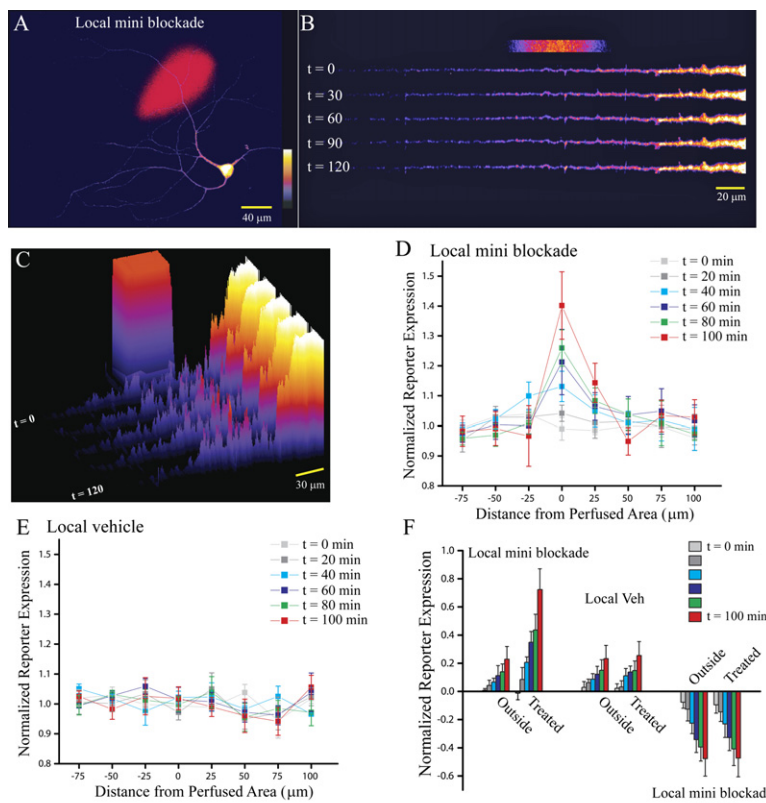


**Figure 2. Blockade of Excitatory Minis Induces Local Translation in Dendrites**

Example and summary of local perfusion experiments in cultured hippocampal neurons (>21 DIV) expressing a GFP-based fluorescent translation reporter (Aakalu et al., 2001). Neurons were globally treated with TTX (1  $\mu$ M, bath applied) to block AP-dependent neurotransmission prior to spatially restricted perfusion of either a mini-blocking cocktail (the AMPAR antagonist CNQX [40  $\mu$ M] plus the NMDAR antagonist APV [60  $\mu$ M]; n = 10 dendrites from six cells) or vehicle as a control (n = 8 dendrites from four cells). In an additional set of experiments, local mini blockade was examined with protein synthesis blocked by bath application of anisomycin (40  $\mu$ M; n = 10 dendrites from five cells).

(A–C) Example of an experiment in which prior bath application of TTX was followed by local perfusion of a mini-blocking cocktail for 120 min. (A) Shown is a neuron expressing the protein synthesis reporter, with superimposed perfusion area demarcated by Alexa 568 (present in the local perfusate in all experiments) fluorescence in red. (B) A time-lapse montage of the dendrite (straightened) from the cell shown in (A) from initiating local perfusion to 120 min later, at 30 min intervals; the perfusion area is marked in red above the dendrites. (C) 3D plot of fluorescence intensity in the same dendrite from t = 0–120 min, at 30 min intervals; relative fluorescence intensity (reporter increase in dendritic reporter expression in the

expression) is indicated by the color and height of the pixels. A spatially specific and progressive increase in reporter expression in the treated area (indicated by color tower above t = 0) was evident after local disruption of miniature synaptic transmission.

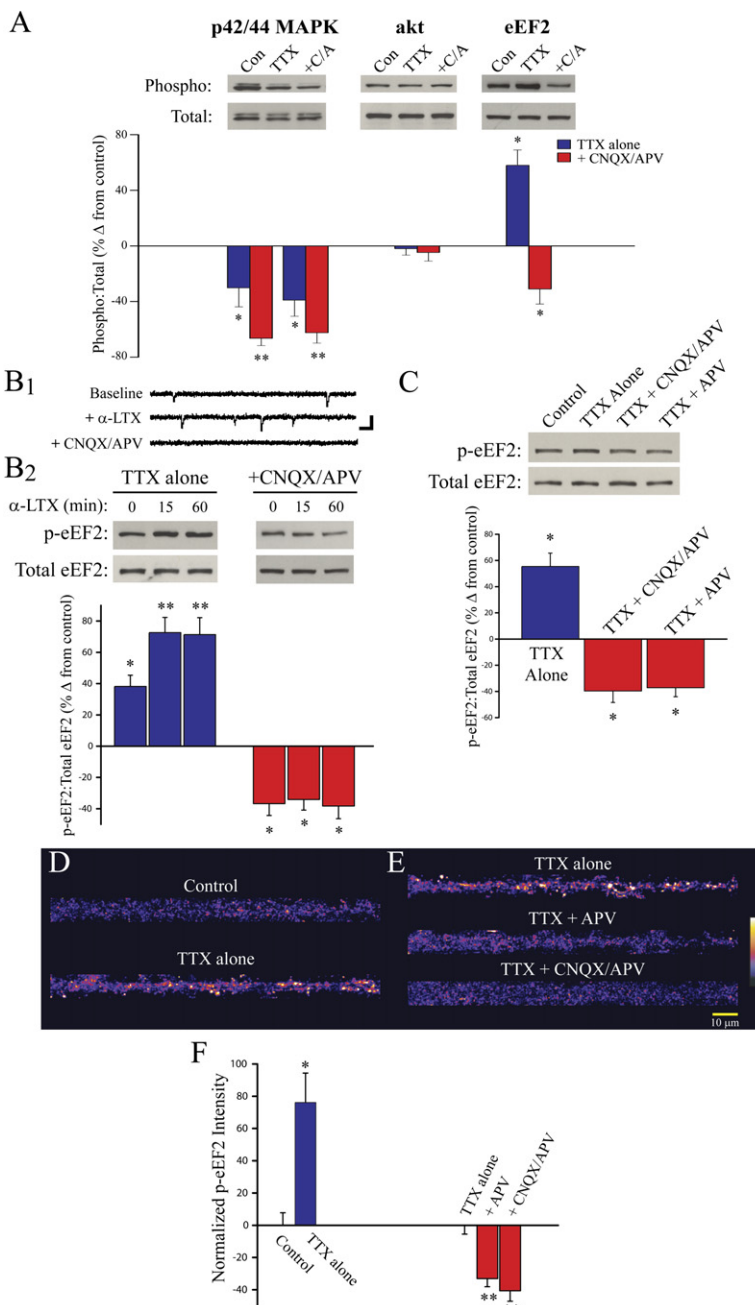
(D and E) Summary data. Mean ( $\pm$ SEM) change in reporter expression with local mini blockade (D) or vehicle (E) in different segments of treated dendrites over time, relative to baseline (20 min prior to local perfusion), normalized to the average change in untreated dendritic segments. Whereas the rate of change in vehicle-treated segments closely matched that in untreated regions of the same dendrite at all time points, a progressive increase in reporter expression, relative to other areas of the same dendrite, was evident in segments treated locally with CNQX+APV. (F) Mean ( $\pm$ SEM) change in reporter expression (relative to baseline) in untreated and treated segments of dendrites over time in the three conditions examined. Under anisomycin treatment, a progressive loss in reporter expression was observed over time due to the lack of protein synthesis; the rate of reporter loss in treated versus untreated dendritic segments was indistinguishable, indicating that local mini blockade does not alter local reporter degradation or accumulation.

relative to untreated controls, but additional treatment with  $\alpha$ -LTX produced a significantly greater phosphorylation of eEF2 that was sustained for at least 60 min. In contrast, block of miniature synaptic transmission with GluR antagonists again produced significantly diminished levels of p-eEF2 relative to control. Importantly, the effect of  $\alpha$ -LTX was lost when minis were blocked postsynaptically, indicating that its positive effects on eEF2 phosphorylation require the integrity of miniature neurotransmission. Taken together, these results indicate that the phosphorylation of eEF2 is bidirectionally regulated by miniature synaptic transmission.

The phosphorylation of eEF2 at Thr56 is catalyzed by eEF2 kinase, a  $\text{Ca}^{2+}$ /calmodulin-dependent protein kinase (Nairn and Palfrey, 1987). Since NMDARs, rather than AMPARs, are the principal source of activity-dependent  $\text{Ca}^{2+}$  influx at synapses, we next examined the role of these different receptor types in mediating eEF2 phosphorylation during miniature transmission (Figure 3C).

We found that blocking only the NMDAR component of miniature neurotransmission (TTX+APV) was sufficient to inhibit eEF2 phosphorylation during AP blockade, and the additional blockade of AMPARs (TTX+CNQX+APV) did not significantly alter the magnitude of this effect. These results suggest that the regulation of eEF2 phosphorylation by minis is primarily downstream of NMDAR activation.

To further validate the role of NMDAR minis in regulating eEF2 phosphorylation, we examined whether blocking voltage-gated  $\text{Ca}^{2+}$  channels that support AP-triggered neurotransmitter release would also enhance eEF2 phosphorylation at Thr56. Similar to the effects of direct AP blockade (with TTX), neurons treated with antagonists to the  $\text{Ca}^{2+}$  channels associated with evoked transmission at hippocampal synapses (N-type channel blocker  $\omega$ -conotoxin GVIA, 1  $\mu$ M, and the P/Q-type blocker  $\omega$ -agatoxin IVA, 200 nM; Wheeler et al., 1994) exhibited increased levels of p-eEF2 relative to untreated controls. As before,



(D–F) To assess whether AP blockade enhances eEF2 phosphorylation in dendrites, neurons were either untreated (control, n = 33) or treated with TTX (2 μM) for 2.5 hr (n = 31) prior to fixation and labeling with an antibody specific for p-eEF2. To examine if miniature transmission promotes eEF2 phosphorylation in dendrites, neurons were treated with TTX (2 μM; 2.5 hr) either alone (n = 31) or coincident with APV (60 μM; n = 33) or CNQX (40 μM) + APV (n = 33) over the last 1.5 hr. (D and E) Representative straightened dendrites from untreated controls and each of the above treatment conditions; color look-up table indicates p-eEF2 immunofluorescence intensity. (F) Mean (±SEM) change in dendritic p-eEF2 intensity relative to average control (left) or average in TTX alone (right). TTX alone led to significantly elevated levels of p-eEF2 in dendrites; coincident mini blockade led to significantly diminished dendritic levels of p-eEF2.

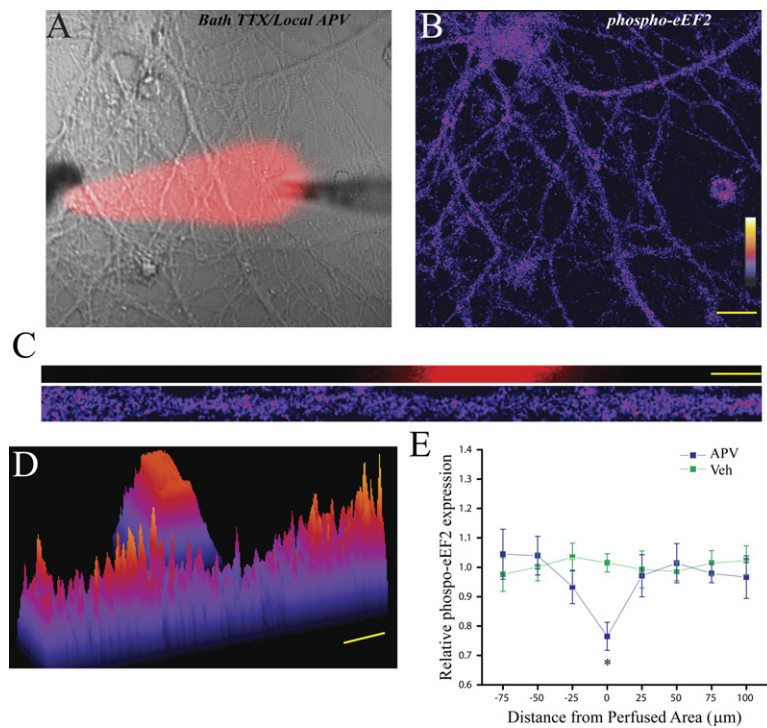
For all panels, \*p < 0.05 versus control; \*\*p < 0.05 versus TTX alone.

**Figure 3. Bidirectional Regulation of eEF2 Phosphorylation by Miniature Synaptic Transmission**

(A) To examine potential regulation of translation-relevant signaling pathways by miniature neurotransmission, neurons were either untreated (control) or treated with TTX (2 μM) for 12 hr with or without mini blockade (CNQX [40 μM] + APV [50 μM]) for the last 2 hr. Representative western blots (top) and summary data (below) using antibodies specific for dually phosphorylated (Thr202/Tyr204) and total p42/p44 MAPK, phosphorylated (Ser473) and total Akt, and phosphorylated (Thr56) and total eEF2 are shown. Whereas PI3 kinase signaling (using phosphorylated Akt as a downstream readout) was unaffected by either condition of activity blockade, p42/p44 MAP kinase signaling was strongly depressed by AP blockade alone, and even more so by the additional blockade of miniature neurotransmission (TTX+CNQX+APV). By contrast, eEF2 was regulated in opposite directions by AP versus mini blockade: TTX alone lead to significantly enhanced levels of p-eEF2 (the inactive form), whereas mini blockade lead to significantly diminished levels of p-eEF2 (i.e., a larger proportion of active eEF2). Data are from eight independent experiments.

(B) To examine if the regulation of eEF2 phosphorylation by minis is bidirectional, neurons were treated with TTX with or without mini blockade as in (A), and additionally challenged with α-latrotoxin (α-LTX; 100 pM) to stimulate miniature transmission. (B1) Representative whole-cell voltage-clamp recording demonstrating the frequency of mEPSCs in the same neuron in the presence of TTX alone (baseline), 10 min after addition of 100 pM α-LTX, and 5 min following addition of CNQX+APV. Scale bar, 100 ms, 10 pA. (B2) Stimulating miniature transmission with α-LTX significantly enhanced eEF2 phosphorylation; this effect required the integrity of miniature synaptic activity—mini blockade with CNQX+APV completely prevented the increase in p-eEF2 with α-LTX.

(C) Blockade of the NMDAR component of miniature neurotransmission alone (TTX+APV) produced comparable decreases in eEF2 phosphorylation to blocking both the AMPAR and NMDAR components, suggesting that the regulation of eEF2 by excitatory miniature transmission is primarily downstream of the NMDARs.



coincident blockade of NMDARs produced the opposite effect—significantly diminished levels of p-eEF2 (Figure S1 in the Supplemental Data available with this article online). Thus, the differential regulation of eEF2 phosphorylation by AP-dependent and miniature neurotransmission revealed in our earlier experiments is not strictly dependent on blocking APs per se, but rather on evoked neurotransmitter release.

#### Minis Regulate eEF2 Phosphorylation in Neuronal Dendrites

To further examine activity-dependent eEF2 phosphorylation, we stained neurons with an antibody specific for p-eEF2 (Marin et al., 1997) and examined the levels of p-eEF2 in the dendrites of neurons treated with AP blockade alone or a coincident blockade of miniature synaptic transmission (Figure 3D–3F). Similar to our biochemical experiments, neurons treated with TTX alone exhibited marked elevation of p-eEF2 in dendrites relative to untreated controls (Figure 3D). Coincident blockade of both AMPAR and NMDAR-dependent miniature neurotransmission (TTX+CNQX+APV) during TTX treatment strongly counteracted the increase in eEF2 phosphorylation observed with AP block alone. Again, this effect was primarily mediated by NMDARs, since selective blockade of NMDAR miniature neurotransmission (TTX+APV) largely accounted for the decrease in p-eEF2 levels in dendrites (Figures 3E and 3F). Together, these results demonstrate that ongoing miniature synaptic transmission, acting primarily through NMDAR activity, stimulates eEF2 phosphorylation in neuronal dendrites.

**Figure 4. Spatially Restricted NMDAR Mini Blockade Produces a Local Decrease in eEF2 Phosphorylation**

TTX (1 μM) was bath applied approximately 60 min prior to local perfusion of either TTX+APV (60 μM; n = 11 dendrites from six cells) or TTX+vehicle (n = 9 dendrites from five cells) for 60 min.

(A) DIC image showing neuron with local APV perfusion spot (red).

(B) p-eEF2 staining for the neuron shown in (A); intensity of p-eEF2 immunofluorescence given by color look-up table. Scale bar, 20 μm.

(C) Straightened dendrite from the cell shown in (A) and (B); the perfused area is also shown above the dendrite in red. Scale bar, 10 μm.

(D) 3D plot of relative p-eEF2 immunofluorescence for the dendrite shown in (C); perfusion spot is also indicated. Scale bar, 20 μm.

(E) Summary data. Mean ( $\pm$ SEM) relative p-eEF2 fluorescence intensity, normalized to the average nonzero pixel intensity outside the treated area. On the abscissa, positive and negative values indicate segments distal and proximal (toward), respectively, from the treated area. Local NMDAR mini blockade led to a significant (\* $p < 0.05$ ) decrease in p-eEF2 expression in the treated region, whereas local perfusion of vehicle had no effect.

#### Minis Regulate eEF2 Phosphorylation Locally in Dendrites

We next asked whether minis can regulate eEF2 phosphorylation locally in dendrites. To address this, we blocked APs in the entire dish (by bath application of TTX) and then locally blocked NMDARs using restricted perfusion of APV. Post hoc immunostaining for p-eEF2 revealed that local blockade of NMDAR minis (for 60 min) resulted in a decrease in p-eEF2 in the treated area relative to adjacent dendritic segments (Figures 4A–4E), whereas local perfusion of vehicle alone had no effect on p-eEF2 expression (Figure 4E). Conversely, local enhancement of miniature synaptic transmission by spatially restricted delivery of α-LTX during global AP blockade produced the opposite effect—a specific increase in p-eEF2 levels in perfused dendritic segments relative to other dendritic segments (Figures 5A–5E). These effects on local p-eEF2 levels were not due to redistribution of eEF2 in dendrites, since the relative levels of total eEF2, independent of the phosphorylation state, were not altered by restricted perfusion of either APV or α-LTX (Figure 5F). Together, these results indicate that the phosphorylation of eEF2 at Thr56 is bidirectionally and locally regulated in neuronal dendrites by levels of miniature neurotransmission.

#### The Regulation of eEF2 Phosphorylation by Minis Locally Controls Translation in Dendrites

The above results indicate that ongoing miniature synaptic transmission potently regulates eEF2 phosphorylation, primarily via the activity of NMDARs. Given that this

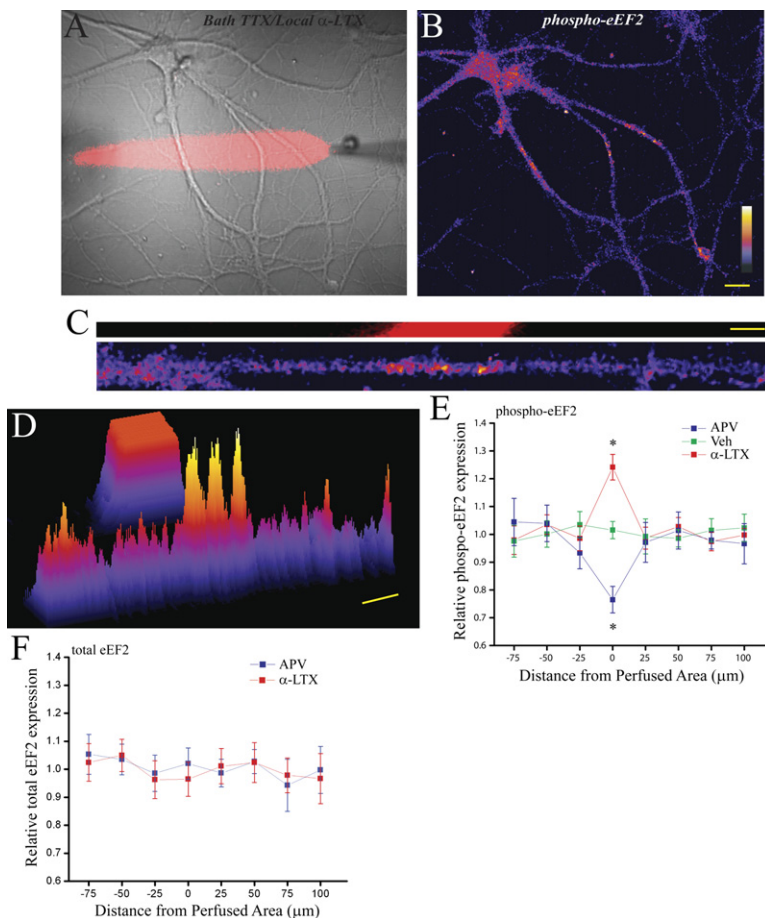


**Figure 5. Local Enhancement of Miniature Transmission Stimulates eEF2 Phosphorylation**

TTX (1  $\mu$ M) + LaCl<sub>3</sub> (0.1 mM) was bath applied approximately 60 min prior to local perfusion of the same solution plus 500 pM  $\alpha$ -LTX for an additional 45–60 min ( $n = 11$  dendrites from five cells).

(A) DIC image showing neuron with local  $\alpha$ -LTX perfusion spot (red).

(B) p-eEF2 staining for the neuron shown in (A); intensity of p-eEF2 immunofluorescence given by color look-up table. Scale bar, 20  $\mu$ m.

(C) Straightened dendrite from the cell shown in (A) and (B); the perfused area is also shown above the dendrite in red. Scale bar, 10  $\mu$ m.

(D) 3D plot of relative p-eEF2 immunofluorescence for the dendrite shown in (C). Scale bar, 20  $\mu$ m.

(E) Summary data. Mean ( $\pm$ SEM) relative p-eEF2 fluorescence intensity, normalized to the average nonzero pixel intensity outside the treated area. On the abscissa, positive and negative values indicate segments distal and proximal (toward soma), respectively, from the treated area. Data for local APV and local vehicle groups are replotted from Figure 3 for comparison. Local enhancement of miniature neurotransmission led to a significant (\* $p < 0.05$ ) increase in p-eEF2 expression in the treated region, indicating that the local regulation of eEF2 phosphorylation by minis is bidirectional.

(F) Summary data for experiments examining dendritic expression of total eEF2 (independent of phosphorylation state) after local perfusion with APV ( $n = 8$  dendrites from four cells) or  $\alpha$ -LTX ( $n = 9$  dendrites from four cells). Data are expressed as in (E). Neither local APV nor local  $\alpha$ -LTX altered overall expression of eEF2 in the treated area.

phosphorylation inhibits eEF2 function, we hypothesized that activation of eEF2 kinase by NMDAR minis contributes to the translational suppression that miniature events normally provide. If so, then inhibiting the kinase should be sufficient to stimulate translation. To address this question, we took advantage of two distinct eEF2 kinase inhibitors, rottlerin (Gschwendt et al., 1994) and NH125 (Arora et al., 2003), and examined their effect on protein synthesis (using the reporter described above) in dendrites when APs were blocked. After acquiring a baseline image in the presence of TTX alone, neurons were acutely challenged with either rottlerin (5  $\mu$ M), NH125 (10  $\mu$ M), or vehicle (TTX alone) and imaged 60 and 120 min later. While neurons maintained in TTX alone exhibited stable levels of reporter expression in distal dendrites, those acutely challenged with rottlerin or NH125 each exhibited marked increases in dendritic reporter expression over time (Figures 6A and 6B). To examine if these changes in reporter expression were due to enhanced protein synthesis, we repeated the same experiment in the presence of the protein synthesis inhibitor anisomycin (40  $\mu$ M). Reporter expres-

sion in neurons treated with anisomycin diminished substantially over time, and importantly, the rate of reporter loss was nearly identical under the three conditions examined (Figures 6C and 6D). These results indicate that the increase in reporter expression observed after blocking eEF2 kinase is due to enhanced protein synthesis rather than other posttranslational factors (e.g., degradation).

Finally, since rottlerin is also known to inhibit PKC $\delta$ , we examined the effects of a PKC inhibitor, Bisindolylmaleimide I (Bis; 1  $\mu$ M), at a concentration that effectively blocks this isoform. Unlike the effects of rottlerin or NH125, coincident administration of Bis during TTX did not alter dendritic reporter expression relative to TTX alone (mean  $\pm$  SEM baseline at 120 min: TTX alone, 91.2%  $\pm$  14.6%; TTX + Bis, 88.6%  $\pm$  17.3%;  $n = 12$  cells/group, nonsignificant). Thus, the enhanced rates of reporter synthesis observed with rottlerin and NH125 cannot be attributed to their effects on PKC.

Given that under conditions of intact miniature transmission, direct inhibition of eEF2 kinase stimulates dendritic protein synthesis, we next asked whether the local

## Neuron

## eEF2 and Dendritic Protein Synthesis

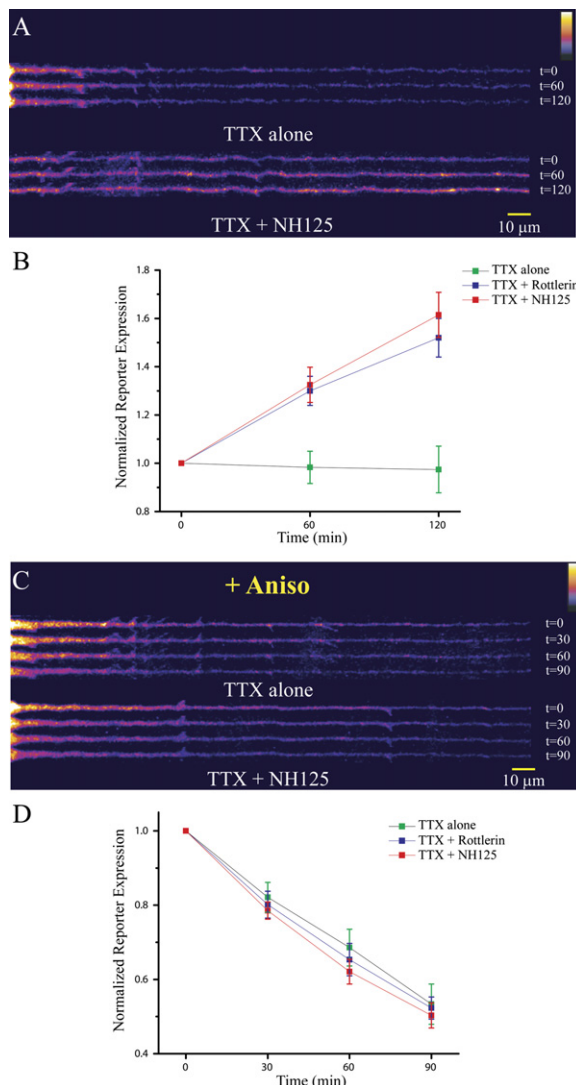


**Figure 6. Inhibition of eEF2 Kinase during Miniature Transmission Drives Dendritic Protein Synthesis**

Neurons ( $n = 16$  cells/group) expressing the protein synthesis reporter were treated with TTX (2 μM) prior to imaging, and challenged with one of two distinct eEF2 kinase inhibitors—rottlerin (5 μM) or NH125 (10 μM)—immediately following acquisition of a baseline image ( $t = 0$ ). A second set of experiments examined the same treatment conditions ( $n = 14$  cells/group) in the presence of the protein synthesis inhibitor anisomycin (40 μM).

(A) A time-lapse montage of straightened dendrites from cells either maintained in TTX alone or acutely challenged with NH125.

(B) Mean ( $\pm$ SEM) reporter expression (relative to baseline) in the distal dendritic compartment (>125 μm from soma) for each of the three treatment conditions. Treatment with rottlerin or NH125 enhanced dendritic reporter expression, whereas expression remained stable in the presence of TTX alone.

(C) A time-lapse montage of straightened dendrites from cells treated as in (A), but in the presence of anisomycin.

(D) Mean ( $\pm$ SEM) reporter expression (relative to baseline) in distal dendrites in each of the three treatment conditions in the presence of anisomycin. Substantial decreases in reporter expression over time were evident with anisomycin treatment, but the rate of reporter

regulation of eEF2 phosphorylation by miniature neurotransmission is sufficient to provide spatially specific control of dendritic translation. After a baseline image series was acquired in the presence of bath-applied TTX, dendritic segments were locally perfused with TTX+NH125 to block eEF2 kinase in a spatially defined area. For locally treated dendrites, we compared changes in reporter expression in the treated dendritic segment with those of other dendritic segments outside the perfused area both prior to and 0–80 min following local perfusion of NH125. For dendrites that did not pass through the perfusion area (untreated), we compared changes in reporter expression in an area of identical size and distance from the cell soma as the treated dendrites from the same neurons. We found that the change in reporter expression in the treated area was initially comparable to that of other segments of the same dendrite ( $t = -20$  to 0 min), but following local NH125 perfusion, treated areas demonstrated a progressive increase in reporter expression over the next 80 min (Figures 7A–7C). By contrast, no such differential effect was observed in untreated dendrites (Figure 7D) from the same neurons, and local perfusion of TTX alone also did not alter reporter synthesis locally (Figure 2E), indicating that the marked increase in local reporter expression was specifically due to NH125 treatment. These results thus indicate that eEF2 kinase activity not only exerts control over dendritic protein synthesis, but that it does so in a spatially limited manner.

## DISCUSSION

We have demonstrated that eEF2 acts as a local biochemical sensor for miniature synaptic transmission, serving to couple this form of neurotransmission to local translational suppression in dendrites. Other studies have demonstrated a strong relationship between phosphorylation of eEF2 and translational suppression in cultured neurons (Marin et al., 1997), synaptic biochemical fractions (Scheetz et al., 2000), or hippocampal slices (Chotiner et al., 2003) in response to intense activation of ionotropic GluRs. Here, we find that eEF2 phosphorylation driven by miniature neurotransmission acts to constrain neuronal protein synthesis, working locally within intact neuronal dendrites to suppress translation in a spatially specific fashion. Interestingly, we have also found that intrinsic AP-dependent network activity in cultured hippocampal neurons maintains eEF2 in a relatively dephosphorylated (active) state, suggesting that basal levels of AP-dependent and miniature neurotransmission regulate eEF2 in opposite directions, similar to their opposing influences on dendritic protein synthesis (Sutton et al., 2004). Thus, while eEF2 phosphorylation is clearly engaged by intense increases in AP-triggered neurotransmission, its responsiveness to AP-dependent and miniature synaptic

turnover in the absence of protein synthesis was similar among treatment groups. Fluorescence intensity is indicated by the color look-up table in (C).

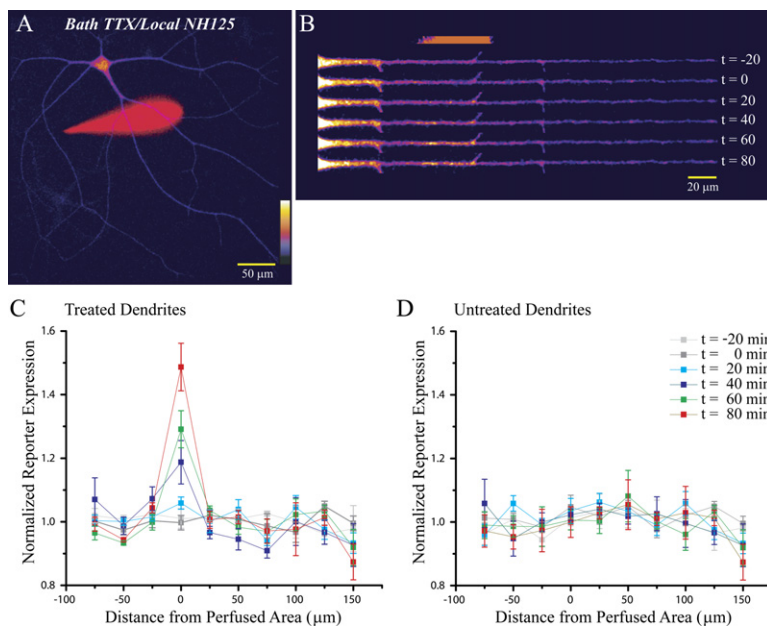


**Figure 7. Spatially Restricted Blockade of eEF2 Kinase Stimulates Local Dendritic Protein Synthesis**

Neurons expressing the translation reporter and treated with TTX (2 μM) were imaged before and after local perfusion with NH125 (10 μM; starting at t = 0).

(A) Shown is a neuron with superimposed perfusion area demarcated by Alexa 568 fluorescence in red.

(B) A time-lapse montage of a straightened dendrite from the cell shown in (A) from 20 min before to 80 min following local perfusion, at 20 min intervals; the perfusion area (in red) is also shown above the dendrites. Fluorescence intensity is indicated by the color look-up table in (A).

(C and D) Mean ( $\pm$ SEM) change in reporter expression in different segments of treated (C) or untreated (D) dendrites ( $n = 12$  and 10 dendrites, respectively, from six cells) over time relative to baseline (40 min prior to local perfusion) normalized to the average change in the same dendrites outside the perfusion area. Dendrites from the same cells as in (C), but not passing through the perfusion area, were used for the analysis in (D); an area identical in size and distance from the soma (relative to the corresponding treated dendrite from the same neuron) was used for the “perfusion area” in (D).

tical in size and distance from the soma (relative to the corresponding treated dendrite from the same neuron). Spatially restricted blockade of eEF2 kinase induced local reporter synthesis in treated dendrites, whereas reporter expression in untreated dendrites remained consistent with the dendrite as a whole.

transmission is qualitatively distinct during periods of normal AP-triggered network activity.

#### eEF2 Is a Biochemical Sensor Tuned to Local Miniature Synaptic Transmission

In recent years, it has become clear that different activity-driven signaling pathways at synapses are capable of encoding particular features of the activity patterns that activate them. For example, CAMKII, a protein kinase strongly implicated in the induction of long-term potentiation (e.g., Malinow et al., 1989; Silva et al., 1992; Barria et al., 1997), is capable of decoding the frequency of  $\text{Ca}^{2+}$  oscillations in vitro (De Koninck and Schulman, 1998). Likewise, persistent activation of p42/p44 MAPK by membrane depolarization in cultured hippocampal neurons is critically dependent on spacing of individual stimuli (Wu et al., 2001). Our results indicate that p42/p44 MAPK is generally tuned to the absolute levels of synaptic activity, without specific responsiveness to the quality of neurotransmission (i.e., whether the activity derives from evoked or spontaneous release). By contrast, the activity-dependent phosphorylation status of eEF2 is critically dependent on relative levels of AP-dependent and miniature synaptic transmission. When AP-dependent transmission dominates, a sizeable amount of eEF2 is dephosphorylated. However, during AP blockade, when miniature neurotransmission dominates, a marked increase in eEF2 phosphorylation results. We have further shown that this eEF2 phosphorylation is specifically driven by miniature neurotransmission, since increasing (with

$\alpha$ -LTX) or removing (with GluR antagonists) the impact of minis produces corresponding increases or decreases in eEF2 phosphorylation. Finally, using restricted perfusion techniques, we have shown that this bidirectional regulation of eEF2 phosphorylation by miniature neurotransmission is implemented in a spatially specific fashion. These results suggest that eEF2 phosphorylation is tuned to local levels of miniature synaptic transmission.

#### Unique Modes of Translational Inhibition Conferred by AMPAR and NMDAR Minis

Phosphorylation of eEF2 at Thr56 is catalyzed by a  $\text{Ca}^{2+}$ /calmodulin-dependent protein kinase (Nairn and Palfrey, 1987). Thus, the fact that minis regulate eEF2 phosphorylation primarily through NMDARs suggests a model in which the  $\text{Ca}^{2+}$  influx through the NMDAR engages this phosphorylation step directly, through activation of eEF2 kinase. In support of this notion, the open-channel NMDAR antagonist MK-801, when applied during AP blockade, also drives dendritic protein synthesis (data not shown), suggesting that ion flux through the NMDARs rather than glutamate binding is responsible for the translational suppression. Moreover, the characteristics of eEF2 kinase match well with the small currents generated by miniature release; for example, relative to CAMKII, eEF2 kinase is activated by >5-fold lower  $\text{Ca}^{2+}$  concentrations (Hughes et al., 1993) and exhibits approximately two orders of magnitude greater affinity for calmodulin (Mitsui et al., 1993). Thus, whereas CAMKII has been shown to effectively decode aspects of AP-triggered

neurotransmission such as input frequency (e.g., De Koninck and Schulman, 1998), eEF2 kinase seems optimized for decoding asynchronous activity on a dramatically different scale of sensitivity.

Previous studies have indicated that AMPAR and NMDAR minis cooperate in inhibiting dendritic protein synthesis (Sutton et al., 2004). Our results suggest that a major component of the NMDAR-mediated inhibition of local translation involves the phosphorylation (and inactivation) of eEF2. However, whereas blockade of both AMPAR and NMDAR minis enhances protein synthesis to a greater degree than NMDAR mini blockade alone, blockade of NMDAR minis fully accounts for the dephosphorylation of eEF2. These observations suggest that miniature transmission recruits an additional, as of yet unidentified mechanism for local translational suppression through AMPARs. Other studies also support a unique role for the AMPAR component of miniature synaptic transmission in mediating certain aspects of synaptic function. For example, McKinney et al. (1999) demonstrated that miniature synaptic events can maintain spine density in organotypic hippocampal slices during prolonged periods (7 days) of activity deprivation and that the AMPAR component of these events was critically important for this structural stability. Together, these observations suggest unique functional roles for the AMPAR and NMDAR components of excitatory miniature neurotransmission.

#### Functional Implications of Translational Control at the Level of Elongation

Although diminished rates of protein synthesis are the immediate functional consequences of lowering elongation efficiency, it has been suggested that this means of translational control serves at least two other functions. First, previous studies have demonstrated that, in some circumstances, reducing elongation efficiency can reduce translation error rates (e.g., Thompson and Karim, 1982; Abraham and Pihl, 1983). Given the metabolic cost inherent in long-range mRNA transport into dendrites at distances of hundreds of microns, translational fidelity is presumably of greater importance for local translational control in dendrites than in the soma, where translational capacity is less limiting. Thus, minis may also act to limit missense errors or premature termination of translation at individual synapses, where, based on polyribosome numbers from electron micrographs, it is likely that only a handful of mRNAs can be translated at any one time (e.g., Steward and Reeves, 1988; Ostroff et al., 2002). Second, it has been suggested that reducing elongation efficiency may favor the translation of particular mRNAs and thus serve to alter the complement of mRNAs in the actively translating pool (Walden and Thach, 1986; Scheetz et al., 2000). For example, in synaptoneuroosomes prepared from superior colliculus neurons, intense NMDAR stimulation stimulates eEF2 phosphorylation, reduces global protein synthesis by 50%, and yet enhances synthesis of  $\alpha$ CAMKII (Scheetz et al., 2000). Importantly, low concentrations of

the elongation inhibitor cycloheximide also enhanced  $\alpha$ CAMKII synthesis while depressing global translation in synaptoneuroosomes, suggesting that the reduction in elongation efficiency itself can be sufficient to drive synthesis of  $\alpha$ CAMKII (and possibly other proteins), given the appropriate context. Based on these findings, Scheetz et al. (2000) proposed that NMDAR-dependent phosphorylation of eEF2 could shift the rate-limiting step in local translation from initiation to elongation, which could select particular mRNAs for translation that are normally translated poorly. Thus, it is possible that ongoing miniature transmission alters the propensity for particular mRNAs to be locally translated, either by a mechanism similar to that proposed above or by maintaining the association of specific mRNAs with polyribosomes. It is noteworthy, however, that in our studies we find that local synthesis of a fluorescent translation reporter (which is flanked by the 5' and 3' untranslated regions of  $\alpha$ CAMKII) in hippocampal neurons was suppressed by eEF2 phosphorylation driven by NMDAR minis, suggesting that the context provided by miniature synaptic transmission is not permissive for the unique mode of regulation identified by Scheetz et al. (2000). Other studies have demonstrated, for example, that strong NMDAR stimulation produces several biochemical changes that promote translation initiation (e.g., Banko et al., 2004; Kelleher et al., 2004; Gong et al., 2006), raising the question as to how these changes interact with regulation at the level of elongation. Alternatively, the inverse relationship between elongation efficiency and  $\alpha$ CAMKII synthesis observed by Scheetz et al. (2000) might depend on a limited mRNA pool, a potential issue that we intentionally circumvent through overexpression of our reporter mRNA. In fact, mini blockade is known to broadly activate synthesis of a number of endogenous proteins (Sutton et al., 2004), suggesting that the conditions of reporter expression we use capture general changes in translational efficiency more strongly than specific regulatory mechanisms unique to  $\alpha$ CAMKII. Nevertheless, consistent with the proposal of Scheetz et al. (2000), our results do show that the local phosphorylation of eEF2 in dendrites constrains local protein synthesis, indicating that elongation efficiency can be a limiting condition for local translational control.

#### Multiple Parallel Mechanisms for Coupling Activity Patterns to the Translation Machinery

A major challenge in studies of local translational control is to understand how specific regulatory mechanisms operate within the highly dynamic nature of activity within neuronal circuits. CA1 hippocampal neurons, for example, are continuously bombarded by activity from any one of the ~30,000 different inputs they receive, yet any one of these inputs may experience extended periods without AP-triggered synaptic activity. Considerable attention has been devoted to the former case, and while important progress has been made in understanding the mechanisms by which evoked activity patterns engage the

protein synthesis machinery to alter synaptic function (for reviews, see Klann and Dever, 2004; Sutton and Schuman, 2005, 2006; Pfeiffer and Huber, 2006), how these unique patterns of activity are decoded by the local translation machinery is still poorly understood. In the latter case, where evoked activity at particular inputs is low, miniature synaptic events appear to serve a local stabilizing role at synapses, preventing runaway scaling of synaptic strength during these periods of inactivity (Sutton et al., 2006). Here, we have identified eEF2 as one of the biochemical sensors that is tuned to miniature synaptic transmission, and show that it contributes to the local translational suppression conferred by miniature events. Moreover, we have shown that intrinsic AP-mediated network activity opposes the impact of miniature transmission on eEF2 phosphorylation. These results indicate that distinct modes of neurotransmission (AP-dependent versus spontaneous release) are decoded by the translational apparatus in dendrites, which implies the existence of other decoding mechanisms that act in parallel to link specific features of evoked synaptic activity (e.g., pattern, frequency) with local translational control.

## EXPERIMENTAL PROCEDURES

### Cell Culture and Infection

Dissociated postnatal (P1–2) rat hippocampal neuron cultures, plated at a density of 230–460 mm<sup>2</sup> in poly-D-lysine-coated glass-bottom petri dishes (Mattek), were prepared as previously described (Aakalu et al., 2001) and maintained for at least 21 DIV at 37°C in growth medium [Neurobasal A supplemented with B27 and Glutamax-1 (Invitrogen)] prior to use. To analyze dendritic protein synthesis, neurons were infected with a Sindbis viral vector encoding a fluorescent translation reporter (coding sequence for a myristoylated, destabilized GFP flanked by the 5' and 3' untranslated regions of  $\alpha$ -CAMKII; Aakalu et al., 2001). For infection, cells were washed once with growth medium, then incubated with virus (diluted in growth medium) for 10–20 min at 37°C. Following infection, cells were washed again with growth medium, then incubated with conditioned media containing 2  $\mu$ M TTX for 7–8 hr prior to imaging.

### Electrophysiology

Whole-cell patch-clamp recordings were made from cultured hippocampal neurons bathed in HBS (containing 119 mM NaCl, 5 mM KCl, 2 mM CaCl<sub>2</sub>, 2 mM MgCl<sub>2</sub>, 30 mM glucose, and 10 mM HEPES [pH 7.4]), plus 1  $\mu$ M TTX and 10  $\mu$ M bicuculline, with an Axopatch 200B amplifier. Whole-cell pipette internal solutions contained 100 mM cesium gluconate, 0.2 mM EGTA, 5 mM MgCl<sub>2</sub>, 2 mM adenosine triphosphate, 0.3 mM guanosine triphosphate, and 40 mM HEPES (pH 7.2), and had resistances ranging from 4–6 M $\Omega$ . Cultured neurons with a pyramidal-like morphology were voltage-clamped at -70 mV and series resistance was left uncompensated. mEPSCs were analyzed off-line using Synaptosoft mini analysis software. Statistical differences between experimental conditions were determined by ANOVA and post hoc Fisher's LSD test.

### Microfluidic Experiments

Microfluidic chambers were previously developed to isolate microenvironments composed of dendritic and axonal regions (Taylor et al., 2003, 2005). These chambers consist of two parallel microfluidic channels, both connected by inlet and outlet wells. These two channels or compartments are separated by a solid barrier region with over 150 microgrooves embedded in the bottom of the connecting barrier.

The dimensions of the microgrooves (7.5  $\mu$ m wide, 3  $\mu$ m high) allow dendrites and axons to enter, but prevent the passage of larger cell bodies. Due to the high fluidic resistance of the microgrooves, a slight volume difference between the two channels (30–50  $\mu$ l) generates a pressure difference which facilitates the isolation of soluble treatments to one side. For smaller-molecular-weight molecules, which generally have larger diffusion coefficients (e.g., TTX and APV), there is some diffusion within the microgrooves after 3 hr (Figure 1B), which decreases substantially over the 900  $\mu$ m barrier. Using xy scans of isolated Alexa Fluor 488 (1  $\mu$ M, MW 570, 3 hr) through the microgrooves, we estimate that the concentration in the proximal 100  $\mu$ m of the microgroove is <45% of the concentration in the treated side, and <3% in the distal 100  $\mu$ m. Due to the small cross-sectional area of the microgrooves and the pressure gradient, we found the concentration in the adjacent compartment to be negligible.

We plated two populations of neurons on either side of the barrier, allowing processes and synaptic connections to form within the microgrooves. We applied TTX selectively to one side (the presynaptic compartment), then performed whole-cell patch-clamp recordings to examine whether APs could be selectively blocked in the treated side. Due to the pressure difference between the two compartments, there is a slight flow through the microgrooves, which generates a dilution effect in the treated side. To compensate for this, we used higher than normal concentrations of TTX (5  $\mu$ M). For current-clamp recordings, we used a volume difference of 50  $\mu$ l, applied TTX for 1 hr, then rinsed out the TTX and removed the poly(dimethylsiloxane) (PDMS) chamber. APs were selectively blocked for >45 min. In addition to showing that we can selectively block APs, this experiment also confirms the ability to selectively treat one compartment without influencing the other.

Neurons were infected with the reporter virus in one compartment (the postsynaptic side). Typically, 10–20 infected neurons had dendrites extending into the microgrooves, and in all cases the virus infected cells only on the virus-applied (postsynaptic) side. After 8–9.5 hr, the entire chamber was rinsed with HBS three times, then 300  $\mu$ l of HBS was applied to the reporter-infected side and 250  $\mu$ l of TTX (5  $\mu$ M) was applied to the presynaptic side. After 1–1.5 hr, images were taken every 10 min. Three or four baseline images were taken, then the fluid was removed from the chamber, 300  $\mu$ l of HBS was added to the presynaptic side, and 250  $\mu$ l of APV (250  $\mu$ M) was added to the postsynaptic side. Images were taken every 10 min. We estimate a concentration of APV within the microgrooves sufficient to block NMDARs (45% of 250  $\mu$ M is 112.5  $\mu$ M).

### Western Blotting

Neurons were treated in conditioned media with TTX (2  $\mu$ M) for 12 hr either alone or with CNQX (40  $\mu$ M) + APV (60  $\mu$ M) coincident with the last 2 hr of TTX treatment. Samples were collected in lysis buffer containing 100 mM NaCl, 10 mM NaPO<sub>4</sub>, 10 mM Na<sub>4</sub>P<sub>2</sub>O<sub>7</sub>, 10 mM lysine, 5 mM EDTA, 5 mM EGTA, 50 mM NaF, 1 mM NaVO<sub>3</sub>, 1% Triton-X, 0.1% SDS, and 1 tablet Complete Mini protease inhibitor cocktail (Roche)/7 ml (pH 7.4). The samples were centrifuged at top speed in a microfuge for 15 min to remove any insoluble material, then total protein concentrations were determined by a modified Lowry assay (DC protein assay, Biorad). Equal amounts of protein for each sample (20–30  $\mu$ g) were loaded and separated on 4%–15% Tris-HCl gradient gels, then transferred to polyvinylidene fluoride (PVDF) membranes. Blots were blocked with Tris-buffered saline containing 0.1% Triton-X (TBST), 5% BSA, 50 mM NaF, and 1 mM NaVO<sub>3</sub> for 60 min at room temperature (RT), and incubated with the following rabbit polyclonal primary antibodies (all from Cell Signaling Technology) for either 60 min at RT or overnight at 4°C: anti-phospho Akt (Ser473; 1:1000), anti-total Akt (1:1000), anti-phospho p42/p44 MAPK (Thr202/Tyr204; 1:2000), anti-total p42/p44 MAPK (1:2000), anti-phospho eEF2 (Thr56; 1:500), and anti-total eEF2 (1:500). After extensive washing with TBST, blots were incubated with HRP-conjugated anti-rabbit secondary antibody (1:5000; Jackson Immunoresearch) followed by

chemiluminescent detection (ECL, Amersham Biosciences). Band intensity was quantified with densitometry using NIH Image J, and the ratio of phosphorylated protein to total protein was calculated and expressed relative to the matched control sample. Statistical differences between treatment conditions and control were assessed by Chi square, whereas comparisons between TTX alone and TTX+CNQX+APV were assessed with either paired t tests (two groups) or ANOVA followed by Fisher's LSD.

#### Immunocytochemistry

Prior to labeling, neurons were untreated (controls) or treated with TTX (2  $\mu$ M; 2.5 hr) in conditioned media either alone or with CNQX (40  $\mu$ M) + APV (60  $\mu$ M) or APV (60  $\mu$ M) alone coincident with the last 1.5 hr of TTX treatment. Cells were then fixed on ice for 20 min with 4% paraformaldehyde/4% sucrose in PBS, permeabilized (0.1% Triton-X in PBS, 10 min), and labeled with rabbit polyclonal antibody against p-eEF2 (1:100, 60 min at RT; kindly provided by Dr. A.C. Nairn, Dept. Psychiatry, Yale University), followed by immunocytochemical detection with Alexa 488-conjugated anti-rabbit secondary antibody (1:250, 60 min at RT). Neurons were also labeled with either mouse monoclonal anti-MAP2 antibody (1:800; Sigma), followed by Alexa 546-conjugated anti-mouse secondary antibody, or with rhodamine-phalloidin (1:200, 60 min RT; Molecular Probes).

For analysis of immunocytochemistry experiments, images were obtained with Olympus IX-70 or Zeiss LSM 510 laser scanning confocal microscopes using a Plan-Apochromat 63 $\times$ /1.4 oil objective. Alexa 488 and 546 were visualized by excitation with the 488 line of an argon ion laser and the 543 nm line of a HeNe laser, respectively, with emission filters of LP 505 and BP 565-615. Neurons with a pyramidal-like morphology were selected for imaging by epifluorescent visualization of MAP2 or phalloidin staining, to ensure blind sampling of p-eEF2 expression. Identical acquisition parameters were used to acquire images from each treatment condition. For analysis, the principal dendrite of each neuron was linearized using the straighten plugin for Image J, and the average nonzero pixel intensity for the p-eEF2 channel was measured for each dendrite. Data for each variable in all groups were normalized to the average value in the respective control groups (untreated or TTX alone). Statistical differences were assessed by ANOVA, followed by Fisher's LSD post hoc tests.

#### Live-Cell Reporter Imaging

For experiments examining synthesis of the translation reporter using bath application of eEF2 kinase inhibitors, conditioned media was replaced with HBS containing 1  $\mu$ M TTX, and neurons were maintained at 37°C for 1.5–2 hr prior to imaging and throughout the experiment. All neurons chosen for experiments had a pyramidal-like morphology with one or two major dendrites emerging from the soma. After a baseline image was acquired, neurons were immediately challenged with rottlerin (5  $\mu$ M), NH125 (10  $\mu$ M), or 0.05% DMSO (the vehicle for both rottlerin and NH125), and imaged at 30 or 60 min intervals. Unfortunately, exposures of rottlerin and NH125 >2.5 hr were found to be cytotoxic, precluding analysis of long-term effects of eEF2 kinase inhibition. Anisomycin (40  $\mu$ M), when used, was applied coincident with the initial replacement of conditioned media with HBS.

All images were acquired in 0.4  $\mu$ m sections, and z-series were set to span the entire neuronal volume. Image analysis was conducted on maximal intensity z-compressed image stacks. The primary dendrite from each cell was linearized using NIH Image J, and fluorescence intensity was measured as a function of both time and distance from the cell soma. The dendritic compartment was divided into proximal and distal domains, defined by distances of less or greater than, respectively, 125  $\mu$ m from the soma. Comparable changes in both proximal and distal domains were observed in these experiments, so only the data from the distal dendritic compartment is presented.

Statistical differences in reporter expression (relative to baseline) between groups were assessed by ANOVA and Fisher's LSD post hoc tests.

#### Local Perfusion

All local perfusion experiments were performed with an Olympus IX-70 confocal laser scanning microscope using Plan-Apochromat 40 $\times$ /0.95 air or 40 $\times$ /1.0 oil objectives. The delivery micropipette was pulled as a typical whole-cell recording pipette with an aperture of ~0.5  $\mu$ m. The area of dendrite targeted for local perfusion was controlled by a suction pipette, which was used to draw the treatment solution across one or more dendrites and to remove the perfusate from the bath. Alexa 568 hydrazide (1  $\mu$ g/ml) was included in the perfusate to visualize the affected area. The 568 nm line of a krypton ion laser was used to visualize Alexa 568 fluorescence (emitted light collected above 600 nm) and to collect differential interference contrast (DIC) images. GFP and Alexa 488 (for p-eEF2 labeling) were excited with the 488 nm line of an argon ion laser, and emitted light was collected between 510 and 550 nm. In all local perfusion experiments, the bath was maintained at 37°C and continuously perfused at 1.5 ml/min with HBS containing 1  $\mu$ M TTX and other agents as indicated.

For analysis, the size of the treated area was determined in each linearized dendrite based on Alexa 568 fluorescence integrated across all images (typically 6–10) taken during local perfusion. Adjacent nonoverlapping dendritic segments, 25  $\mu$ m in length, proximal (i.e., toward the cell soma) and distal to the treated area were assigned negative and positive values, respectively.

For experiments examining local regulation of p-eEF2 expression, cells were immediately fixed following local perfusion, and processed for immunostaining as described above. Analysis of p-eEF2 expression in local perfusion experiments was performed on maximal intensity z-compressed image stacks. The average nonzero pixel intensity for the entire length of the dendrite, excluding the treated area, was used to normalize p-eEF2 intensity and was assigned a value of 1. The intensity of p-eEF2 immunofluorescence was then computed for the treated and all untreated dendritic segments and expressed relative to the average nontreated value. Statistical differences in normalized p-eEF2 staining between segments were assessed by ANOVA and Fisher's LSD post hoc tests.

For experiments examining local synthesis of the translation reporter during local perfusion, reporter expression was determined from maximal intensity z-compressed stacks. Prior to local perfusion, a baseline series of images was acquired to determine the pre-existing trajectory of reporter expression dynamics in both the treated area and untreated areas of dendrites. Reporter expression in all dendritic segments was expressed relative to a baseline image taken 20–40 min prior to local perfusion. The change at each time point for each dendritic segment, excluding the treated area, was averaged and assigned a value of 1 to normalize the change in reporter expression based on the trajectory of the dendrite as a whole. Statistical differences in normalized reporter expression between segments were assessed by ANOVA and Fisher's LSD post hoc tests.

#### Supplemental Data

The Supplemental Data for this article can be found online at <http://www.neuron.org/cgi/content/full/55/4/648/DC1/>.

#### ACKNOWLEDGMENTS

We thank H. Weld and L. Chen for making beautiful cultured hippocampal neurons, A. Nairn for kindly providing the p-eEF2 antibody used for our immunocytochemistry experiments and for helpful discussions, and G. Laurent for solving an experimental conundrum. This work was supported by the Damon Runyon Cancer Research Foundation (M.A.S.) and the NIH (E.M.S.). E.M.S. is an investigator of HHMI.

Received: November 3, 2006

Revised: June 19, 2007

Accepted: July 25, 2007

Published: August 15, 2007

## REFERENCES

- Aakalu, G., Smith, W.B., Jiang, C., Nguyen, N., and Schuman, E.M. (2001). Dynamic visualization of dendritic protein synthesis in hippocampal neurons. *Neuron* 30, 489–502.
- Abraham, A.K., and Pihl, A. (1983). Effect of protein synthesis inhibitors on the fidelity of translation in eukaryotic systems. *Biochim. Biophys. Acta* 741, 197–203.
- Arora, S., Yang, J.M., Kinzy, T.G., Utsumi, R., Okamoto, T., Kitayama, T., Ortiz, P.A., and Hait, W.N. (2003). Identification and characterization of an inhibitor of eukaryotic elongation factor 2 kinase against human cancer cell lines. *Cancer Res.* 63, 6894–6899.
- Ashton, A.C., Volynski, K.E., Lelianova, V.G., Orlova, E.V., Van Renterghem, C., Canepari, M., Seagar, M., and Ushkaryov, Y.A. (2001). alpha-Latrotoxin, acting via two Ca<sup>2+</sup>-dependent pathways, triggers exocytosis of two pools of synaptic vesicles. *J. Biol. Chem.* 276, 44695–44703.
- Banko, J.L., Hou, L., and Klann, E. (2004). NMDA receptor activation results in PKA- and ERK-dependent MnK1 activation and increased eIF4E phosphorylation in hippocampal area CA1. *J. Neurochem.* 91, 462–470.
- Barria, A., Muller, D., Derkach, V., Griffith, L.C., and Soderling, T.R. (1997). Regulatory phosphorylation of AMPA-type glutamate receptors by CAM-KII during long-term potentiation. *Science* 276, 2042–2045.
- Bradshaw, K.D., Emptage, N.J., and Bliss, T.V.P. (2003). A role for dendritic protein synthesis in hippocampal late LTP. *Eur. J. Neurosci.* 18, 3150–3152.
- Carroll, M., Warrem, O., Fan, X., and Sossin, W.S. (2004). 5-HT stimulates eEF2 dephosphorylation in a rapamycin-sensitive manner in Aplysia neurites. *J. Neurochem.* 90, 1464–1476.
- Ceccarelli, B., Hurlbut, W.P., and Mauro, A. (1973). Turnover of transmitter and synaptic vesicles at the frog neuromuscular junction. *J. Cell Biol.* 57, 499–524.
- Chotiner, J.K., Khorasani, H., Nairn, A.C., O'Dell, T.J., and Watson, J.B. (2003). Adenylyl cyclase-dependent form of chemical long-term potentiation triggers translational regulation at the elongation step. *Neuroscience* 116, 743–752.
- De Koninck, P., and Schulman, H. (1998). Sensitivity of CAM kinase II to the frequency of Ca<sup>2+</sup> oscillations. *Science* 279, 227–230.
- Fatt, P., and Katz, B. (1952). Spontaneous subthreshold activity at motor nerve endings. *J. Physiol.* 117, 109–128.
- Gong, R., Park, C.S., Abbassi, N.R., and Tang, S.J. (2006). Roles of glutamate receptors and the mammalian target of rapamycin (mTOR) signaling pathway in activity-dependent dendritic protein synthesis in hippocampal neurons. *J. Biol. Chem.* 281, 18802–18815.
- Gschwendt, M., Kittstein, W., and Marks, F. (1994). Elongation factor-2 kinase: effective inhibition by the novel protein kinase inhibitor rottlerin and relative insensitivity towards staurosporine. *FEBS Lett.* 338, 85–88.
- Holland, E.C. (2004). Regulation of translation and cancer. *Cell Cycle* 3, 452–455.
- Huber, K.M., Kayser, M.S., and Bear, M.F. (2000). Role for rapid dendritic protein synthesis in hippocampal mGluR-dependent long-term depression. *Science* 288, 1254–1256.
- Hughes, S.J., Smith, H., and Ashcroft, S.J.H. (1993). Characterization of Ca<sup>2+</sup>/calmodulin-dependent protein kinase in rat pancreatic islets. *Biochem. J.* 289, 795–800.
- Kang, H., and Schuman, E.M. (1996). A requirement for local protein synthesis in neurotrophin-induced synaptic plasticity. *Science* 273, 1402–1406.
- Kelleher, R.J., Govindarajan, A., Jung, H.Y., Kang, H., and Tonegawa, S. (2004). Translational control by MAPK signaling in long-term synaptic plasticity and memory. *Cell* 116, 467–479.
- Klann, E., and Dever, T.E. (2004). Biochemical mechanisms for translational regulation in synaptic plasticity. *Nat. Rev. Neurosci.* 5, 931–942.
- Malinow, R., Schulman, H., and Tsien, R.W. (1989). Inhibition of postsynaptic PKC or CAMKII blocks induction but not expression of LTP. *Science* 245, 862–866.
- Marin, P., Nastiuk, K.L., Daniel, N., Girault, J.A., Czernick, A.J., Glowinski, J., Nairn, A.C., and Premont, J. (1997). Glutamate-dependent phosphorylation of elongation factor-2 and inhibition of protein synthesis in neurons. *J. Neurosci.* 17, 3445–3454.
- McKinney, R.A., Capogna, M., Durr, R., Gahwiler, B.H., and Thompson, S.M. (1999). Miniature synaptic events maintain dendritic spines via AMPA receptor activation. *Nat. Neurosci.* 2, 44–49.
- Mitsui, K., Brady, M., Palfrey, H.C., and Nairn, A.C. (1993). Purification and characterization of calmodulin-dependent protein kinase III from rabbit reticulocytes and rat pancreas. *J. Biol. Chem.* 268, 13422–13433.
- Nairn, A.C., and Palfrey, H.C. (1987). Identification of the major Mr 100,000 substrate for calmodulin-dependent protein kinase III in mammalian cells as elongation factor-2. *J. Biol. Chem.* 262, 17299–17303.
- Ostroff, L.E., Fiala, J.C., and Harris, K.M. (2002). Polyribosomes redistribute from dendritic shafts into spines with enlarged synapses during LTP in developing rat hippocampal slices. *Neuron* 35, 535–545.
- Pfeiffer, B.E., and Huber, K.M. (2006). Current advances in local protein synthesis and synaptic plasticity. *J. Neurosci.* 26, 7147–7150.
- Redpath, N.T., Price, N.T., Severinov, K.V., and Proud, C.G. (1993). Regulation of elongation factor-2 by multisite phosphorylation. *Eur. J. Biochem.* 213, 689–699.
- Ruggero, D., and Sonenberg, N. (2005). The Akt of translational control. *Oncogene* 24, 7426–7434.
- Ryazanov, A.G., Shestakova, E.A., and Natapov, P.G. (1988). Phosphorylation of elongation factor 2 by EF-2 kinase affects rate of translation. *Nature* 334, 170–173.
- Scheetz, A.J., Nairn, A.C., and Constantine-Paton, M. (2000). NMDA receptor-mediated control of protein synthesis at developing synapses. *Nat. Neurosci.* 3, 211–216.
- Silva, A.J., Stevens, C.F., Tonegawa, S., and Wang, Y. (1992). Deficient hippocampal long-term potentiation in alpha-calcium-calmodulin kinase II mutant mice. *Science* 257, 201–206.
- Steward, O., and Reeves, T.M. (1988). Protein-synthesis machinery beneath postsynaptic sites on CNS neurons: association between polyribosomes and other organelles at the synaptic site. *J. Neurosci.* 8, 176–184.
- Sutton, M.A., and Schuman, E.M. (2005). Local translational control in dendrites and its role in long-term synaptic plasticity. *J. Neurobiol.* 64, 116–131.
- Sutton, M.A., and Schuman, E.M. (2006). Dendritic protein synthesis, synaptic plasticity, and memory. *Cell* 127, 49–58.
- Sutton, M.A., Wall, N.R., Aakalu, G.N., and Schuman, E.M. (2004). Regulation of dendritic protein synthesis by miniature synaptic events. *Science* 304, 1979–1983.
- Sutton, M.A., Ito, H.T., Cressy, P., Kempf, C., Woo, J.C., and Schuman, E.M. (2006). Miniature neurotransmission stabilizes synaptic function via tonic suppression of local dendritic protein synthesis. *Cell* 125, 785–799.
- Taylor, A.M., Rhee, S.W., Tu, C.H., Cribbs, D.H., Cotman, C.W., and Jeon, N.L. (2003). Microfluidic Multicompartment Device for Neuroscience Research. *Langmuir* 19, 1551–1556.

- Taylor, A.M., Burton-Jones, M., Rhee, S.W., Cribbs, D.H., Cotman, C.W., and Jeon, N.L. (2005). A microfluidic culture platform for CNS axonal injury, regeneration and transport. *Nat. Methods* 2, 599–605.
- Thompson, R.C., and Karim, A.M. (1982). The accuracy of protein biosynthesis is limited by its speed: high fidelity selection by ribosomes of aminoacyl-tRNA ternary complexes containing GTP. *Proc. Natl. Acad. Sci. USA* 79, 4922–4926.
- Walden, W.E., and Thach, R.E. (1986). Translational control of gene expression in a normal fibroblast. Characterization of a subclass

of mRNAs with unusual kinetic properties. *Biochemistry* 25, 2033–2041.

Wheeler, D.B., Randall, A., and Tsien, R.W. (1994). Roles of N-type and Q-type Ca<sup>2+</sup> channels in supporting hippocampal synaptic transmission. *Science* 264, 107–111.

Wu, G.Y., Deisseroth, K., and Tsien, R.W. (2001). Spaced stimuli stabilize MAPK pathway activation and its effects on dendritic morphology. *Nat. Neurosci.* 4, 151–158.